Luminescent Semiconductor Quantum Dots: Synthesis, Characterization and Biological Applications

Dissertation

Submitted to the

Fachbereich Chemie, Technische Universität Dortmund, Germany

for obtaining the degree of a

Doktor der Naturwissenschaften (Dr.rer.nat)

by

Hua-Chang Lu

Dortmund, April 2008

This work was carried out between September 2004 and March 2008 at the Biologisch-Chemische Mikrostrukturtechnik, Fachbereich Chemie, Technische Universität Dortmund, Germany, under the supervision of Prof. Dr. Christof M. Niemeyer. As a member of International Max Planck Research School for Chemical Biology (IMPRS-CB, Dortmund), this work was also financially supported by the IMPRS Scholarship from the Max Planck Society.

Referee 1:	Prof. Dr. Christof M. Niemeyer
Referee 2:	Prof. Dr. Christian Becker
Date of thesis defence and oral exam	May 21, 2008

Dedication

I dedicate this thesis to my grandfather, Chen Xiang-Yao, who passed away while I was writing this thesis.

我將此博士論文獻給我的外公陳祥堯。老人家于2008年春，也即我撰寫此論文期間，以89歲高齡辭世。遠隔萬里，不能回去見外公最後一面，抱憾泣奠，三叩首。

Publications

Parts of the results reported in this dissertation have already been published in the following publications:

Lu, H., Schöps, O., Woggon, U. and Niemeyer, C.M. *Self-assembled donor comprising quantum dots and fluorescent proteins for long-range fluorescence resonance energy transfer*. J. Am. Chem. Soc. **130**, 4815-4827 (2008).

Ipe, B.I., Shukla, A., Lu, H., Zou, B., Rehage, H. and Niemeyer, C.M. *Dynamic light-scattering analysis of the electrostatic interaction of hexahistidine-tagged cytochrome P450 enzyme with semiconductor quantum dots.* ChemPhyChem**, 7**, 1112-1118 (2006).

Abbreviations

0D	Zero-Dimensional
1D	One-Dimensional
2Ch-FRET	Two-Chromophore Fluorescence (or Förster) Resonance Energy Transfer
2D	Two-Dimensional
2D-PLE	Two-Dimensional-Photoluminescence Excitation Spectroscopy
3Ch-FRET	Three-Chromophore Fluorescence (or Förster) Resonance Energy Transfer
3D	Three-Dimensional
A	Adenine
Abs	Absorbance
AFM	Atomic Force Microscopy
a.u.	Arbitrary Unit
bp	Base Pair
BSA	Bovine Serum Albumin
C	Cytosine
°C	Degree Celsius
Cys	Cysteine
D/A	Donor/Acceptor
Da	Dalton
DDA	Dodecylamine
DNA	Deoxyribonucleic Acid
dsDNA	Double-Stranded DNA
dT	Deoxythymidine
DHLA	Dihydrolipoic Acid
DHLA-QDs	Dihydrolipoic Acid-coated Quantum Dots
DMF	N, N-Dimethylformamide
DTT	Dithiothreitol
ε	Extinction Coefficient
EDTA	Ethylene Diamine Tetraacetic Acid
Em	Emission

Equiv	Equivalent
EYFP	Enhanced Yellow Fluorescent Protein
FP	Fluorescent Protein
FPLC	Fast Protein Liquid Chromatography
FRET	Fluorescence (or Förster) Resonance Energy Transfer
FWHM	Full Width at Half Maximum
g	Gram
G	Guanine
GGpp	Geranylgeranyl pyrophosphate
GDP	Guanosine Diphosphate
GFP	Green Fluorescent Protein
GTP	Guanosine Triphosphate
HD	Hydrodynamic Diameter
HDA	Hexadecylamine
HEPES	4-(2-Hydroxyethyl)-Piperazine-1-Ethanesulfonic Acid
His_6	Hexahistidine
HPA	Hexylphosphonic Acid
hr	Hour
IgG	Immunoglobulin G
kb	Kilobase
Me_2Zn	Dimethylzinc
mL	Milliliter
mM	Millimolar
min	Minute
µL	Microliter
µm	Micrometer
µM	Micromolar
NCs	Nanocrytals
nm	Nanometer
nmol	Nanomole
No.	Number

NPs	Nanoparticles
ns	nanosecond
NTA	Nitrilo triacetic acid
OG	*β*-octylglucopyranoside
PAGE	Polyacrylamide Gel Electrophoresis
PEG	Poly (ethylene glycol)
PEG-PE	Poly (ethylene glycol) Phosphatidylethanolamine
PEG-PLs	Poly (ethylene glycol)-terminated Phospholipids
PEG2000-QDs	PEG2000-Phospholipid-coated QDs
PEG350-QDs	PEG350-Phospholipid-coated QDs
PL	Photoluminescence
PLs	Phospholipids
PLs-QDs	non-PEG Phospholipid-coated QDs
PLE	Photoluminescence Excitation Spectroscopy
pmol	Picomole
POPG	1-Palmitoyl-2-oleyl-sn-glycerophosphatidylglycerol
POPC	1-Palmitoyl-2-oleyl-sn-glycerophosphatidylcholine
ps	picosecond
QDs	Quantum Dots
QY	Quantum Yield
REP	Rab Escort Protein
RGGT	Rab Geranylgeranyl Transferase
rpm	Rotation per Minute
RT	Room Temperature
Se	Selenium
sec	Second
SEC	Size Exclusion Chromotography
SDS	Sodium Dodecyl Sulfate
ssDNA	Single-Stranded DNA
sSMCC	Sulfosuccinimidyl-4-(*N*-maleimmidomethyl)cyclohexane-1-carboxylate
T	Thymine

TBP	Tributylphosphine
TDPA	Tetradecylphosphonic Acid
TEM	Transmission Electron Microscopy
TEMED	N, N, N', N'-Tetramethylethylenediamine
$(TMS)_2S$	bis(Trimethylsilyl) Sulfide
TOP	Trioctylphosphine
TOPSe	Trioctylphosphine Selenium
TOPO	Trioctylphosphine Oxide
Tris	Tris (hydroxymethyl) amino methane
UV	Ultra-Violet
Vis	Visible
YFP	Yellow Fluorescent Protein

1 Introduction

1.1 General

We are witnessing an explosion of interest in the applications of nanoscale materials and structures for biological investigations in labeling, imaging, sensing, diagnostics in the past ten years.[1-9] Nanotechnology has become a key word in scientific research as well as in the public concern since the early 1990's. The unique electronical, magnetical, optical or physico-chemical properties of these nanomaterials distinguish them from bulk materials and make them applicable in a variety of fields and especially, in biological science and technology.

Nanobiotechnology is one of the highly interdisciplinary subfields and it attracted the interests of chemists, physicists, biologists, material scientists and engineers.[10, 11] There are several important and active areas of research including: 1) the development of methods for building nanostructures and nanostructured materials out of biological or biologically inspired components such as oligonucleotides, proteins, viruses, and cells; these structures are intended for both biological and abiological applications, 2) the utilization of synthetic nanomaterials to regulate and monitor important biological processes, and 3) the development of synthetic and soft mater compatible surface analytical tools for building nanostructures important in both biology and medicine. [10, 11] It is anticipated that advance in nanobiotechlogy will have great impact on chemistry, biology or medical area.

Nanocrystals (NCs) are often considered as a single 'crystal' of a size of a few nanometers consisting of around a few hundred to as many as 10,000 atoms, in which the electron motion is 'confined' by potential barriers in all dimensions.[3] Semiconductor nanocrystals, often termed as quantum dots (QDs), are regarded as an artificial atom, in which the energy levels are discrete, much as in an atom or molecule. But in the case of NCs, the distance of the electronic energy levels can be precisely chosen through variation of the size. QDs are normally highly fluorescent,[12] which makes them highly attractive as an alternative for traditional organic dyes and fluorescent proteins in many cases.[13-15] Nowadays, QDs are commercially available, for example, Qdots® from Invitrogen; Evidots® from Evident; NanoDots® from NanoCo.

In this thesis, the work on QDs was focused on CdSe NCs, which are the most intensively studied semiconductor NCs. They are produced by a range of well developed synthetic routes and solubilization strategies.[13, 16] Furthermore, after overcoating with an inorganic shell of ZnS, the NCs

become highly fluorescent and feature attractive optical properties as high quantum yield (QY), large absorption cross section and high photostability.[14]

1.2 Semiconductor quantum dots (QDs)

1.2.1 Quantum confinement effect and optical properties of QDs

Semiconductor quantum dots have attracted a huge interest of the scientific community over the past two decades mainly because of their applications as powerful fluorescent probes and building blocks of novel biosensors.[8, 13-15, 17, 18] Because of the small size of only a few nanometers, which is the same order of magnitude as the so-called Bohr exciton radius at room temperature,[12] the states of free charge carriers (electrons and holes) in semiconductor NCs are quantized. The movement of these electrons and holes is determined by quantum mechanics, so-called quantum confinement effect.[12, 19, 20] The nanocrystals are hence called quantum dots (QDs). Similar to the model of particle-in-a-box, the energy levels between the electrons and holes are discrete and particularly size-dependent. Quantum dots are also considered as artificial atoms because of the similarity between the discrete energy levels of QDs and those of atoms (Figure 1.1A).[12] Since the energy levels of QDs are size-dependent, they can be tuned in a controllable way by synthesizing different sizes of NCs of the same composition. The size-dependent energy levels of such semiconductor NCs contribute to the extraordinary optical and electrical properties.[13, 14] The smaller size of a semiconductor QD, the larger is the band gap and thus, the fluorescence of the shorter wavelength is achieved.

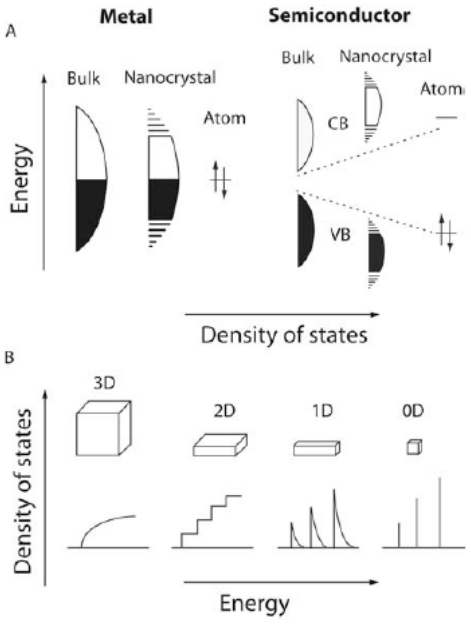

Figure 1.1 (A) Schematic representation of the density of states in metal and semiconductor NCs according to Alivisatos.[12, 19] In each cases, the dashed lines show the increasing band gap separations for bulk material to molecule, between the valence band (VB) and conduction band (CB). (B) Idealized density of states in one band of a semiconductor as a function of the dimensional freedom. 3D for the bulk, 2D for quantum films, 1D for quantum wires or fibers and 0D for quantum dots.

Figure 1.1A demonstrates the comparison of band gap of bulk metal and semiconductor QDs. In the case of QDs, the energy between valence band and conduction band is discrete due to the quantum effect and the HOMO-LUMO gap increases in semiconductor QDs of small size. Figure 1.1B shows the idealized density of states for one band of a semiconductor structure of 3, 2, 1, and zero dimensions. The energy levels are still continuous in the case of 3D materials, while the levels are discrete in the 0D QDs or similar case of a molecule.

Usually, the properties of normal bulk materials or crystalline solids are not influenced by their size. But when the sizes decrease down to the nanometer length, these crystalline solids start to experience changes in their properties which do not occur in bulk materials. There are two major effects which are responsible for these size variations. First, the surface atom ratio in a nanocrystal is much bigger than that in bulk materials. The surface atoms are important for their contribution to the free energy in any material and the surface atoms are also responsible for the big changes in thermodynamic properties such as the decrease of melting temperature depression. Secondly, the intrinsic properties of NCs are transformed by quantum size effects as described above. Semiconductor QDs are well known to exhibit strong variations in optical and electrical properties with size effects.[21] One such example of thermodynamic property that dramatically changes with the size of NCs is shown in Figure 1.2.[22] Melting point depressions of more than 50% are observed for small sized CdS QDs as compared to bulk materials. The increased ratio of the surface atoms with the decreasing of the particle size can be an explanation of this depression. In a nanocrystal containing only a few hundred atoms, the surface atoms take big ratio and these atoms tend to be coordinatively unsaturated and thus a large energy is associated with this surface. Usually, the surface energy is always lower in a liquid phase than in a solid phase. In a solid phase, rigid bonding structures cause stepped surfaces with higher energy corner and edge atoms. But the total surface energy tends to be reduced upon melting. This stabilizes the liquid phase over the solid phase. The smaller the QDs are, the bigger is the contribution made by the surface atoms to the overall energy of the system and thus the larger the melting temperature depression will be.[23]

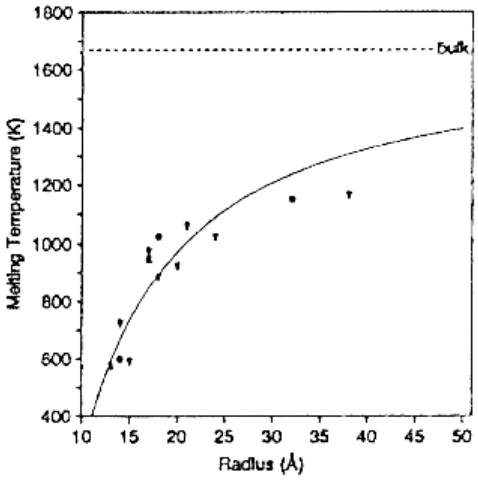

Figure 1.2 Melting temperature as a function of the size of CdS quantum dots from Goldstein, et al. [22]

The most attractive property of semiconductor QDs is the tunable optical, electrical or photoredox properties as a function of the particle size.[21] It was mentioned earlier that this is due to the quantum confinement effect, which arises as a consequence of the changes in the density of electronic states and was first studied in the 1980s[21, 24-27] and later developed by Brus et al. to explain the phenomena from the point of view of quantum chemistry.[28, 29] Based on this theory, in a semiconductor QD, the excitons follow the mechanism similar to a hydrogen atom and can be described by a hydrogen-like model. [28] Unlike in bulk materials where the electrons and holes are free to move, they are confined in QDs. This confinement leads to an increase of electronic energy, similar to the case of a particle-in-a box model. While the size quantization and confinement effect is mainly considered to describe various physical properties, the optical properties are the most of our concern. Figure 1.3 shows the size-dependent absorption and emission of QDs with different composition as CdS, CdSe, CdTe, InP, PbSe, etc.[14]

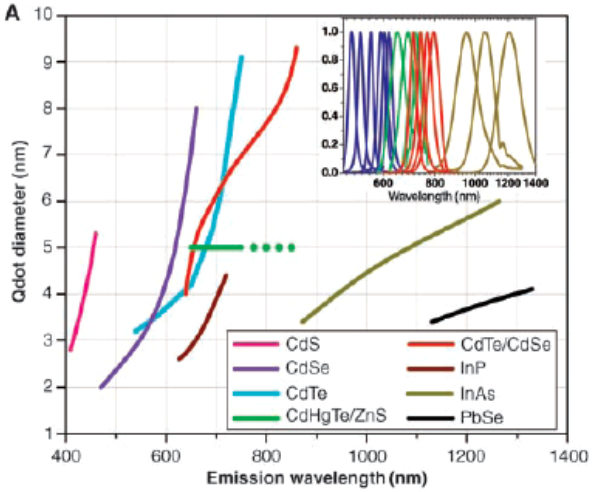

Figure 1.3 Emission maxima and sizes of quantum dots of different composition. Quantum dots can be synthesized from various types of semiconductor materials (normally, group II-VI: CdS, CdSe, CdTe…; group III-V: InP, InAs…; IV-VI: PbSe…) characterized by different bulk band gap energies. The curves represent experimental data on the dependence of peak emission wavelength on QD diameter. The range of emission wavelength is 400-1350 nm, with size varying from 2 to 9.5 nm. This image was taken from an excellent review article on QDs for biological applications.[14]

The optical properties of QDs are related to the electronic structure, chemical composition and also the nanocrystal size. The decrease of the crystal size causes the shift of absorption from infrared to the visible region of the electromagnetic spectrum since the band gap energy of the QD increases. Figure 1.4A shows how the emission of CdSe QD can be tuned by controlling the size and how the increase of the size shifts the emission from blue to the red end of the spectrum.[30-32] A typical absorption and emission spectrum of CdSe QD are shown in Figure 1.5. It is a 3.5 nm diameter CdSe sample prepared by Murray et al.[16] The sharp spectra features suggest high quality crystals and few electronic defect sites. The absorption spectra are influenced by various physical and chemical effects. For example, the polydispersity of QDs brings line broadening in the spectra. The spectra can also be influenced by the crystal structure of QD;[33] different surface coating also leads to modification of the absorption spectra.

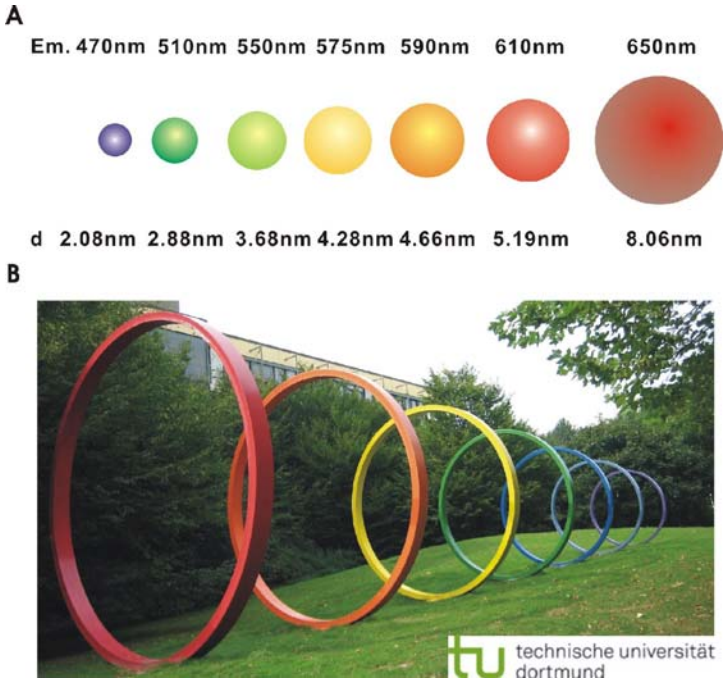

Figure 1.4 (A) Schematic representation of tunable optical properties of QDs. The emission of QDs can be tuned by controlling the size of CdSe: an increasing in the size (from ~2.1 nm to ~8.1 nm in diameter) of CdSe shifts

the emission from blue (~470 nm) to dark red (~650 nm) of the electromagnetic spectrum. The cartoon was drawn approximatively based on the data from ref. [30, 31] B) A set of statuary steels illustrating general size dependent properties in the north campus of Technical University of Dortmund, Germany.

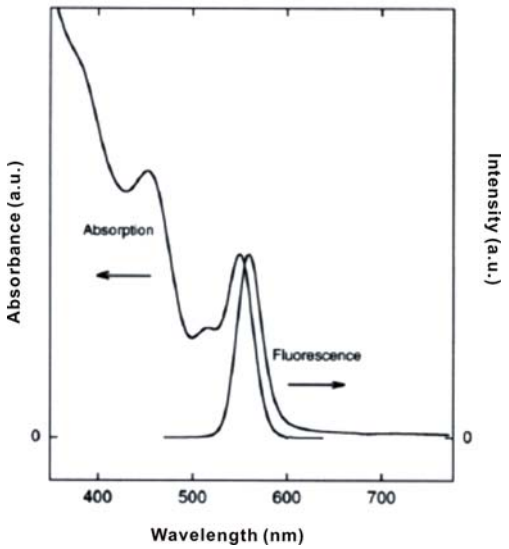

Figure 1.5 Typical absorption and emission spectrum of 3.5 nm CdSe NCs from ref.[16] The sharp absorption feature suggests a highly monodisperse sample.

The absorption spectra can be used to estimate the particle size as well as the crystal concentration, the absorption cross-section and extinction coefficient. The methods and data were well established by several research groups.[30-32, 34] In example, in Figure 1.5 the CdSe sample with the first absorption peak at 545 nm leads to a size of around 3.8 nm. The concentration of sample can be estimated by measuring the optical density of the first absorption peak. The working tables of absorption and extinction coefficient versus size are listed in the appendix section 7.1.

The fluorescent emission observed for CdSe QD is a typical sharp peak with a small Stokes shift corresponding to the band gap or near band gap emission resulting from the recombination of the electron-hole pair. The recombination or relaxation of the electron-hole pairs can be followed by several processes like radiative recombination (fluorescent emission), recombination by trap states or annihilation of the exciton or Auger processes.[16] These processes are shown in Figure 1.6. After absorption of a photon, an electron is excited to the energy levels on the excited states, and this is followed by a picoseconds nonradiative vibrational relaxation process, bringing the electron to the lowest excited state. This process can be followed by fluorescence emission using fluorescence lifetime measurement in the nanosecond regime, where a photon is emitted and the system relaxes to the ground

state. Due to trapping of electrons (holes) by trap states within the band gap of the QD, there are additional ways for the relaxation of the electron which results in the weak red shifted fluorescence or nonradiative relaxation. That corresponds to a much broader band at longer wavelengths, which is often observed for QDs with many surface defect states. This red shift often disappears after proper passivation of the surface, for instance, by an organic or inorganic shell.[35]

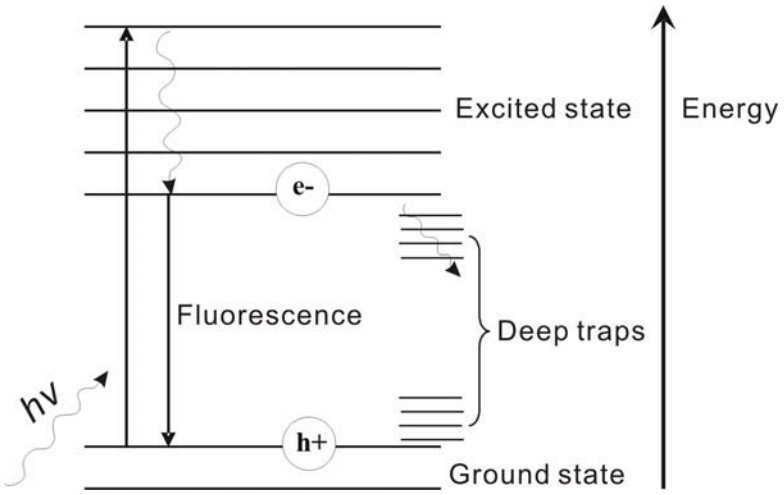

Figure 1.6 Schematic presentation of fluorescence emission process: the path for absorption of light, vibrational relaxation and radiative recombination or alternative relaxation through trap states.

1.2.2 Synthesis and surface modification of QDs

1.2.2.1 Synthesis of QDs CdSe/ZnS

Among the range of available QDs, the one comprised of CdSe cores and overcoated with a layer of ZnS, are most often used in the biological applications. Although the group II-VI semiconductor QDs have been synthesized in a controllable way for many years,[36-38] the real breakthrough in synthesizing high quality colloidal QDs was reported by Bawendi and colleagues in 1993.[16] They developed a synthetic strategy of high-temperature growth ligands (mixture of trioctylphosphine/trioctylphosphine oxide, TOP/TOPO) combined with pyrolysis of organometallic precursors, yielding CdSe NCs with high crystalline cores and nearly monodisperse. Peng and colleagues modified this synthesis by replacing the initial cadmium precursor dimethyl cadmium ($Cd(CH_3)_2$) by a less toxic and cheaper cadmium source, cadmium oxide (CdO) and achieved even higher quality QDs.[39] The growth mechanism of CdSe QD consists a nucleation from the homogenous precursor organic solution and the Ostwald ripening process. Precursors of cadmium are first coordinated in TOPO/HPA/TDPA

(trioctylphophine oxide/hexylphosphonic acid/tetradecylphosphonic acid) at high temperature of ~350°C before the injection of the selenium, which is dissolved in TBP (tributylphosphine). The nucleation takes place rapidly right after injection and continues until the temperature and monomer concentration drop below a critical threshold.[39, 40] Figure 1.7C illustrates the growth of the CdSe NCs with addition of TOP/TOPO coordinated Cd and Se ions on the surface.[41] Figure 1.7B is a high-magnification image of a 6.5 nm CdSe NC, which allows us to see the atoms in the NC structure. The symmetry of the crystallite as well as the hexagonal shape of the unit cell is evident.[42]

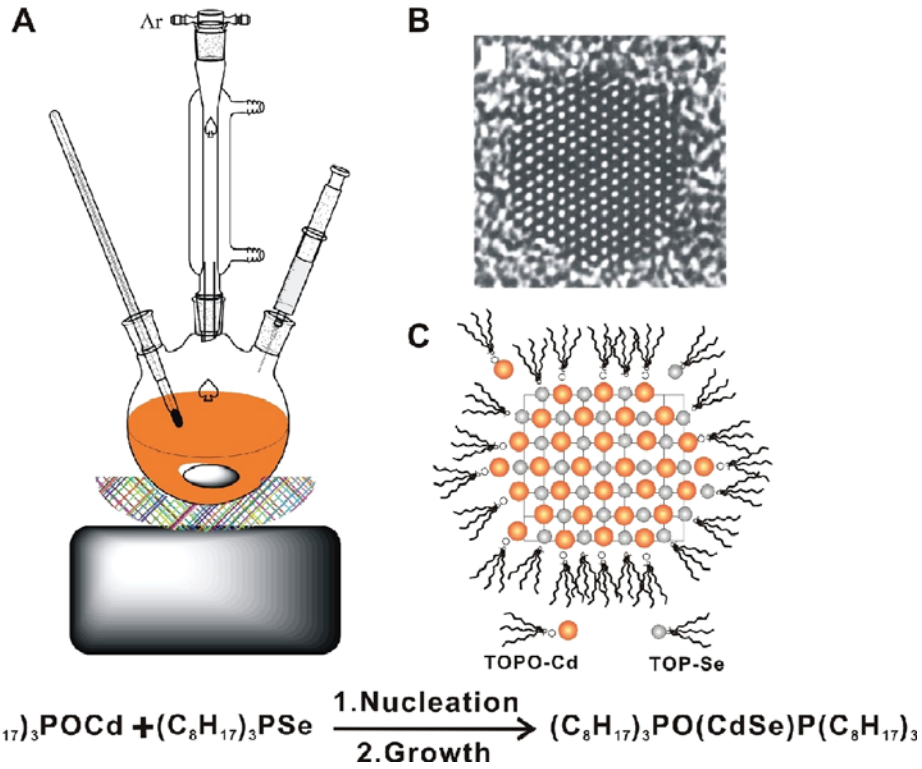

Figure 1.7 Synthesis of CdSe QDs. A) Typical apparatus for preparation of high-quality CdSe by a high-temperature route. The organic ligands are heated in the three-neck flask in an argon atmosphere. B) High resolution TEM image of one CdSe nanocrystal viewed along [001] zone axis (c-axis of the wurtzite lattice).[42] C) Schematic representation of a CdSe NC. The surface is capped with TOP/TOPO due to the influx of Cd and Se ions selectively bound to the surfactant molecule TOP/TOPO. Selenium is assumed to be bound to TOP whereas cadmium is assumed to be bound to TOPO, according to Peng et al.[43]

The growth of CdSe NCs will continue when the temperature remains above ~200 °C. Once the reaction mixture is cooled down, the growth of QD can be stopped. For the production of larger monodisperse QDs, a second injection can be used.[40] Both the average size and the size distribution of

NCs in one sample are dependent on the growth temperature, which is consistent with the surface free energy considerations. The growth temperature maintains the steady growth of NCs and increases with increasing average crystal size. As illustrated in Figure 1.8A, the La Mer model shows that the production of monodisperse colloids requires a temporally discrete nucleation event followed by a slower controllable growth on the existing nuclei.[44, 45] A rapid injection of the reagents to the reaction system helps to raise the precursor concentration above the nucleation threshold. A short nucleation burst then partially relieves the supersaturation. As long as the precursors are consumed, the concentration condition is not satisfied to form new nuclei. The second stage that determines the final size distribution of the NCs is the so-called Ostwald ripening.[46, 47] In this stage, the small NCs with a high surface energy will dissolve and the material is redeposited on the larger NCs. The average crystal size increases and the size distribution becomes narrower over time. Figure 1.8B is a plot of a model that describes this Ostwald ripening process.[48] In this model, at any given precursor concentration, there exists a critical size, which is at equilibrium. NCs smaller than the critical size will dissolve (negative growth rate), while larger ones will grow at different rates dependent on their size. The biggest rate of growth happens when the NCs are slightly larger than the critical size. These effects of NCs growth all lead to a better size distribution and ideally yield monodispersity of the particles.

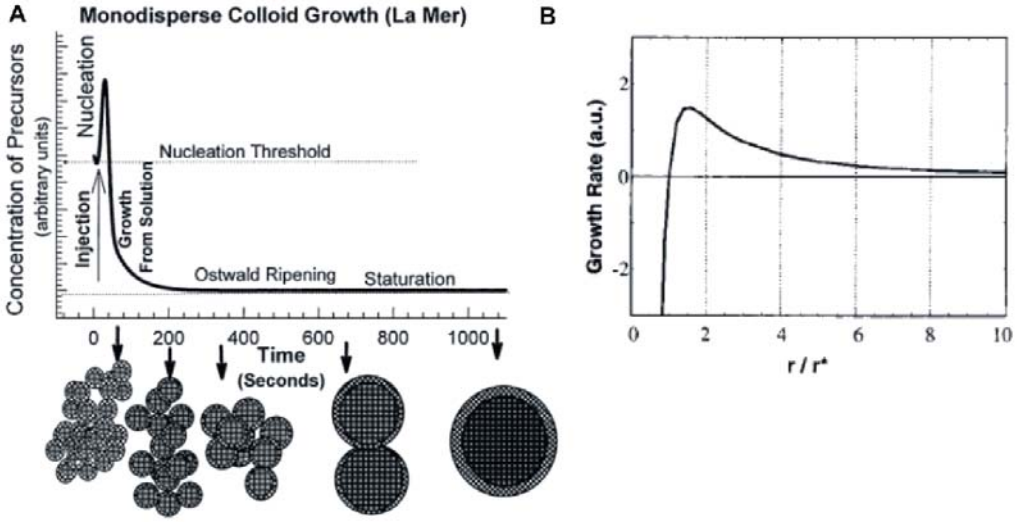

Figure 1.8 (A) Cartoon depicting the stages of nucleation and growth for the preparation of high-quality QDs in the framework of the La Mer model. As NCs grow with time, a size series of QDs may be insolated by periodically removing aliquots from the reaction vessel. (Adopted from Bawendi et al.[45]) (B) Variation of the growth rate versus size, according to kinetics study of colloidal semiconductor NC growth by Peng et al.[40]

To achieve a higher quantum yield and better protection of the CdSe from oxidation or Cd/Se leaking, a capping ZnS layer is usually grown on the top of the nanocrystal core.[35, 49] This modification also enhances QDs' photostability by several orders of magnitude, as compared with organic dyes.[50] The high surface atom ratio of NCs suggests that the surface properties will have significant effects on their structural and optical properties. Although a surface capping with organic or inorganic layers has been found to influence only mildly the absorption property, it is well-known that the photoluminescence efficiency, spectrum, and life time evolution are strongly affected by the surface states. This is possibly due to the presence of gap surface states caused by surface nonstoichiometry, unsaturated bonds, etc.[49] A proper control of the surface is the key to achieve highly luminescent QDs. After overcoating with the larger band gap semiconductor material ZnS, QDs with quantum yields in the range of 60-85% can be obtained.[51]

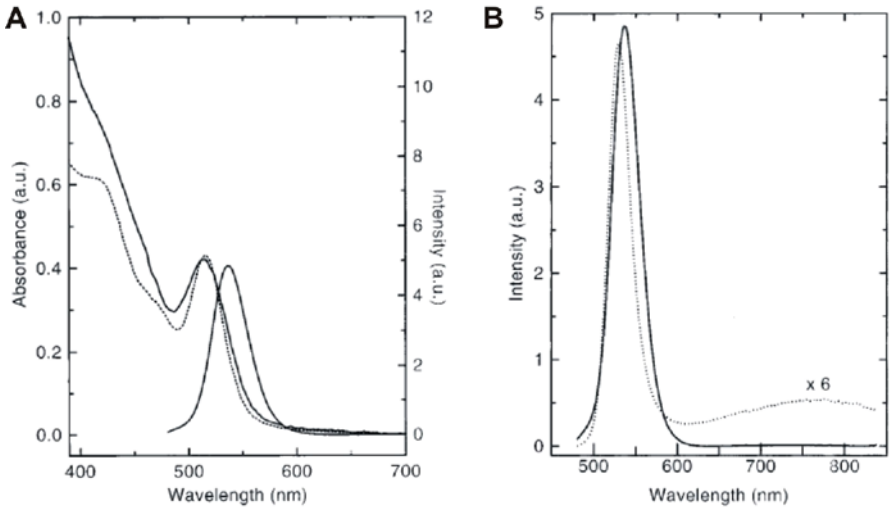

Figure 1.9 Absorption and photoluminescence spectra of sample CdSe before and after overcoating with ZnS. (A) Absorption spectrum of the CdSe/TOPO (dotted line) and the CdSe/ZnS NCs (solid line). The fluorescence of the CdSe/ZnS is also shown (solid line). (B) Fluorescence of the TOPO-CdSe (dotted line) and CdSe/ZnS (solid line) NCs is normalized by their absorption at the excitation wavelength (470nm).[49] The thickness of ZnS shell also influence the quantum efficiency of QDs and it was reported by Bawendi et al that the highest QY achieved when capping CdSe with ~1.3 monolayer (~0.4 nm) of ZnS.[35]

The ZnS layer is usually grown on the top of the previously prepared CdSe core using dimethylzinc (Me_2Zn) and bis(trimethylsilyl) sulfide ($(TMS)_2S$) as precursors in TOP/TOPO mixture solvent at a temperature of 200 °C.[49] The capping process has little modification of the CdSe core but only introduces the new crystallite on the CdSe surface. This was confirmed by the very little differences of

the absorption spectra before and after capping. However, it was observed that the quantum yield has been significantly improved after capping of ZnS and the fluorescence spectrum of CdSe/ZnS retained the sharp peak with a small red shift (~5 nm). This effect implied that the ZnS capping had passivated the surface nonradiative recombination sites still present in CdSe. Compared with the organic overcoating, the inorganic shell seems more robust and has greater tolerance to processing harsh conditions in biological applications. Figure 1.9 illustrates the comparison of the absorption spectra and photoluminescence spectra of CdSe and CdSe/ZnS, prepared by Hines et al.[49] The quantum yield of CdSe/ZnS is ~6 times of that of CdSe.

1.2.2.2 Surface modification of QDs CdSe/ZnS

As described above, QDs are mostly prepared in nonpolar organic solvents. If they are to be solubilized in aqueous buffers, the hydrophobic surface coating must be replaced by amphiphilic ligands. Solubilization and surface-functionalization of QDs are essential for many biological applications, but this process requires sophisticated surface chemistry, which is often a significant challenge. Various QDs solubilization strategies have been developed over the past decades.[13, 14, 18, 52, 53] These strategies generally can be grouped into two types. The first approach uses ligand exchange of the original hydrophobic surfactant ligands by hydrophilic molecules. The most often applied molecules are thiol-containing compounds, such as monothiolated ligands (i.e. mercaptoacetic acid),[54, 55] or bidentated thiols (dihydrolipoic acid derivatives)[56-58], or more sophisticated ones, such as alkylthiol terminated DNA[59], thioalkylated oligo-ethyleneglycols[60]. The advantage of this method is only leading to a small increase in hydrodynamic diameter (HD) of QDs due to the introduction of a thin coating. This is of strong interests for QD-based FRET investigation[17, 61] or some biological applications which require high diffusional mobilities.[62, 63] However, there are obvious drawbacks of this method, the stability of the thin ligand shell is often influenced by local environment, such as pH, salt concentration, etc. and these QDs are difficult to disperse in the cytosol of cells.[56, 63, 64] Recently, some new approaches by using similar thiol-containing molecules as DL-cysteine,[65] poly (ethylene glycols)-terminated dihydrolipoic acid (PEG-DHLA)[66] have been developed for solubilization and functionliazation of QDs and achieved significant *in vitro* and *in vivo* stability.[67-70] The second strategy for solubilization is based on encapsulation into a layer of amphiphilic diblock[71, 72] or triblock copolymers,[73] phospholipid micelles,[74-76] silica shells,[77, 78] dendrimers,[79] or amphiphilic polysaccharides,[80] polymer shells,[81] oligomeric phosphine coating,[82] or by phytochelatin-peptides coating,[83] or histidine-rich proteins.[84]

Such encapsulated QDs certainly benefit from high photoluminescence efficiency and improved stability, but the thick overcoating also produces large hydrodynamic diameters in the range of 20-30 nm for a 4-6 nm core/shell QD. This is often much larger than the cellular receptors being labeled, thereby prohibiting the widespread implementation of QDs for biological imaging. Furthermore, large particles will potentially interfere with the function of proteins being labeled and they might limit access to hindered regions such as neuronal synapses.[85, 86] Finally, the non-specific binding of these thick shell QDs to cell organelles are often severe due to the high surface charges which prevent them from using in single-particle tracking applications.[70] PEG-DHLA functionalized ligands have been synthesized by conjugating a short PEG (5, 8, 12 or 15 repeating units) to DHLA and used to cap QDs by Mattoussi et al (Figure 1.10).[66] It was observed that PEG-DHLA capping of QDs dramatically improves the stability and limits the nonspecific interactions in biological environment. The most precious advantage of this strategy is that hydrodynamic diameter (HD) of the capped QDs is only a few nanometers larger than the inorganic core (i.e. HD ~9.9 nm for a 565 nm-emitting QD). This strategy has been found to comprise both advantages of thin coating and enhanced stability and biocompatibility and has excellent potential applications for *in vitro* and *in vivo* biological imaging or sensing.[67-70, 87]

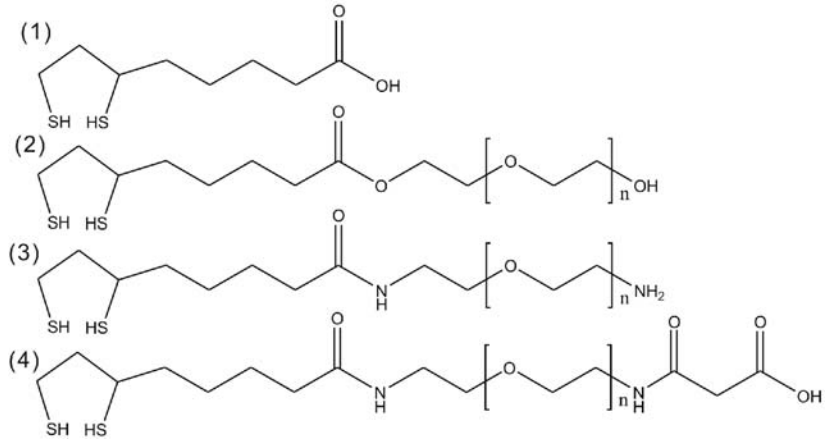

Figure 1.10 Scheme for dihydrolipoic acid (DHLA) molecule (1) and poly (ethylene glycols)-terminated dihyrolipoic acid (PEG-DHLA) with hydroxyl (2); amino (3) and carboxyl (4) functional groups. Synthetic multidentate molecules for solubilizing and functionalizing QDs. n=5, 8, 12 or 15, etc.[66, 70]

1.3 Luminescent quantum dots (QDs) for Fluorescent resonance energy transfer (FRET)

1.3.1 Fundamentals of FRET

Fluorescence (or Förster) Resonance Energy Transfer (FRET) is a process in which energy is transferred by a nonradiative, long-range dipole-dipole coupling from a fluorophore in an excited state serving as a donor, to another proximal ground state acceptor (Figure 1.11). Because FRET usually occurs over distances realized in the interaction between most biomolecules, that is typically in the range of 1-10 nm, it is a powerful spectroscopic tool to interrogate changes in molecular conformation, association, and the assembly or disassembly of biomolecular machinery.[61, 88, 89] One requirement for the spectroscopic properties of the involved chromophores is that the emission spectrum of the donor and the absorption spectrum of the acceptor need to exhibit a significant overlap for FRET to occur.

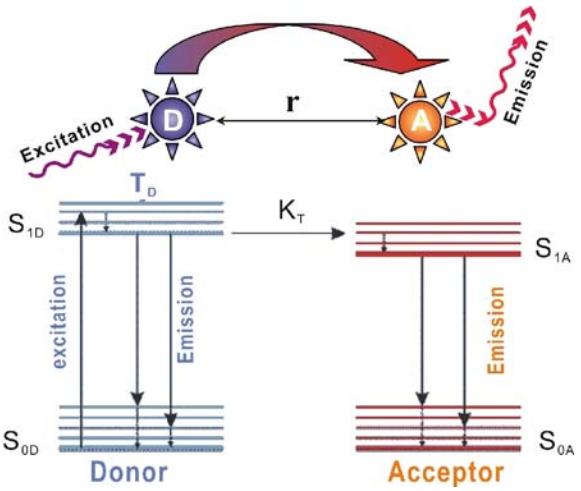

Figure 1.11 Schematic of the FRET process. Upon excitation, the excited state donor molecule transfers energy nonradiatively to a proximal acceptor molecule located at distance of *r* from the donor. The acceptor releases the energy through fluorescence or other nonradiative channels. The diagram shows the energy levels of the donor and acceptor and the rates and states involved in FRET.

The quantitative study of FRET requires the knowledge of distinct parameters, such as the Förster radius and energy transfer rates. For 2-Chromophore-FRET (2Ch-FRET) systems, where a single exciton donor can interact with several acceptors, the energy transfer efficiency depends on the molar ratio of acceptor and donor. *E* can be expressed as

$$E(N,r)=\frac{N}{N+\left(\frac{r}{R_0}\right)^6} \qquad 1.1$$

where N is the average number of acceptor molecules per one donor molecule.[88, 90] For simple FRET pair with one donor and one acceptor molecule, N=1. In some more complicated cases, especially FRET involves nanoparticle donors, in which multiple acceptor molecules can be immobilized on one nanoparticle donor, N is the number of acceptor. The Förster radius R_0 defined as the distance between donor and acceptor that yields 50% energy transfer efficiency, can be calculated as,[88]

$$R_0^6 = 8.8\times10^{23}\kappa_p{}^2 n_D{}^{-4} Q_D J \qquad 1.2$$

where Q_D is the quantum yield (QY) of the donor in the absence of an acceptor, and n_D is the refractive index of the medium; $\kappa_p{}^2$ is an orientation factor, depending on the relative orientation of the donor and acceptor dipoles. $\kappa_p{}^2$=2/3 is the value for randomly oriented dipoles, which is suited for the systems investigated in this thesis.[91] The overlap integral J is a quantitative measure of donor-acceptor spectral overlap integrated over all wavelengths λ, and is defined as,[88]

$$J = \int f_D(\lambda)\varepsilon_A(\lambda)\lambda^4 d\lambda \qquad 1.3$$

where f_D and ε_A represent the donor emission spectrum (normalized and dimensionless) and acceptor absorption spectrum, respectively. Experimentally, the efficiency E of a FRET process can, for example, be derived from the quenching of the donor fluorescence intensity, according to[88]

$$E = 1-\frac{F_{DA}}{F_D} = 1-\frac{\tau_{D-A}}{\tau_D} = \frac{k_{transfer}}{k_{rad}+k_{nonrad}+k_{transfer}} \qquad 1.4$$

where F_D and F_{DA} are the fluorescence intensities of the donor in the absence and presence of an acceptor; $\tau_{D\text{-}A}$ and τ_D are the fluorescent lifetimes of the donor in the absence and presence of an acceptor. k_{rad}, k_{nonrad} and $k_{transfer}$ are the radiative and nonradiative recombination rates and the transfer rate of the donor, respectively. Alternatively, the efficiency E can be determined by the luminescence enhancement (if the acceptor is a fluorescent molecule), expressed as[92]

$$E = \frac{A_A(\lambda_D)}{A_D(\lambda_D)}\left[\frac{F_{AD}(\lambda_A)}{F_A(\lambda_A)}-1\right] \qquad 1.5$$

where λ_D is the donor excitation wavelength; A_D and A_A are the donor and acceptor absorbance at the wavelength λ_D; F_{AD} and F_A are acceptor fluorescent intensities at the acceptor emission wavelength λ_A in the presence and absence of a donor.

As an example for the 2Ch-FRET system, Kukolka and co-workers reported the assembly and spectroscopic characterization of various unique FRET systems, which were constructed by means of DNA hybridization using the enhanced yellow fluorescent protein (EYFP) as the donor and the organic fluorescent dye Atto647 as the acceptor for energy transfer (Figure 1.12).[93] In these systems, the interchromophore distance of donor and acceptor can be conveniently changed by variation of the binding sites of the fluorophores at the DNA "carrier" helix.

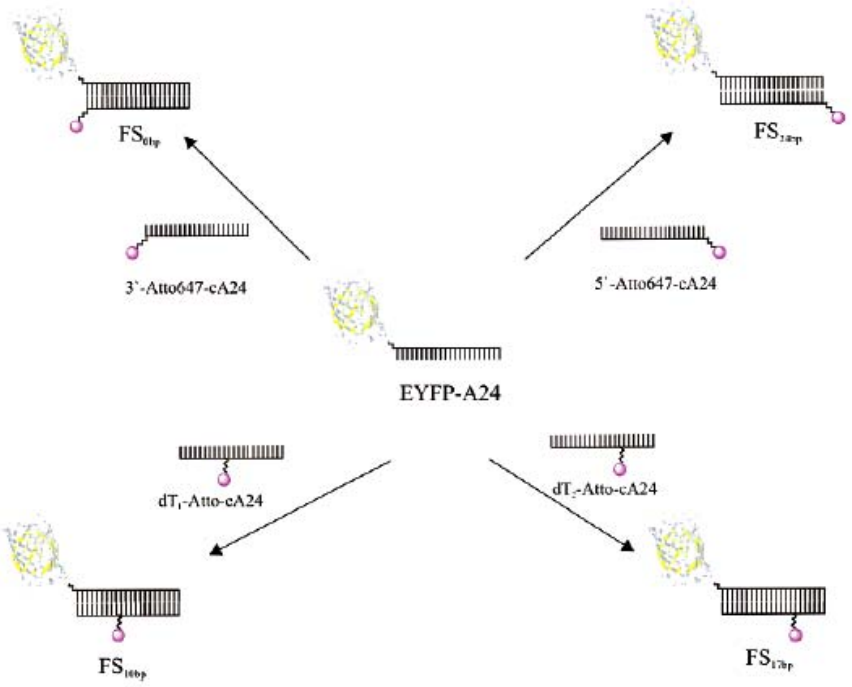

Figure 1.12 Schematic representation of a 2-chromophore FRET system EYFP/Atto647. In this FRET system, EYFP serves as an energy donor, Atto647-dye serves as an acceptor and the oligonucleotides-DNA bring the donor and acceptor together with a precisely controlling of the separation distances.[93]

A limitation of FRET studies usually stems from the fact that it only permits the analysis of interactions between two molecular entities. Many biochemical processes, however, involve multi-component molecular assemblies which are based on dynamic and highly coordinated supramolecular interactions. To study multi-molecular interactions within, for instance, biomolecular machineries, more complex FRET systems, in particular, three-chromophore FRET systems, have been developed, which enable the analysis of up to three mutually dependent energy transfer processes occurring between the fluorophores.[94-102] Other examples concern two-step FRET processes to achieve a higher efficiency in long-range energy transfer, larger spectral shifts between absorption and emission and improved

sensitivity, compared to the simpler one-step FRET.[103, 104] Thus, three chromophore FRET (3Ch-FRET) systems are considered to possess a great potential for elucidating biomolecular structure and dynamics. Figure 1.13 presents one example to demonstrate how a multiple FRET system of three fluorescent proteins elucidate the multi-protein interactions within some molecular machineries.[99]

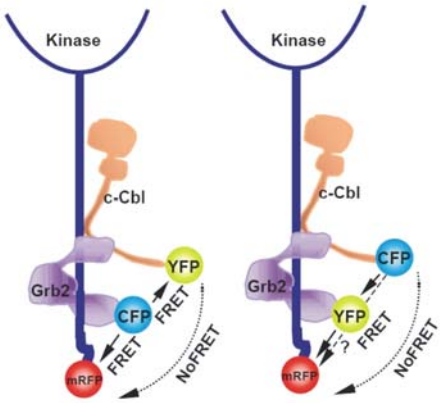

Figure 1.13 A multi-FRET application sample from Sorkin et al.[99]: a hypothetical model of one-step, parallel and sequential FRETs within the EGFR-Grb-Cbl complex based on three chromophore FRET system of CFP/YFP/mRFP.

1.3.2 Luminescent QDs for FRET investigations

As described above, luminescent semiconductor QDs are inorganic nanoparticle fluorophores with unique optical and spectroscopic properties that make them excellent fluorescent labels for biological imaging, sensing and diagnostics.[14, 15, 104] QDs possess a variety of advantages over conventional organic dyes, such as high quantum yields, excellent photo- and chemical stability, and size-dependent, tunable absorption and emission.[20] This also allows one to exploit them as donors and acceptors in energy transfer studies. In recent years, numerous advances have been achieved in QD-based FRET investigations, regarding both fundamental theoretical analyses and biological applications, including the design of biosensors and the analysis of biomolecular conformation and interaction.[17, 55, 61, 90, 91, 104-117] Mattoussi and co-workers have developed a series of dihydrolipoic acid (DHLA)-coated QD-based FRET system as biosensors. Figure 1.14 illustrates one multi-FRET QD maltose sensor. In this system, a 530 nm QD is surrounded by about 10 MBP molecules (only one is shown for simplicity), each labeled with a single Cy3 molecule. β-Cyclodextrin, an analogue of the primary maltose analyte, is labeled with Cy3.5 (β-CD-Cy3.5), which binds specifically in the binding pocket of MBP to complete

the sensor complex. Excitation of the QD results in excitation of the MBP-Cy3 (FRET 1), which in turn excites the β-CD-Cy3.5 (FRET 2). Added maltose displaces β-CD-Cy3.5 and leads to increased emission of Cy3. This sensor is 'driven' by a QD to achieve a better sensitivity and overcome inherent limitations of the D/A distance.[104]

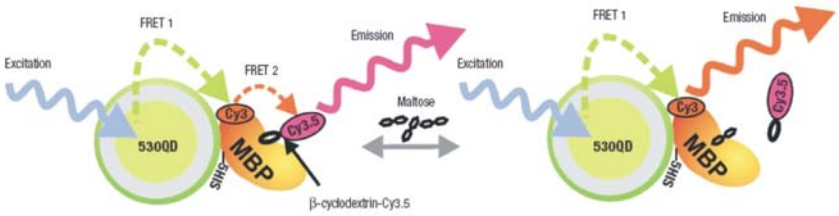

Figure 1.14 Schematic function of a multi-FRET QD maltose sensor-one QD-based FRET application sample from Mattoussi et al.[104] Each 560 nm emitting QD is surrounded by an average of ~10 MBP moieties; a single MBP is shown for simplicity. Formation of QD-MBP-β-CD-QSY9 (maximum absorption ~565 nm) results in quenching of QD emission. Added maltose displaces β-CD-QSY9 from the sensor assembly, resulting in an increase in direct QD emission.

It has previously been suggested that the combination of different types of fluorophores, such as inorganic luminescent nanocrystals, organic dyes, and genetically encoded fluorescent proteins offers a promising route for the fabrication of multi-chromophore systems.[61] In this thesis, a DNA-based three chromophore-FRET (3Ch-FRET) system was assembled and spectroscopically characterized. The system comprises three different types of fluorophores, that are luminescent QDs, enhanced yellow fluorescent protein (EYFP) and short single-stranded DNA (ssDNA) oligonucleotides tagged with the organic dye Atto647, all of which are common fluorescent tags in bio-labeling and bio-sensing.

1.4 Luminescent quantum dots (QDs) for cellular imaging

Fluorescent semiconductor QDs have been used for cellular labeling since last decade and attracted the greatest interest ever since.[54, 77] Within last few years, significant progress has been made describing the ability of single or multi color of biofunctionalized QDs to label living or fixed cells. Many of these advances show that QDs labeling allows a longer temporal imaging of cells with extended anti-photobleaching property, as well as multicolor imaging possibility under a single excitation source.[13, 14] For example, QDs have been used in immunofluorescence labeling of membrane proteins,[50, 71, 118, 119] microtubules,[71] actin,[71, 77] or nuclear antigens.[71] The big advantage of QDs is that they are brighter than

organic dyes due to the high extinction coefficient, which is much larger than those of most organic dyes. Additionally, they are resistant to bleaching over much longer period of time which is an extremely useful property for cellular imaging particularly for a long term *in vivo* tracking. Figure 1.15A illustrates the high resistance to photobleaching and photo degradation of Qdots® from Invitrogen compared with organic dye.

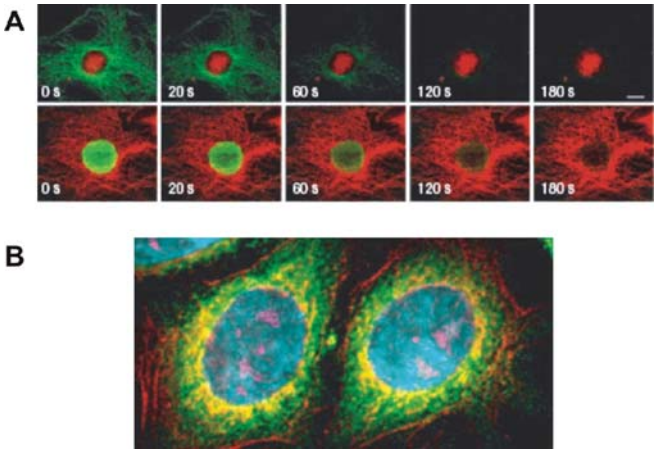

Figure 1.15 QD's resistance to photobleaching and multicolor labeling. (A) Photostability comparison between QDs and Alexa 488. Top row: Nuclear antigens were labeled with QD 630-streptavidin (red), and microtubules were labeled with Alexa 488 conjugated to anti-mouse IgG (green) simultaneously in a 3T3 cell. Bottom row: Microtubules were labeled with Alexa 488 conjugated to anti-human IgG. The specimens were continuously illuminated for 3 min with light from a 100 W mercury lamp. Images were captured with a cooled CCD camera at 10s intervals for each color automatically. Scale bar, 10 μm.[71] (B) Pseudocoloured image depicting five-color QD staining of fixed human epithelial cells. Cyan corresponds to 655-nm QDs labeling nucleus, magenta 605-QDs labeling Ki-67 protein, orange 525-QDs labeling mitochondria, green 565-QDs labeling microtubules and red 705-QDs labeling actin filaments.[13]

Another unique advantage of QDs for the cellular imaging is that QDs of different sizes can be used for labeling different organelles of the same cells and observed with one excitation source. Figure 1.15B demonstrates a multicolor labeling of the fixed cells. Five functionalized QDs with different fluorescent emissions were used to stain five different parts of the fixed human epithelial cells. The cells can then be excited with a single wavelength for all the five QDs.[13]

Whole organism imaging was achieved by Dubertret and co-workers on small *Xenopus* embryos containing intracellular QDs.[74] Phospholipid micelle-stabilized QDs were microinjected into *Xenopus* embryos and showed the cell lineage-tracing during the developmental process spanning the embryo-

tadpole stage and equal transfer of QDs from mother to daughter cells (Figure 1.16). This experiment also demonstrated the long-term cellular compatibility and photo and chemical stability of phospholipid micelle-stabilized QDs.

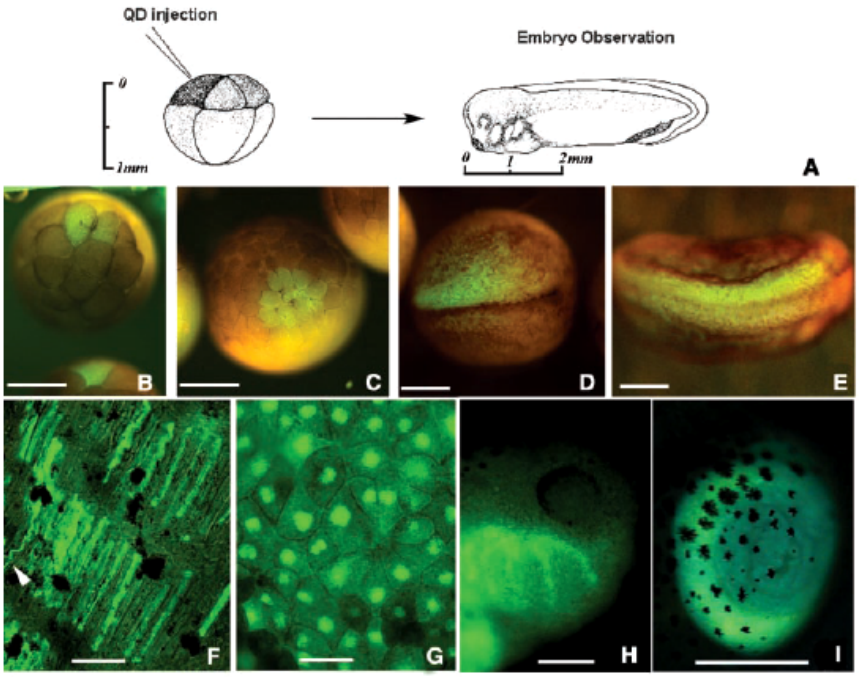

Figure 1.16 QD labeling of *Xenopus* embryos at different stages and specific QD intracellular localizations. (A) Schematic showing the experimental strategy. Phospholipid micelle-stabilized QDs were microinjected into an individual blastomere during very early cleavage stages. (B) Injection of one cell out of an eight-cell-stage embryo resulted in labeling of individual blastomeres. (C) Same embryo shown 1 hour later. The daughter cells of the injected blastomere are labeled (D) and at a later stage (E) show two neurula embryos, which were injected into a single cell at the eight-cell-stage in the animal pole. The QDs can be visualized through the pigmented layer of the epidermis. (F) Intracellular labeling of an axon and somites at tadpole stage 40. The QDs migrate into axons all the way to growth cones. In the somites, the QDs seems to be localized in subcellular structures. (G) QDs localized in the nucleus during mid-balstula stages. (H) Labeled neural crest cells migrating into the branchial arches. (I) QD fluorescence observed in the gut of an injected embryo. Bars: (B) to (E), (H) and (I), 0.5 mm; (F) and (G), 30 µm.

The luminescent QDs have the potential to revolutionize biological imaging. Despite the drawbacks such as large hydrodynamic diameter and cytotoxicity, which may be overcome with the advances of new synthetic and surface-modification techniques, QDs unique properties can complement the

disadvantages of well-established fluorophores or fluorescent proteins for the applications in which photostability, NIR emission,[120, 121] or single-molecule sensitivity[122] over long time scales are required.
As a solid phase, a single QD allows attachment of multiple proteins, which actually serves as a nanoscaffold and provides the possibility for creating a multifunctional nanoparticle-biological hybrid. Conjugation strategies for attaching proteins to QDs can normally be grouped into three categories, depending on the capping strategies for QDs.[13] (i) EDC coupling, 1-ethyl-3-(3-dimethylaminopropyl) carbodiimide, condensation to react carboxy groups on the QD surface to amines on biomolecules; (ii) direct binding of thiolated peptides or polyhistidine residues to the QD surface; (iii) electrostatic adsorption or non-covalent assembly using some engineered proteins. The limitation of the EDC coupling method is the difficulty to control the crosslinking and aggregation of QDs, because there are numerous surface functional sites on one QD, which possibly bind or crosslink the numerous protein target sites. Nevertheless, this strategy was widely used to prepare commercial QD-protein conjugates. For example, the Qdots® (Invitrogen Co.) straptavidin conjugates were prepared by coupling multiple straptavidin molecules on carboxyl functionalized polymer coated QDs through EDC linker.[71] Direct binding based on thiol-bonding between QD surface sulphur atoms and cysteine residues[84, 118] or Zn-affinity coordination of histidine residues to QD surface Zn atoms or Ni-NTA functional groups were also often used.[75, 83, 90, 106, 123, 124] The use of the histidine residues limits some of the proteins binding to QDs. Engineering proteins to express positively charged domains provide the possibility to self-assemble onto the surface of negatively charged QDs (e.g. DHLA-QDs) through electrostatic assembly.[56, 125] However, these assembly were easily effected by the pH or salt concentration changes.

1.5 Aim of this work

As discussed above, it is of outmost importance to prepare robust, water-solubilized and functionalized QDs in order to enable controllable properties for biological applications. Therefore, the main objective of this work was to synthesize and surface-modify luminescent CdSe/ZnS QDs.
The desired QDs should possess high photoluminescence quantum yield, narrow size distribution and a chemically accessible surface to allow the binding of biomolecular moieties. To this end, it has been decided to use the classic synthetic route of pyrolysis strategy with Cd/Se precursors to prepare CdSe QDs with enhanced fluorescence and high quality crystallization. In order to passivate the surface traps of the CdSe NCs and protect them from chemical-degradation, an inorganic shell of ZnS was grown on the top of CdSe. The resulting CdSe/ZnS NCs were dispersed in organic solvent such as chloroform or

hexane. To make them water-soluble, several strategies can be applied to render the QDs into aqueous solution and to introduce a range of functional groups. A ligand-exchange strategy with dihydrolipoic acid and a phospholipid micelle-coating strategy can be applied to make the CdSe/ZnS water-soluble (Figure 1.17). Based on the different characters of these two types of functionalized QDs, the DHLA-coated QDs with reduced hydrodynamic size are suitable and were chosen for FRET-based biosensor study. To this end, the DHLA-coated QDs should be used for the assembly of a QD-fluorescent protein donor system for a multi-FRET study. The highly stable phospholipid micelle-stabilized QDs with thick coating should be investigated for their use in cellular imaging to study the prenylation mechanism of Rab7 protein.

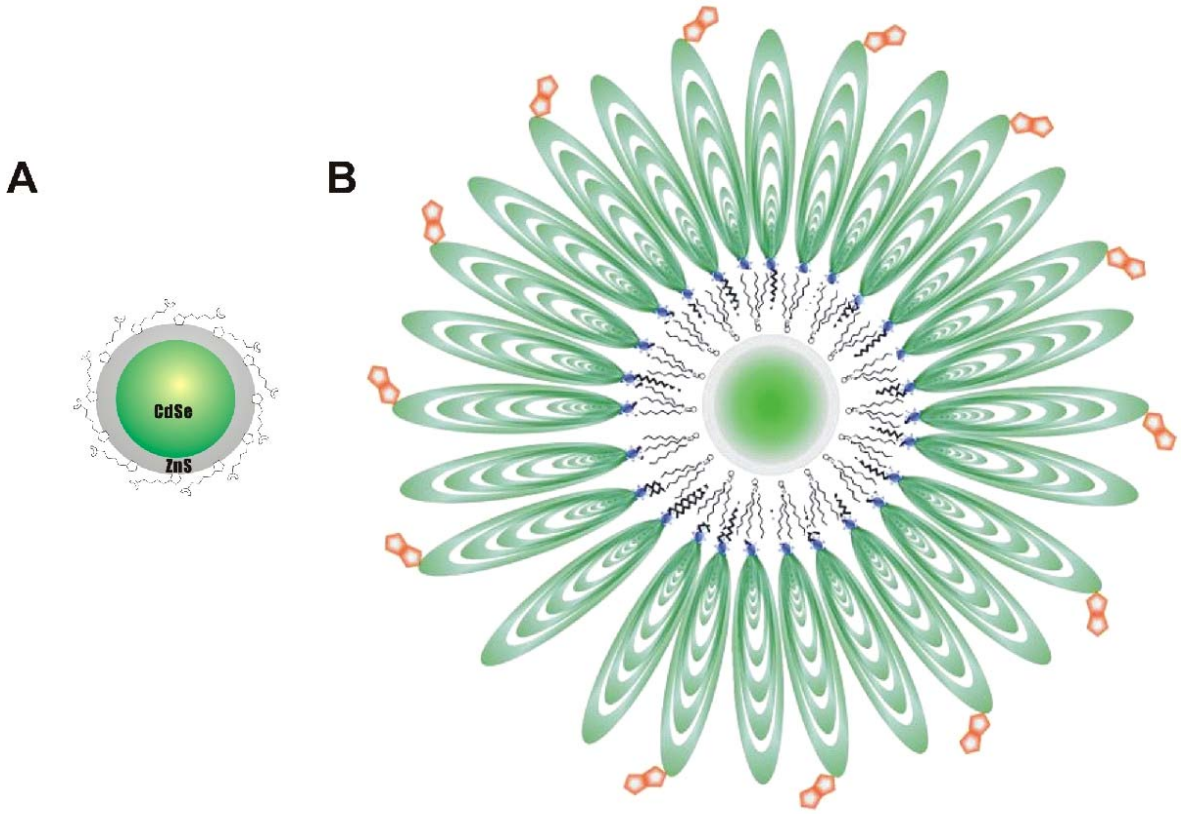

Figure 1.17 Schematic representation of solubilized and functionlized QDs. (A) Dihydrolipoic acid-coated CdSe/ZnS QDs. (B) phospholipid micelle stabilized CdSe/ZnS QDs with functional groups.

2 Results and Discussion

2.1 Synthesis and Characterization of QDs CdSe/ZnS

A wide variety of QD synthesis protocols have been developed, and the synthesis of CdSe QDs represents the most investigated and the best understood system. Most of the synthesis strategies involve a pyrolysis of the cadmium and selenium precursors in the presence of a ligand that binds to the resulting nanocrystal surface to sterically stabilize them from aggregation or to prevent growth into bulk semiconductor. In this chapter, the structure and synthesis strategy of QDs CdSe/ZnS are described and discussed. The general aim was to achieve a reproducible and robust synthetic route for the preparation of luminescent CdSe/ZnS NCs.

2.1.1 Structure of QDs CdSe/ZnS

The semiconductor nanocrystal was formed by a core composed of cadmium selenide (CdSe), and a shell overcoating of a material such as zinc sulfide (ZnS), cadmium sulfide (CdS) or zinc selenide (ZnSe). The particles were normally capped by a protecting layer of organic molecules (ligand molecules), which stabilize the nanocrystals (NCs) in solution. The trioctylphosphine (TOP) and trioctylphosphine oxide (TOPO) are such binding ligands, which chemisorb on the QD surface when these crystals form and grow in the TOP/TOPO solvent. Core/shell type QDs CdSe/ZnS were prepared by overcoating the CdSe NCs with a higher band gap material ZnS to improve the photoluminescence quantum yield by passivating surface nonradiative recombination sites.[35, 49] Other core-shell NCs examples where inorganic materials are used as overcoating include CdS on CdSe and CdSe on CdS,[126] ZnSe overcoated CdSe[127] and SiO_2 on Si.[128] Compared with surface passivation by organic ligands, these inorganic shell structures are more robust and can provide better protection from photooxidation and fluorescent quenching for the cores. The ZnS shell confines the deep trap emission by passivating the surface vacancies and the trap sites on CdSe, resulting in improved luminescence and higher stability and electrical connection. The core/shell structure QD is schematically depicted in Figure 2.1.1. In this work the previously reported two-step protocol[16, 39, 129] was used to prepare CdSe/ZnS. The CdSe core was first prepared utilizing pyrolysis of organometallic reagents by injecting Se precursor to high temperature Cd precursor solution of TOP/TOPO. The subsequent overcoating step was carried out by slowly growing of the ZnS onto the already formed CdSe core.

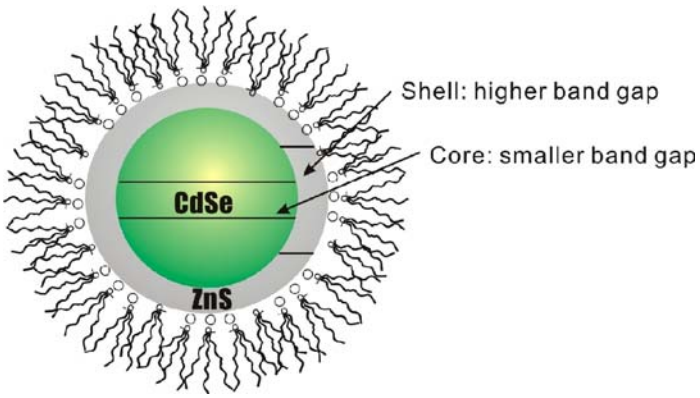

Figure 2.1.1 Schematic representation of a core-shell structure QD CdSe/ZnS. The ZnS shell possess a higher band gap than CdSe core confining the excitons and holes inside the core. Surface is capped with an organic molecule TOP/TOPO.

2.1.2 Synthesis of CdSe core

In the development of QD synthesis, the main task of this work was to obtain a controllable and reproducible method for the preparation of the CdSe cores of uniform size and properties. The pyrolysis synthetic strategy developed by Bawendi and co-workers in 1993 is a simple route to the production of high-quality cadmium chalcogenides quantum dots.[16] The synthesis combines a homogeneous nucleation with a rapid injection of organometallic reagents into a high temperature coordinating solvent and a slow growth and annealing in the coordinating solvent, which results in uniform surface derivatization and regularity in the size and core structure. Peng and co-workers used CdO as cadmium precursor instead of the extremely toxic, pyrophoric and expensive dimethyl cadmium ($Cd(CH_3)_2$) and this one-pot synthesis of high-quality CdE (E=S, Se, Te) was much more economic and easily scaled-up.[39]

The synthesis method used in this thesis is based on usage of CdO and TOPSe precursors and dodecylamine (DDA), tetradecylphosphonic acid (TDPA) and TOPO as coordinating ligand molecules similar to procedure described by Peng et al.[39] At the temperature of around 300 °C, CdO powder was first dissolved in the organic ligands TOPO/DDA/TDPA generating a colorless homogeneous solution. The nucleation of CdSe NCs took place immediately after injection of TOPSe which was prepared prior to injection by dissolving Se powder in TOP. The initial nucleation stage in this procedure is slower than that when $Cd(CH_3)_2$ is used as precursors because the Cd-DDA/Cd-TDPA/Cd-TOPO are more stable than $Cd(CH_3)_2$. The slow initial nucleation rate is an advantage for a reproducible

preparation of high crystal quality CdSe.[39] It is well known that the band edge luminescence energy of CdSe depends strongly on the size and therefore this property was used to assess the time evolution of the growth process. Usually, nucleation takes place right after injection and continues until the temperature and precursor concentration drop below a critical threshold. The kinetics of nucleation are difficult to study,[40] whereas the subsequent growth of NCs can be investigated more readily. As discussed in the introduction chapter (Figure 1.8), this process is based on Ostwald ripening or defocusing by which the growth of the NCs is controlled.[48] During this period of time, the higher surface free energy of small crystallites makes them less stable with respect to dissolution in the solvent compared to larger crystallites. The result of this process is to sharpen the size distribution of the NCs and produce of high quality QDs. With the constant addition of the precursors, the monodisperse CdSe crystals of desired size can be obtained by controlling the mixture temperature. In the experiments of this work, when the reaction mixture was cooled down below ~200 °C, the growth of the particles was stopped. The particle size of CdSe can be monitored by continuously taking aliquots of the reaction samples from the flask and measuring the UV-Vis absorbance (Figure 2.1.3).[30-32] For instance, a CdSe sample prepared in this work with the first absorption peak of ~570 nm leads to a particle size of ~4.5 nm based on the size-dependent properties. Figure 2.1.2 shows the typical photoluminescence spectrum of the sample of 4.5 nm diameter CdSe NCs in comparison with the absorption spectrum. The effect of quantum confinement can clearly be seen. CdSe absorption is shifted dramatically from its 716 nm bulk band gaps to three resolved transitions. The luminescence quantum yield for this sample is ~7.6% relative to Rhodamine 6G at room temperature. Briefly, the CdSe NCs were resolved in hexane and the fluorescence was compared with that of the Rhodamine 6G sample, which was diluted in ethanol to the same absorbance as the CdSe sample at 480 nm. There is around 15 nm red shift of the emission peak compared with the absorption maximum, which is the result of a combination of relaxation into shallow trap states and the size distribution.[130] The sharp absorption and emission features and the high quantum yield suggest highly monodisperse CdSe NCs with few surface electronic defects. The sharp luminescence is also a result of the efficient electronical passivation of the capping groups, which protect the individual NC from chemical degradation. Once capped with enough capping molecules, the CdSe NCs in this work are very stable and can be stored in organic solvent for more than one year.[16]

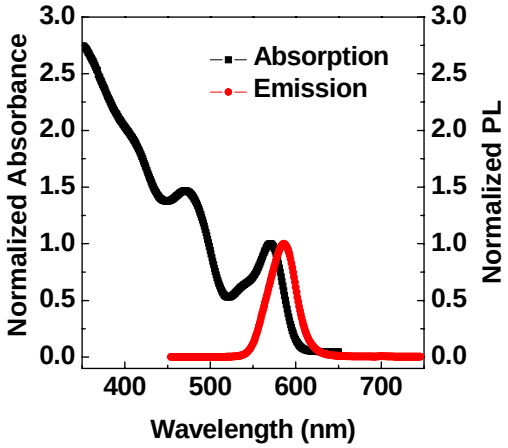

Figure 2.1.2 Typical room temperature absorption and emission spectrum of 586 nm-emitting QD CdSe prepared in this thesis (first absorption peak at 570 nm and emission maximum at 586 nm with a 350 nm excitation, FWHM=~35 nm, particle size of 4.5 nm in diameter, dispersed in chloroform).

Figure 2.1.3 shows the evolution of the UV-Vis absorption spectra for different size CdSe QD samples prepared in this work during the growth of the NCs at around 280 °C for different periods of time.

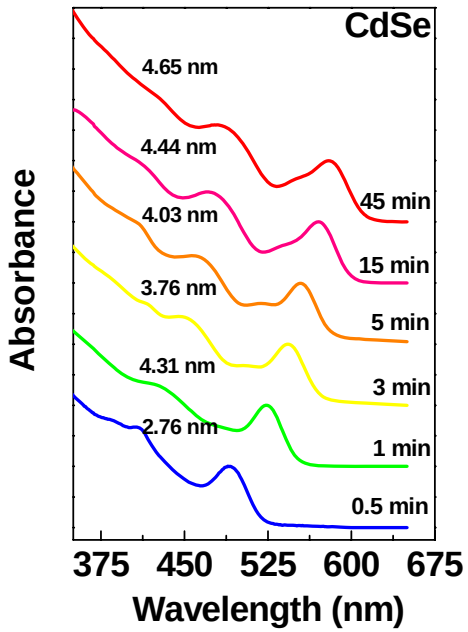

Figure 2.1.3 Room-temperature absorption spectra of CdSe NCs dispersed in chloroform and ranging size from ~2.76 to 4.65 nm versus the growth time at around 280 °C. The samples were all prepared using an identical protocol but varying reaction times.

The final CdSe particle sizes were ranging from ~2.76 to 4.65 nm (first absorption peak arranging from 490 to 590 nm) when the reaction time was ranged from ~30 sec to ~45 min at a growth temperature of ~200-280 °C. To prepare the small CdSe NCs, the temperature of the reaction solution should be well controlled below ~200 °C a few secs after injection of TOPSe to prevent the continuous growth of the crystals. Cooling the flask with cold water or injection of a few milliliter of *n*-butanol to the mixture are the two strategies used in this thesis to control the temperature. It is obvious that CdSe NCs even smaller than the samples prepared in this work are hard to synthesize directly with this method due to the difficulty to reduce the growth time. To obtain smaller NCs, it was reported that the initial precursor concentration or temperature have to be carefully controlled.[16, 39] For preparation of blue emitting QDs (emission less than ~490 nm), CdS/ZnS or other materials NCs can be good alternatives for CdSe.[131]

The resulting TOPO coated CdSe NCs were collected and purified by a size selective precipitation from organic solvent. The capping ligand layer provides an energetic barrier against aggregation of QDs, which strongly relies on the energy of mixing between the tethered groups and the solvent molecules. Addition of a polar but miscible solvent such as methanol destabilizes the NCs and causes precipitation. The NCs can be collected by centrifugation and subsequently washed to remove the free ligands and non-reacted precursors. The NCs can then be redispersed in organic solvents. This process can be repeated several times to get higher purities and narrow size distribution.[45] The particle concentration of the QD solution can be estimated from the UV-Vis absorbance and the extinction coefficient of the QDs. For example, the extinction coefficient of a 586 nm-emitting CdSe QDs sample at the first absorption peak, ~570 nm is 320,000 $M^{-1}cm^{-1}$,[30] and the sample solution of a UV-Vis absorbance of 0.5 at 570 nm indicates a particle concentration of 1.6 μM.

2.1.3 CdSe surface overcoating with ZnS and characterization of CdSe/ZnS

The strategies for overcoating a QD with a second semiconductor material of wider bandgap are well described. Particles passivated with inorganic shell structures are more robust than organically passivated NCs and have greater tolerance to some harsh conditions presented in biological media (e.g. high or low pH buffers or cellular organelles).

Diethylzinc ($ZnEt_2$) and bis(trimethylsilyl) sulfide ($(TMS)_2S$) were used as Zn and S precursors in this work. The amount of the two precursors were calculated prior to experiments based on the desired shell volume assuming a spherical core and shell and taking into account the bulk lattice parameters of CdSe

and ZnS (thickness of one monolayer of ZnS, 0.31 nm). The core size of CdSe was estimated from the absorption wavelength of the first absorption peak as described earlier.[30] The calculated amount of precursors was dissolved in TOP and was added very slowly to the reaction flask containing preheated CdSe dots dispersed in TOPO/TOP to enable the growth of ZnS on the CdSe cores. The control of the temperature at which the CdSe NCs are overcoated is crucial. At higher temperatures, the CdSe NCs will start to grow following the Ostwald ripening laws and the size distribution will become broader. At lower temperature, incomplete decomposition of the precursors could occur which leads to reduction of the crystallinity of the ZnS shell. The growth temperature used in the syntheses carried out here was ~150 °C, at which the CdSe seeds will not degrade and the ZnS shells are of high degree of crystallinity.[30, 35] The concentration of the Zn and S precursors and the rate of addition are also critical steps. Slow addition of the precursors at low concentration will avoid self-nucleation of ZnS and ensure that most of the ZnS grows heterogeneously on the CdSe cores.

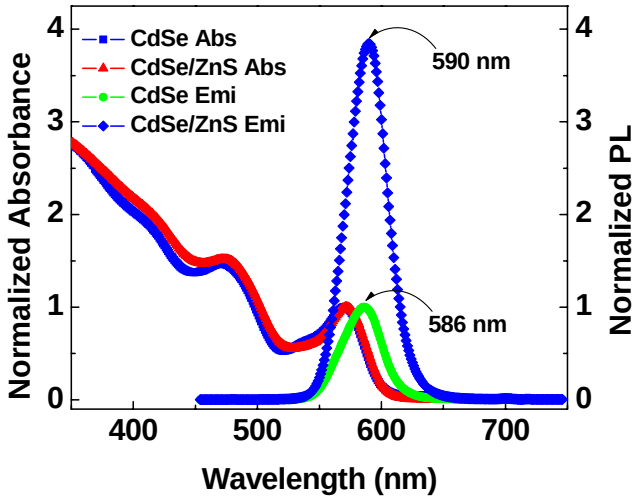

Figure 2.1.4 Typical absorption and photoluminescence (PL) spectra of sample CdSe before and after overcoating with ZnS. The spectra were normalized against the absorbance at the first absorption peak for UV-Vis spectra and the CdSe emission for PL spectra, respectively.

Figure 2.1.4 shows the absorption and PL emission spectra comparison before and after overcoating with 1-2 monolayer (0.31-0.62 nm thickness) of ZnS of one example of a 4.5 nm CdSe NC. A small red shift of the first absorption peak can be seen after overcoating due to partial leakage of the exciton into the ZnS matrix.[35] The photoluminescence spectra of CdSe and CdSe/ZnS indicate the big enhancement of the quantum yield after overcoating. The PL quantum yield increased from ~7.6% to

~29% since the NCs were passivated by ZnS shell. Dabbousi and co-workers carried thorough studies on the effect of ZnS thickness for quantum yield and found out that CdSe overcoated with ~1.3 monolayers (~0.40 nm) of ZnS would exhibit highest quantum efficiency.[35]

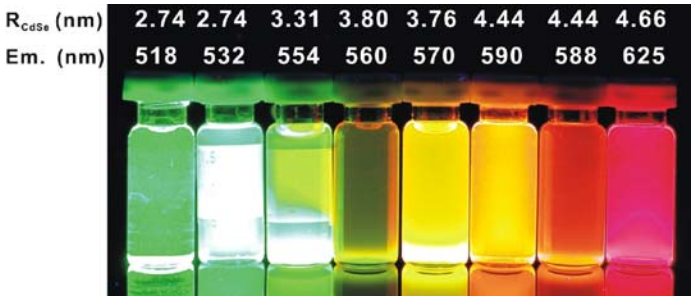

Figure 2.1.5 Color photograph demonstrating the size-tunable fluorescence properties and wide spectral range of the eight QD dispersions (CdSe or CdSe/ZnS) plotted versus CdSe core size and emission maximum. The samples were excited using a 365 nm UV light.

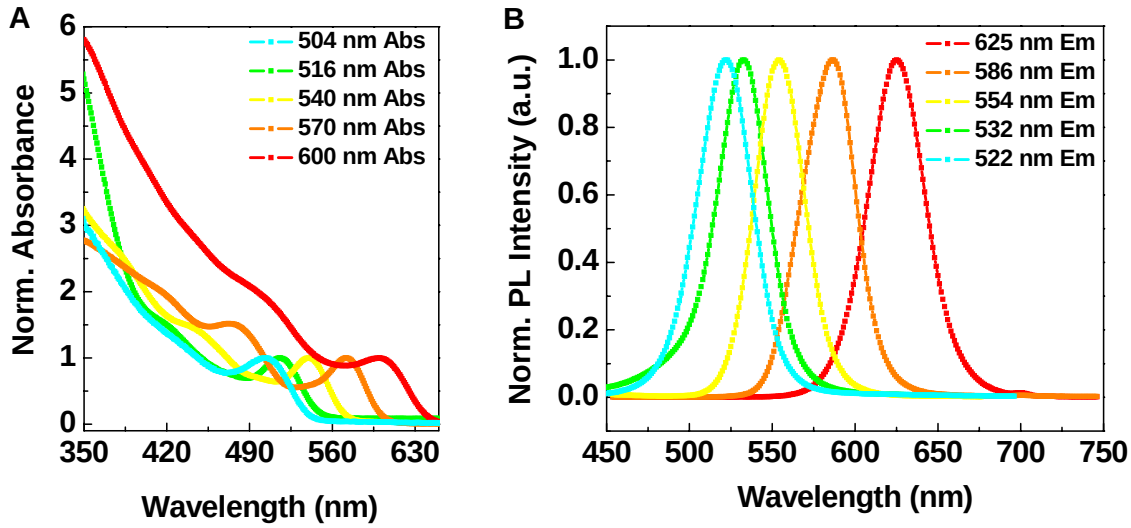

Figure 2.1.6 Absorption (A) and photoluminescence emission (B) spectra of five different CdSe/ZnS QD dispersions. The samples were dispersed in chloroform solutions and excited by 350 nm light.

Figure 2.1.5 displays the wide spectral range of luminescence CdSe (CdSe/ZnS) NCs. The color photograph demonstrates eight different samples of CdSe or ZnS overcoated CdSe QDs dispersed in chloroform solutions. The samples were all irradiated with a 365 nm ultraviolet light from a UV source. As the size of CdSe core increases (from 2.74 to 4.66 nm), the color of luminescence changes from green, yellow, orange to red. Figure 2.1.6 shows the absorption emission spectra of the five different CdSe/ZnS samples all of which were applied in the later parts of this work (chapters 2.2, 2.3 and 2.4).

The Stoke shifts of the fluorescence spectra of these samples were in the range of 15-25 nm and the quantum yield were ranging between ~0.2 and ~0.7, both of which were similar with those reported in literature.[35, 39, 129] Some of the optical properties of five different QDs samples are listed in Table 2.1.1.

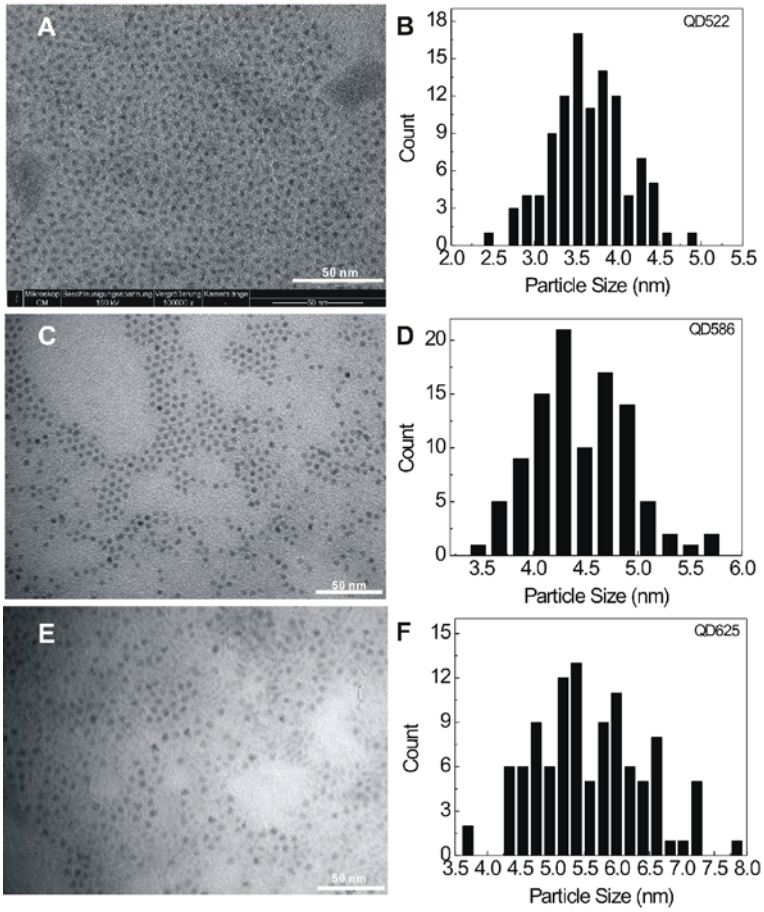

Figure 2.1.7 Transmission electron micrograph and size histogram of one 522 nm (A, B), 586 nm (C, D), 625 nm-emitting (E, F) CdSe/ZnS samples. The magnification for the TEM images are ~4.4×10^5 times (A) and ~3.4×10^5 times (C, E). The sizes of the 522 nm, 586 nm and 625 nm-emitting QDs are 3.7±0.5, 4.5±0.5, 5.6±0.8 nm, respectively according to the histograms.

Transmission electron microscopy was used for imaging of individual crystallite and the development of a statistical description of the size and shape of the particles in a sample. Figure 2.1.7A shows the image at ~4.4×10^5 times magnification with moderate crystallite coverage allows careful size measurements of ~100 individual NCs on a single image and shows that the particles were almost monodisperse. The CdSe/ZnS NCs were found to possess structures with close to spherical shapes. Figure 2.1.7B shows a histogram of size distribution of the same sample and this figure demonstrates

the average size of ~3.7±0.5 nm for the 522 nm-emitting CdSe/ZnS. The sizes of the 586 nm and 625 nm-emitting CdSe/ZnS NCs were also estimated from Figure 2.1.7 C and E, around 4.5±0.5 nm and 5.6±0.8 nm. The NCs are all dot shape like particles with well size distribution.

Table 2.1.1 Resume of the optical properties of five different CdSe/ZnS QDs. The quantum yield data were obtained by using rhodamine 6G as a standard in ethanol. The core size of CdSe was estimated by the first absorption peak.[30]

QDs	Abs/Emi Max (nm)	Stoke shift (nm)	FWHM (nm)	Quantum Yield	Core size (nm)
QD522	504/522	18	39	0.56	2.71
QD532	516/532	16	36	0.71	2.74
QD554	539/554	15	35	0.34	3.31
QD586	570/586	16	38	0.29	4.44
QD625	600/625	25	40	0.20	4.66

2.2 Water-Solubilization and Functionalization of QDs CdSe/ZnS

As discussed previously, there are various techniques for the surface modification of QDs in order to render them water-soluble and functional and target them to specific biomolecular entities.[13, 14, 18, 52, 53] Two general strategies were used in this thesis. On one hand, surface-exchange of hydrophobic surfactant molecules against bifunctional linker molecules such as thoil-containing ligands dihydrolipoic acid was used.[56-58] On the other hand, phase-transfer strategies using amphiphilic molecules that act as detergents solubilizing the QD coated with hydrophobic groups were applied. Phospholipids were chosen as the surfactant to form micelle-stabilized NCs in this thesis.[74-76]

2.2.1 Strategy 1: surface ligand-exchange by dihydrolipoic acid (DHLA)

Mattoussi and co-workers developed a direct method to exchange the surface hydrophobic ligands on the QDs by a dithiolated molecule dihydrolipoic acid (DHLA, Figure 2.2.1) and render these NCs soluble and suitable for biological sensing applications.[56, 62] The resulting DHLA-coated QDs (termed as DHLA-QD) can be stored at 4 °C in borate buffer at pH ~9 for the future use. These negative charged DHLA-QDs are stable and have useful luminescence emission only in aqueous solution at pH ~7 or above. Acidic solutions will induce precipitation of the NCs along with a photoluminescence loss

due to loss of surface charge upon cap protonation or loss of ZnS cap affinity. To produce robust and higher PL QY DHLA-QDs, thicker ZnS shells (e.g. 4~6 monolayers) are usually recommended.[56, 63]

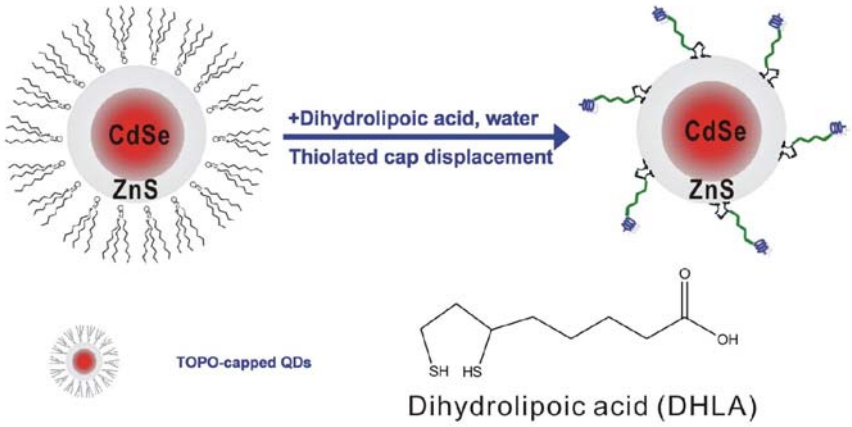

Figure 2.2.1 Schematic representation of the water-solubilization procedure for CdSe/ZnS NCs by ligand-exchange with dihydrolipoic acid (DHLA).

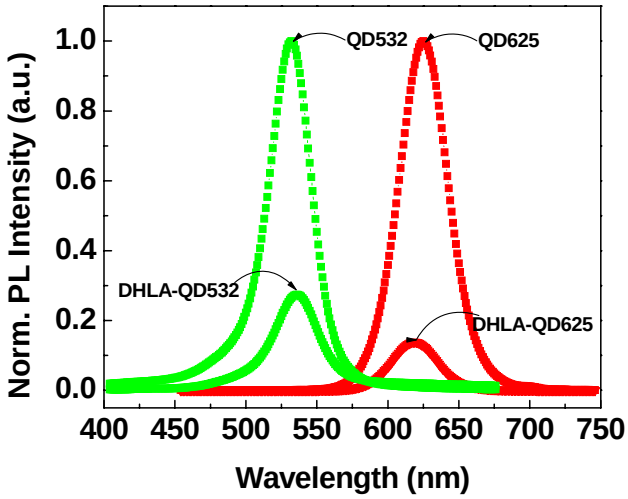

Figure 2.2.2 Normalized PL spectra comparison of two QD samples before and after surface overcoating with dihydrolipoic acid (DHLA).

A reduction of ~50-90% of the PL quantum yield of QDs was typically observed after ligand exchange by DHLA coating. This fluorescence quench was probably due to the decrease in passivation by surface ligands depending on the particular QD sample used. Figure 2.2.2 shows the PL spectra comparison of a 532 nm- and a 625nm-emtting CdSe/ZnS NCs before and after DHLA overcoating. The PL emission spectra indicated that the DHLA-QDs almost maintained the emission wavelength

and ~14-27% of the quantum yield of that of CdSe/ZnS NCs. The negatively charged DHLA-QDs are monodisperse in borate buffer, which was confirmed by atomic force micrographs (AFM). Figure 2.2.3A shows the AFM pictures of the 625 nm-emitting DHLA-QDs which were immobilized on magnesium ion (Mg^{2+}) modified mica slides. The heights of ~8000 particles on the same mica surface were statistically collected and plotted as a histogram as shown in Figure 2.2.3B. The particle size obtained from the statistical study was around 9.9±3.7 nm. This is around 68% bigger than the size detected by TEM, possibly due to the soft organic ligand molecules on QD surface which were also detected by AFM height measurements.

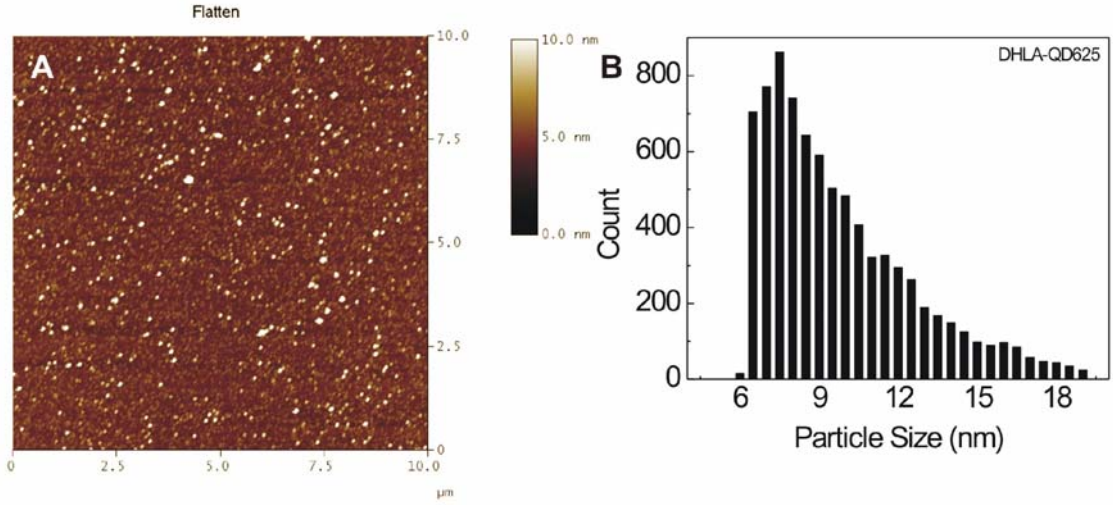

Figure 2.2.3 (A) AFM image of DHLA-QD625 on Mg^{2+} modified mica (10 μm×10 μm, z-scale=5 nm). The DHLA-QDs were dispersed in borate buffer (pH=9.0) at the concentration of 10 μM. (B) height histogram of ~8000 particles on the same surface of that of A. The particle size of DHLA-QD625 obtained from the particle heights is around 9.9±3.7 nm.

The DHLA-QD allows an electrostatic adsorption of biomolecules possessing either a natural positive surface charge (e.g. avidin) or engineered positively charged domains (e.g. a basic leucine zipper or polyhistidine tag), which provides a direct and simple way for the conjugation of biomolecules (e.g. protein or DNA) on the surface of DHLA-QD.[62, 104] In contrast to the commercial QDs, which are often of sizes around 15-30 nm, the reduced particle sizes (~5-10 nm) of DHLA-QDs due to the thin DHLA layer are also a great advantage for the biological applications, especially for the sensing study in which QDs are used as energy donors. Conjugation of DHLA-QDs to maltose binding protein (MBP), the immunoglobulin-G-binding β2 domain of streptococcal protein G (PG) and avidin or polyhistidine tagged peptide have been achieved for some applications in biological sensing or imaging.[56, 58, 63, 90, 91,

[104, 106, 107, 124] However, there are also some disadvantages of this capping strategy. For example, the subsequent bioconjugation requires the use of proteins that have been engineered to express a leucine zipper domain or a polyhistidine tag. This limits the applications of DHLA-QDs. The conventional covalent cross-linking approach based on EDC (1-ethyl-3-(3-dimethylaminopropyl) carbodiimide hydrochloride) condensation was relatively unsuccessful because the dihydrolipoic acid tended to be protonated and the DHLA-QDs extensively aggregated in the acidic coupling buffer.[56] Furthermore, the stability, particularly *in vivo* stability of DHLA-QDs is poor, which also limits their applications in cellular imaging.[63] Finally, the relatively low quantum yield of DHLA-QDs is also a significant drawback.

2.2.2 Strategy 2: solubilization and functionalization with phospholipid micelles

2.2.2.1 Encapsulated in poly (ethylene glycol) (PEG) phospholipid micelles

Poly (ethylene glycol) (PEG) derivatized phospholipids (termed as PEG-PLs) are extensively used for the steric stabilization of liposomes or vesicles.[132] The incorporation of an appropriate amount of PEG lipid into the membrane will greatly increase the colloidal stability of the liposomes. However, in dilute aqueous solution these PEG-PLs tend to form spherical micelles if the critical micelle concentration for each compound is reached. The central holes of these PEG-PLs micelles are of nanometer dimensions, which provide the possibility for encapsulating nanoparticles or drug inside the micelles for further applications.[74, 133-136] Dubertret and co-workers presented a simple strategy to encapsulate single QDs in PEG-PL micelles.[74, 76] Figure 2.2.4 shows an exemplary procedure of encapsulating QDs with 90% of PEG2000-PLs and 10% of functionalized PEG2000-PLs (e.g. biotinylated, amino, carboxyl or maleimidyl functionalized PLs). Due to hydrophobic interaction between the TOPO/TOP ligands and the hydrophobic headgroups of PEG-PLs, the NCs are stabilized inside the empty holes of the micelles. PEG exhibits a very low degree of nonspecific interactions with other biomolecules or polymers in an aqueous environment, which attracts many interests to use it for biotechnical and biomedical applications. In addition, PEG is non-toxic and does not damage active proteins or cells although it might interact with cell membranes. The PEG-PLs used for the encapsulation are commercially available with PEG size ranging from 350 to 5000 Da. In this thesis, the PEG2000-terminated (2000 Da) phospholipids were used for encapsulating QDs.

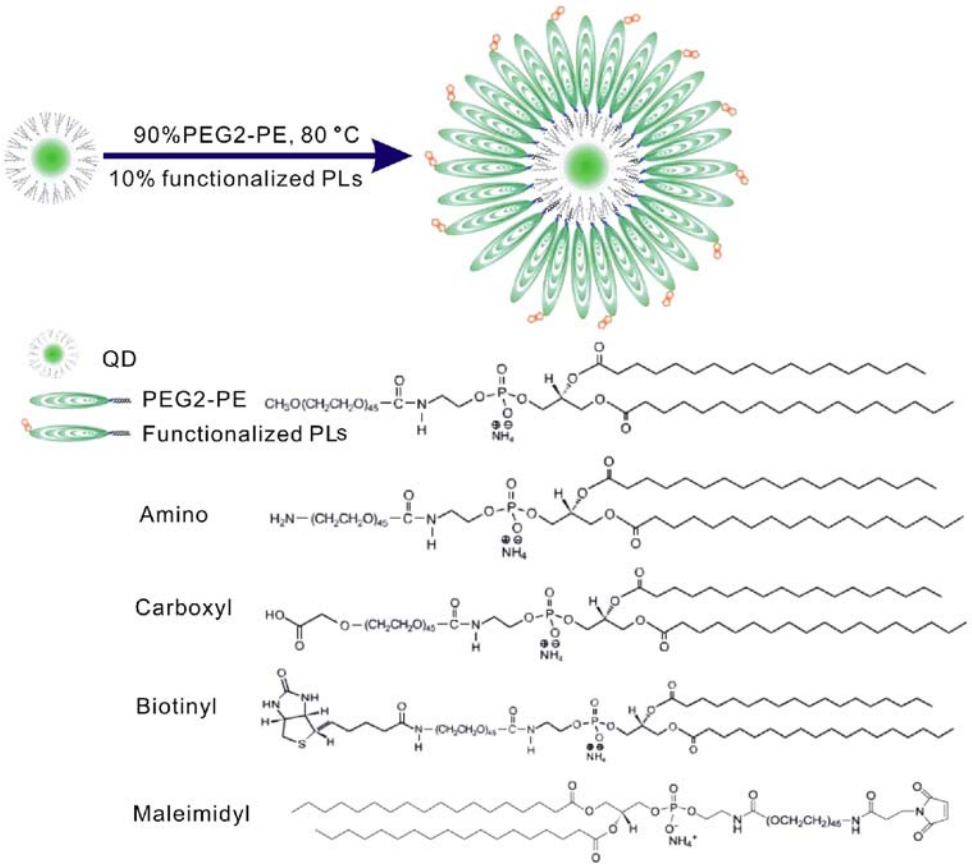

Figure 2.2.4 Schematic representation of the procedure of QD micelle encapsulation and functionalization with PEG2000-terminated PLs and functionalized PLs. The structures of some of the commercially available functionalized PLs (amino, carboxyl, biotinylated and maleimidyl) were shown.

Dubertret et al suggested a two-step protocol to encapsulate QDs with PEG2000-PLs.[74, 76] Firstly a PEG2000-PLs and QDs film was prepared by evaporating the organic solvent from the mixture. The PEG2000-PLs-QDs film was subsequently rehydrated and dispersed in water by smooth stirring, yielding a clear PEG2000-PLs encapsulated QDs (termed as PEG2000-QDs) solution. However, this protocol did not work well in the preparation of this thesis. Instead of the described protocol, a one-step protocol was used to encapsulate QDs in PEG2000-PLs (Figure 2.2.4).[137] Briefly, the mixture of QDs, *m*PEG(2000) phosphatidylethanolamine (*m*PEG2000-PE) in the solvent of chloroform and distilled water were heated slowly in boiling water bath and the chloroform was evaporated by gentle rotary-evaporation. The QDs transferred from the organic phase into the aqueous solution once the micelles formed. The remaining chloroform can be removed under vacuum and the resulting clear micelle-QDs solution can then be purified either by an ultracentrifugation or by size exclusion chromatography (SEC)

to remove the empty micelles and free phospholipids. By varying the PEG-PLs headgroups in the lipid mixture, it is possible to introduce a variety of physical (switchable electrical charges, structures, entropic shielding) and chemical (functional or reactive groups, biological recognition units) properties (Figure 2.2.4). Addition of functionalized (e.g. biotinylated, amino, carboxyl, maleimidyl, etc.) PEG2000-PLs to the PEG2000-PLs allowed to preparing functionalized QDs, which provided the possibility for the further conjugation with biomolecules. This one-step protocol is a more convenient and efficient route to solubilize and functionalize QDs compared with the one described previously.[74, 76] One of the major challenges of surface-modified QDs suitable for cell labeling and single particle tracking is nonspecific binding, which is partly attributed to electrostatic attraction of the biological surface with charged QD ligand coatings.[138] The overall charge of the phospholipid micelle can be tuned precisely for a given pH by adding to the PEG-PLs amino-PEG-PLs or COOH-PEG-PLs to promote electrostatic interactions with oppositely charged entities.[76]

The optical properties of PEG2000-QDs in water were compared to those of the original NCs in chloroform. Photoluminescence quantum yields of PEG2000-QDs remain 40-85% of those of QDs in organic solvent in this work. Transferring the QDs from organic solvent to aqueous phase by coating with the micelles did not lead to significant changes in the absorption and emission spectra shapes. Figure 2.2.5 indicates that PEG-PLs encapsulated QDs almost keep the emission maxima position (~2 nm red shift) and ~80-85% of the luminescence depending on different samples. The final quantum yields of PEG2000-QDs samples were measured to be ~20 to 60% by comparing with Rhodamine 6G.

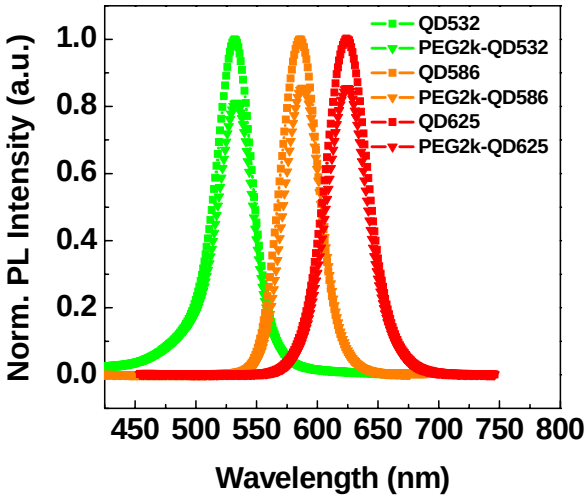

Figure 2.2.5 Photoluminescence emission spectra of 532 nm, 586 nm and 625 nm-emitting QDs CdSe/ZnS before and after encapsulation in PEG2000-PLs.

The size of the QDs once they are rendered hydrophilic is a very important parameter, particularly with regard to QD diffusion in tissue or cellular environment or FRET-based sensing study. The size of the PEG2000-QDs depends on the size of the QDs synthesized and the size of PEG chosen. Compared with DHLA-QDs, QDs encapsulated with PEG2000-PLs are reported to be slightly larger in the hydrodynamic diameter (HD) measured by dynamic light scattering (DLS), ranging from 14-24 nm.[76] For example, the HD of a PEG2000-QD586 sample, which was prepared in this work with a CdSe/ZnS core size of ~4.5 nm is ~18.5 nm, in contrast with ~8.3 nm for DHLA-QD586.

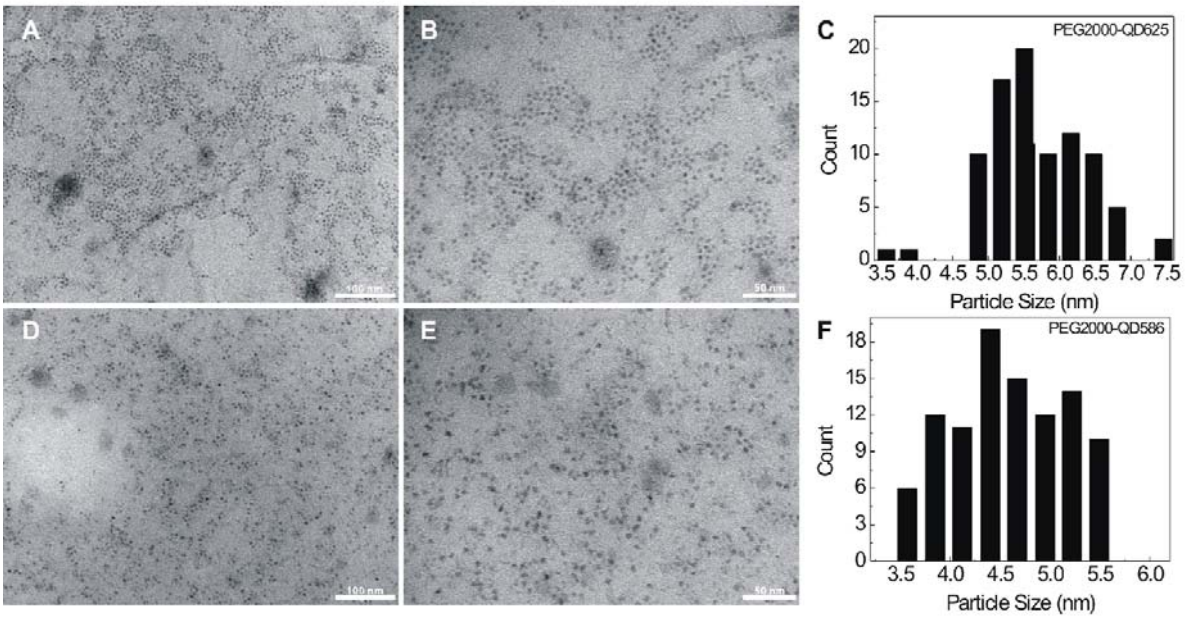

Figure 2.2.6 TEM images of PEG2000-PLs encapsulated QDs with emission at 586 nm (A, B) and 625 nm (D, E) and size histogram for PEG2000-QD586 (C) and PEG2000-QD625 (F). Only the QDs inside the PEG2000-PLs micelle core are seen in the images. The sizes of the 586 nm and 635 nm-emitting PEG2000-QDs are 4.6±0.6 nm and ~5.6±0.7 nm, respectively, which are similar with those before PLs encapsulation.

Transmission electron microscope images of PEG2000-QDs give the information of the core size and dispersion (Figure 2.2.6). The QD-micelles were dried on a carbon-formvar-coated 200-mesh cooper grid. Only the QDs inside the micelle core were visible. The particles appear evenly spread on the grid surface. It is reasonable that the particle sizes of each sample are similar with the ones before encapsulation. (~4.6±0.6 nm for 586 nm and ~5.6±0.7 nm for 625 nm-emitting QDs) The QD-micelles appeared spherical and fairly monodisperse. As also observed from the images, majority of the QDs are isolated, suggesting that most of the micelles contain a single NC. The encapsulation of the QD inside

the micelle does not perturb the geometry or size, because the core of this phospholipid micelle is of the similar size of the QDs we used according to previous study.[74, 132] To investigate the sizes and shapes of the phospholipid micelles, AFM is a better technique than TEM because the organic ligands are invisible under TEM and can be possibly detected by AFM. However, in this thesis, the PEG2000-QDs were failed to immobilize on the mica surface due to the small charges of these micelles.

2.2.2.2 Solubilization and functionalization with non-PEG-phospholipids

Geissbuehler and co-workers presented a general and versatile procedure to make QDs water-soluble and functionalized by a non-PEG phospholipids (termed as PLs).[75] The biggest advantage of the non-PEG-phospholipids coated QDs (termed as PLs-QDs) is a reduced size compared with PEG2000-QDs, which makes them more efficient for the observation of FRET interactions. A PLs-QD is composed of the core, CdSe/ZnS, which is also surrounded by a 1 nm thick TOPO/TOP layer and a lipid shell. (Figure 2.2.7) The typical diameter of a PLs-QD is around 9-12 nm. Following this strategy, PLs-QDs were prepared using two commercially available phospholipids, 1-palmitoyl-2-oleyl-sn-glycerophosphatidylcholine (POPC) and 1-palmitoyl-2-oleyl-sn-glycerophosphatidylglycerol (POPG).

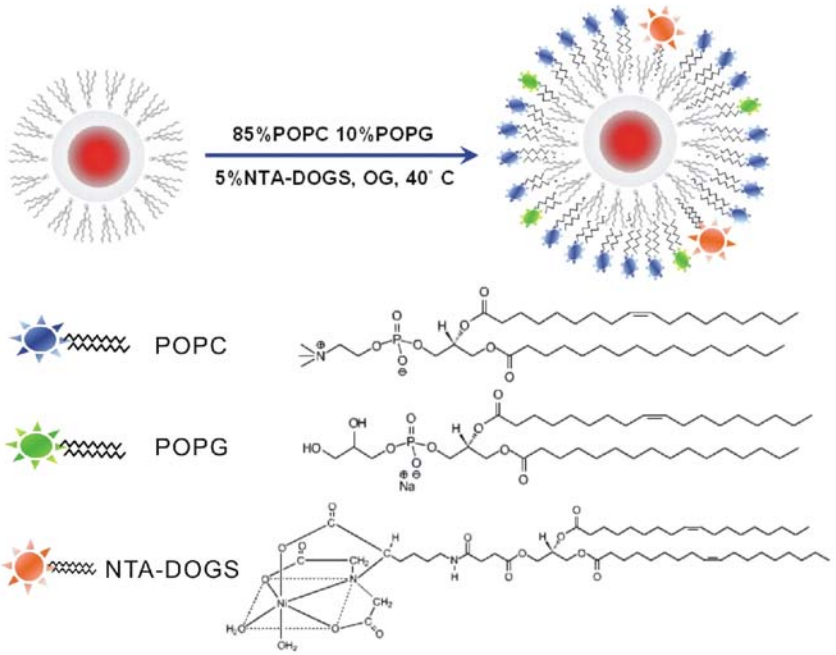

Figure 2.2.7 Schematics of the preparation procedure of non-PEG-PLs (POPC and POPG) coated QDs (PLs-QDs) and functionalization with Ni^{2+}-nitrilotriacetic acid (Ni-NTA) groups.

Figure 2.2.7 illustrates the procedure to prepare the Ni-NTA functionalized PLs-QDs. Using a simple mixing and evaporation route, the hydrophobic QDs were solubilized based on the self-assembly of single lipid monolayers on the particles. A surfactant β-octylglucopyranoside (OG) was added to the mixture to increase the phase transfer between the chloroform and water. The QDs can be simultaneously decorated with diverse range of multiple functionalities by doping functionalized phospholipids with amino, carboxylic acid, Ni-NTA or other technical groups. These phospholipids are commercially available.

The resulting PLs-QDs can be washed and purified by a cut-off concentrator or by dialysis to remove the detergent. Similar to PEG2000-QDs, solubilizing QDs with non-PEG-PLs yielded little changes in the absorption and emission spectra of shapes or positions but a modification of the quantum yields. Figure 2.2.8 shows that photoluminescence emission comparison of three sizes of QDs before and after coating with phospholipids. The quantum yields of PLs-QDs remained from ~22 to 60% varying from sample to sample. It has been reported that the surface of the QD is critical for the photoluminescence characteristic of NCs. The type, amount and folding state of the surface ligands, the position and structure of the ligand layer and the lipid layer influence on TOPO/TOP molecules, are possible reasons for the decrease of the quantum yields after coating with lipids.[75, 139, 140] However, the mechanism of the molecular basis of this effect is still not clear. As a consequence, it is difficult to predict the quantum yields of different PLs-QDs samples. The quantum yields of PLs-QDs depend on the CdSe/ZnS NCs and as well as the lipid layers (Figure 2.2.8).

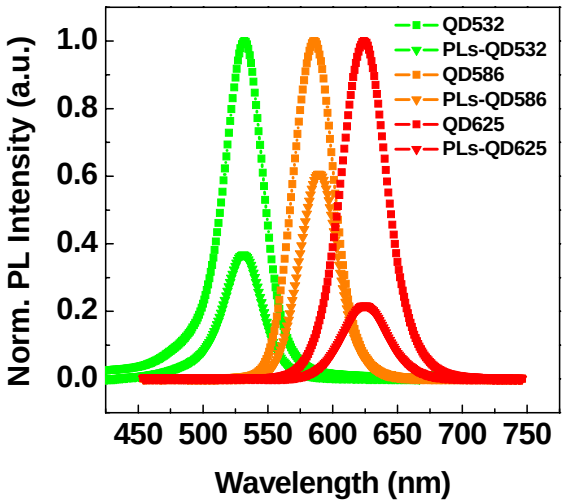

Figure 2.2.8 Photoluminescence emission spectra of 532 nm, 586 nm and 625 nm-emitting QDs CdSe/ZnS before and after coating with non-PEG-PLs POPC and POPG.

The particle shapes and sizes of the lipid-coated QDs are similar with those of TOPO/TOP-coated QDs, which are clearly observed by transmission electron microscope (Figure 2.2.9). As also discussed earlier in chapter 2.2.2.1, the organic lipid layers were not dense enough to be observed by TEM and only the QD cores were detected. For further observation of the lipid layers, cryogenic-TEM or AFM detection could be better choices,[75] which were not carried out in this thesis. Nevertheless, the TEM images in Figure 2.2.7 suggest the monodispersity and well-structure of PLs-QDs with average size of ~4.6±0.5 and 5.6±0.6 nm for 586 nm and 625 nm-emitting QDs, respectively.

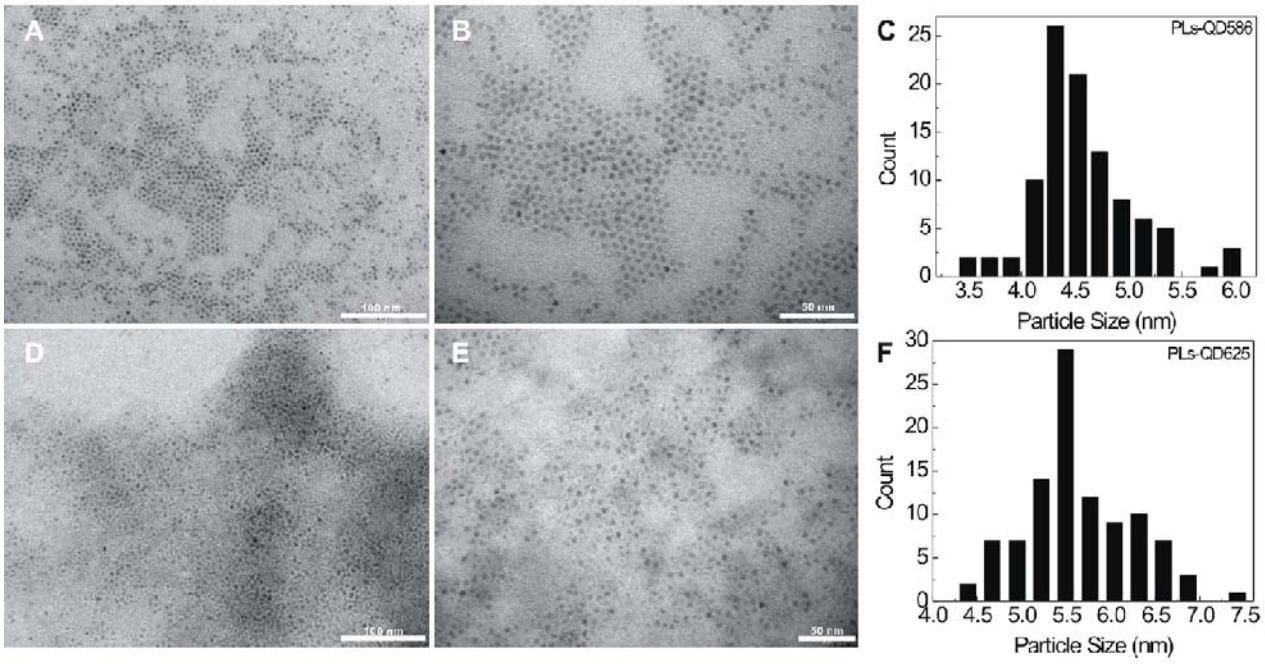

Figure 2.2.9 TEM images of PLs-QDs with emission at 586 nm (A, B) and 625 nm (E, E) and size histogram of PLs-QD586 (C) and PLs-QD625 (F). Only the QDs inside the phospholipid vesicles are seen in the images. The average size of 586 nm and 625 nm-emitting PLs-QDs are ~4.6±0.5 and 5.6±0.6 nm, respectively, which are similar to those before lipid coating.

2.2.3 Summary

Two different methods to solubilize and functionalize the TOPO/TOP-coated QDs were introduced in this chapter: (i) ligand-exchange strategy using dithiolated molecule dihydrolipoic acid (DHLA); (ii) a simple one-step procedure to coat QDs with either PEG-containing or non-PEG phospholipid micelles. For DHLA-QDs, surface negative charge provides the possibility to attach proteins, peptides or oligonucleotides with positive charge domains or motifs. For lipid-coated QDs, a huge choice of

functionalities is available by choosing different functionalized lipids. Table 2.2.1 provides a summary and comparison of the characteristics of DHLA-QDs, PEG2000-QDs and PLs-QDs.

Table 2.2.1 Characteristics comparison of TOPO-, DHLA-, PEG2000-PLs-, non-PEG-PLs-coated QDs (532, 586 and 625 nm-emitting)

QDs	Preparation	Size (nm) *	QY (%)	Photostability[5] (%)			Surface charge	Functionalities	applications
				W[6]	P[7]	C[8]			
TOPO-QD	Hot-injection (~10 hrs)	3.7 [1]	71 [4]	/	/	/	/	/	/
		4.5 [1]	29						
		5.6 [1]	20						
DHLA-QD	Ligand-exchange (~5 hrs)	/	10	91	86	76	Negative in basic environments	Electrostatic binding	FRET donor
		8.3 [2]	7.9						
		9.9 [3]	2.8						
PEG2000-QD	Phase transfer (~90°C, 10 mins)	12 [2]	57	107	100	113	Can be adjusted by doping with NH_2-, COOH-lipids	-NH_2, -maleimidyl -COOH, -biotin [9]	Cellular imaging
		18 [2]	20						
		24 [2]	17						
PLs-QD	Phase transfer (~40°C, 20 mins)	9.9 [2]	18	41	68	72	Can be adjusted by doping with NH_2-, COOH-lipids	Ni^{2+}-NTA- [10]	FRET donor
		12 [2]	17						
		/	4.4						

* color differs from green to orange and red for 532 nm-, 586 nm- and 625 nm-emitting QDs, respectively;

[1] determined by TEM; [2] determined by DLS, hydrodynamic diameters including the organic DHLA or lipid layers;

[3] determined by AFM, hydrodynamic diameters including the organic DHLA layers; [4] measured by using rhodamine 6g as a quantum yield standard; [5] photostability evaluated by the fluorescence remaining of the DHLA-, PEG2000- and PLs-QD586 in three different media, ddH_2O, PBS and A431 cell lysate after 8 hrs, also plotted in Figure 2.4.2; [6] distilled water; [7] PBS buffer; [8] A431 cell lysate; [9] other possible functionalities including -SH, , -OH, -fluorescein, etc. by doping commercial functionalized PEG2000-PLs; [10] other possible functionalities including -SH, , -OH, -NH_2, -maleimidyl -COOH, -biotin, etc.

2.3 Self-Assembled Donor Complexes Comprising DHLA-QD and Fluorescent Proteins for Long-Range FRET

Luminescent semiconductor QDs have unique optical and spectroscopic properties that offer a compelling alternative to organic dyes or fluorescent proteins in FRET-based biosensing.[17, 61] QDs are

excellent energy donors with broad absorption wavelength range and high molar extinction coefficients (normally 10-100 times of that of organic dyes). Furthermore, the tunable and narrow symmetric PL emission spectra in the range from UV to near-IR with high quantum yields, exceptional anti-photobleaching properties and large Stokes shifts all are valuable factors for a donor system. Among these, three properties are particularly appealing for FRET-based biosensing investigations: (i) tunable PL emission which can be obtained by varying the size of the QD, which allows better control of the spectral overlap with donors;[90] (ii) serving as a nanoscaffold, multiple acceptor molecules can be immobilized on one QD to achieve higher energy transfer efficient and more robust donor/acceptor FRET system;[56, 104] (iii) different QDs can be excited at a single excitation wavelength far away from their respective emissions, which provides the possibility for multiplex FRET-based assays.[108]

Energy transfer between QDs and fluorescent proteins has been mentioned in previous reports.[75, 141] However, a comprehensive study (both steady-state and time-resolved state) of the energy transfer efficiency, donor/acceptor (D/A) separation distances and detailed interaction profile are still missing or ambiguous in these papers since the QD/fluorescent protein FRET pair design is more intricate than simple dye/dye or QD/dye FRET pairs. In this work, a self-assembled donor system comprising QD and multiple fluorescent proteins was fabricated and investigated in detail focusing on the interaction between inorganic nanocrystal and the acceptor proteins, the average D/A separation distance and the energy transfer profile, from both steady-state and time-resolved PL measurements. Two different proteins, red fluorescent protein eqFP611 and enhanced yellow fluorescent protein (EYFP) were used as acceptors to fabricate the two chromophore-FRET (2Ch-FRET) systems. Based on this new donor system, a three chromophore-FRET (3Ch-FRET) system was assembled and spectroscopically characterized (Figure 2.3.7). The system comprises three different types of fluorophores, that are luminescent QDs, EYFP and short single-stranded DNA (ssDNA) oligonucleotides tagged with the organic dye Atto647, all of which are common fluorescent tags in bio-labeling and bio-sensing. By taking advantage of the QD/EYFP 2Ch-FRET system, which combines the advantages of QDs (large absorption cross section, tunable size and spectral properties) with those of fluorescent proteins (high quantum yields) it was able to redirect the energy transfer from the QD directly to the Atto647 dye by using the EYFP/Atto647 FRET channel. As a consequence of using QD/EYFP instead of EYFP or QD as the donor, long-distance FRET occurred within donor-acceptor distances of up to 13 nm and with an efficiency of 5%, as compared to 0.3% obtained for using QD only.[142]

2.3.1 Two-chromophore FRET system of QDs and fluorescent proteins

2.3.1.1 Energy transfer between QDs and eqFP611

Before elucidating the FRET system with EYFP and QD, whose emission spectra overlap strongly, it is easier to deal with the eqFP611/QD system, in which green-emitting QD536 was used as energy donor for the red-emitting eqFP611. The red fluorescent protein (FP) eqFP611 shows favorable properties for applications as a molecular marker. It is a tetramer under physiological conditions. The interactions among the monomers are comparatively weak, as inferred from its dissociation into monomers in the presence of sodium dodecyl sulfate (SDS) or at high dilution.[143, 144] Every monomer inside one eqFP611 is quite similar to one GFP-like mutant. In this project, the His_6-modified eqFP611 was immobilized on a DHLA-QD via the Zn-hexahistidine coordination or on a Ni-NTA functionalized lipid-coated QD via Ni-NTA-hexahistidine coordination. As illustrated in Figure 2.3.1A, multiple eqFP611 can be attached on one DHLA-QD surface due to the electrostatic interaction. Since every tetramer eqFP611 has four monomers, all of which possess a His_6 and are ready to attach to the QD surface, this brings additional complexity to analyze the interaction between the tetramer and DHLA-QD. Every monomer has its own functionalized group and is capable to access to the QD surface via Zn-hexahistidine interaction. In addition, every monomer has it own chromophore center and can serves as an energy acceptor for QD. Therefore, in this thesis, an approximative model was applied to consider the average interaction between the eqFP611 monomers and QD. Although the four monomers inside a tetramer are not completely equivalent from the binding position, orientation or D/A separation distances, this model assumes an equivalent GFP-like monomer when quantitatively investigating FRET between QD and eqFP611. For example, the parameters such as molar extinction coefficient, concentration and D/A separation distance are averaged for the four monomers (Table 2.3.1).

Table 2.3.1 size and spectroscopic properties of eqFP611 and EYFP

FPs	**Mw (kD)**	**Absorption λ_{max} [nm]**	**Emission λ_{max} [nm]**	**$\varepsilon_{abs\text{-}max}$ [$M^{-1}cm^{-1}$]**	**QY [%]**	**Size (monomer)**
eqFP611	26	559	611	78000	45	~2.4×4.2
EYFP	27	514	527	84000	62	~2.4×4.2

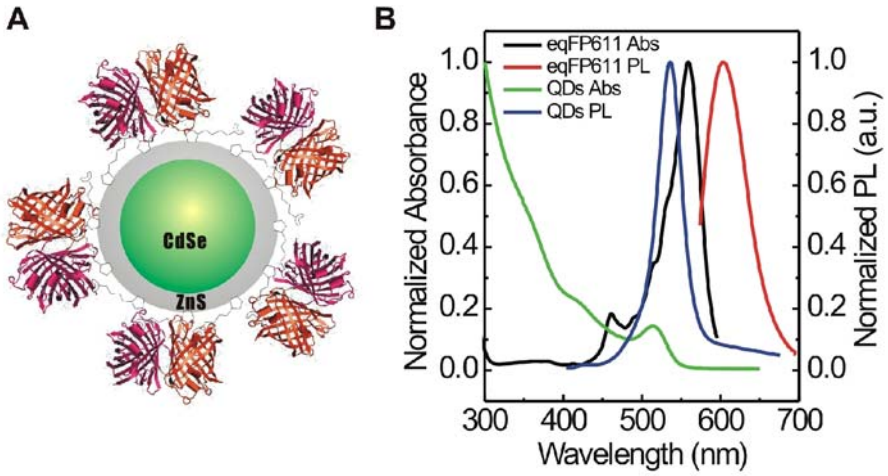

Figure 2.3.1 Schematic representation and spectral properties of a DHLA-QD/eqFP611 donor/acceptor system. (A) multiple eqFP611 were adsorbed to DHLA-coated QD to form a QD/FPs conjugate; (B) spectroscopic characterization of the 536 nm-emitting DHLA-QDs absorption (green) and emission (blue) and eqFP611 absorption (black) and emission (red).

Figure 2.3.1B shows the DHLA-QD536 emission and the eqFP611 absorption and emission spectra overlap and the integrated overlap was calculated to be ~3.2×10^{-13} cm^3M^{-1} and listed in Table 2.3.2. To elucidate the energy transfer between DHLA-QD and eqFP611 monomers, a titration experiment was carried out by increasing the addition ratio of eqFP611/QD and the results are plotted in Figure 2.3.2. The system was excited at the wavelength of 400 nm, where the eqFP611 absorption is minimal and QD absorbs strongly. Note that the concentration of eqFP611 used here refers to the one for monomers (i.e. four times of that of the eqFP611 tetramers). The results show that with ~20-25 eqFP611 monomers, coverage on one QD will reach the space saturation. This number can also be theoretically estimated by a previously described model in which the QD was regarded as a spherical center and the protein molecules are assumed to be close-packed spheres around the central QD.[56]

$$N_{eqFP611} = 0.65\left(\frac{\left(R_2^3 - R_1^3\right)}{R_p^3}\right) \qquad 2.1$$

As depicted in equation 2.1, R_1 is the QD radius and $R_2 \sim R_1 + 2R_p$ is the radius of QD plus bound eqFP611 molecules. The radius of a 536 nm-emitting QD is ~2.0-2.3 nm. eqFP611 monomer, a mutant of GFP has a β-barrel structure with a diameter of ~2.3-3.0 nm and a length of ~4.0-4.2 nm, similar to that of GFP.[145] Using values of R_p=~1.8 nm (equiv radius of a cylinder), R_1=~2.1 nm for CdSe/ZnS QD for equation 2.1 leads to a surface coverage number of ~20 per QD, which is slightly smaller than the

data obtained from titration experiments. The ideal model assumed that all the four monomers were equally attached to the QD surface, which is unlikely in the actual state. Some of the monomers may not directly involve in the surface coverage of QD but still serve as acceptors because these monomers are part of the bound tetramers and did not directly contact QD but the distances are close enough for an efficient FRET. These monomers actually have been counted in the titration number, which was slightly larger than the calculated one from space coverage. One may speculate that, if there is enough space, most of the monomers will attach to QD via Zn-hexahistidine coordination due to the strong electrostatic interaction. It was also reported that the surface-immobilized eqFP611 molecules were monomeric,[143, 144] which on the other hand confirm this model.

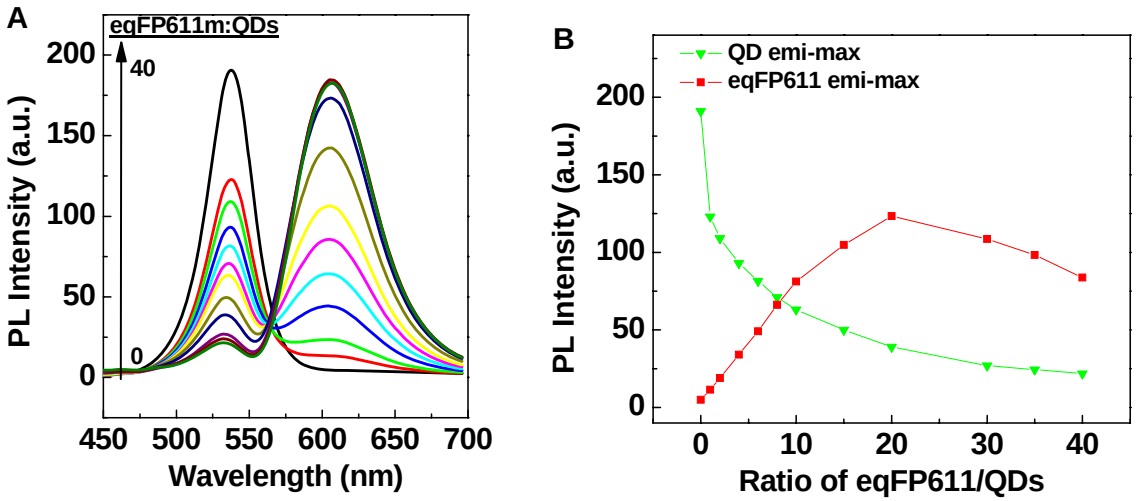

Figure 2.3.2 PL evolution of the DHLA-QD/eqFP611 FRET system. (A) Titration of QDs with increasing molar ratios of eqFP611 (the concentration refers to the one for monomer) measured at an excitation wavelength of 400 nm; (B) QD PL (green triangle) and eqFP611 PL (red square) as a function of the ratio eqFP611 (monomer)/QD. Note that the data for eqFP611 PL in (B) were corrected for the PL background from direct excitation.

The FRET efficiency of ~0.80 was estimated (Figure 2.3.2A) from the PL quenching of DHLA-QD using equation 1.4 in chapter 1.3.1. This FRET efficiency results in an average D/A separation distance of ~5.6 nm between the QD center and the eqFP611 monomer chromophore, taking into account a Förster radius of R_0=~4.3 nm for a QD/eqFP611 FRET pair and $N_{eqFP611}$=~20 using equation 1.1 in chapter 1.3.1. The Förster radius of R_0 and overlap integral J were estimated based on equation 1.2 and 1.3 with the aid of the software *photochemCAD*.[146] All the FRET parameters were calculated and listed in Table 2.3.2. The average D/A distance of ~5.6 nm is larger than the theoretical value estimated from geometric considerations that take into account the size of the QD, the size of eqFP611 monomer and

the average interaction between the two chromophores. The proteins are attached to the surface of QD by means of Zn-hexahistidine interaction and the distance between the centers of QD and eqFP611 can be estimated by adding the radius of the QD (~2.1 nm), the half diagonal length of one eqFP611 monomeric cylinder (~2.4 nm) and the length of hexahistidine tail (~0.7 nm when all polyhistidine residues are coordinated to the QD surface[106]). This yields a sum of r=~5.2 nm, which is ~0.4 nm less than the one from the PL titration data. The D/A separation distances from geometric relation require tight packing of the proteins, which is unlikely in the case of eqFP611. This may explain the relatively large D/A separation distance value.

To confirm the energy transfer from QD to the fluorescent proteins, a qualitative time-resolved fluorescence measurement was carried out by investigating the temporal evolution of the QD/eqFP611 conjugate by time-resolved fluorescence spectroscopy (Figure 2.3.3). To this end, samples containing the QD/eqFP611 conjugates were excited with a 50µW pulsed laser at the wavelength of 400 nm. As indicated from Figure 2.3.3, the emission of QD/eqFP611 conjugate showed an increase in intensity at 619-649 nm range and decrease in intensity at 538-649 nm range due to the decrease of QD emission and enhancement of eqFP611 emission. For comparison, the PL decay of two separated samples comprising only of QDs or eqFP611 were measured and found to display a slower decay in QDs case and a faster decay of eqFP611 sample. These qualitative time-resolved measurements are in agreement with the steady-state PL study (Figure 2.3.2).

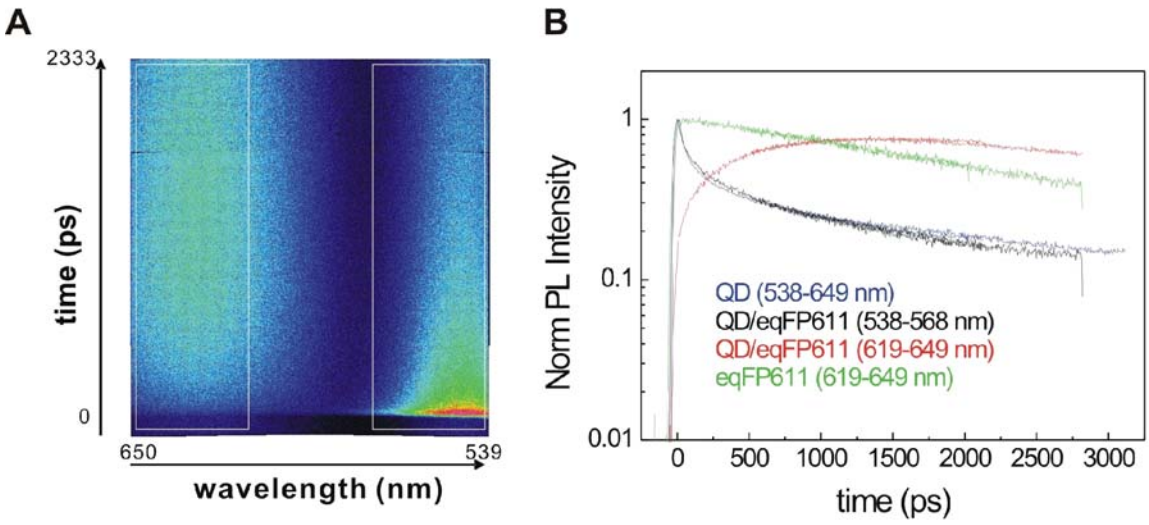

Figure 2.3.3 Temporal evolution of the PL signal of the QD/eqFP611 conjugate. (A) Spectrally and temporally resolved dynamics of the conjugate emission. The region over which the intensity was spectrally integrated to

generate the cut, shown in the right panel, is indicated by the white box. (B) Emission dynamics of the spectrally integrated QD/eqFP611 conjugate (black and red curves), QD alone (blue) and eqFP611 alone (green).

In addition to DHLA-QDs, non-PEG phospholipid coated QDs (PLs-QDs), which were functionalized with Ni-NTA group, were also used as FRET donors for eqFP611. As mentioned earlier, compared with PEG2000-QDs, PLs-QDs have much smaller hydrodynamic size, which makes them possible to use as FRET donors. The advantage of PLs-QDs donors in contrast to DHLA-QDs donors is their better stability in big pH range, which makes them possible for FRET-based *in vitro* or *in vivo* biosensing.[75] Figure 2.3.4 shows the similar titration experiment results which indicate that the energy transfers from a PLs-QD531 to the eqFP611 proteins. The saturation was reached when ~35 eqFP611 monomers were immobilized on one QD (Figure 2.3.4B). This number is larger than that of DHLA-QD system probably due to the larger hydrodynamic diameter of the PLs-QDs as well as a different binding mechanism. The specific binding of the eqFP611 to PLs-QDs was based on Ni-NTA-His_6 coordination but not on electrostatic interaction as in the DHLA-QD/eqFP611 system.[75] A control experiment was carried out by using PLs-QD531 without Ni-NTA functional groups and indicated no eqFP611 PL signal increase, which confirmed Ni-NTA-His_6 binding mechanism. As a consequence, the number of binding proteins depends on the available functional groups on one QD, and of course this number should be equal or smaller than the theoretical packing capability for a ~9.9 nm size PLs-QD. This theoretical upper limit can be estimated based on equation 2.1 with the size of eqFP611 monomer (R_p~2.1 nm) and lipid-QD531 (R_1~5.0 nm, determined by DLS) and gives value of ~45 eqFP611 monomers per QD. However, the binding mechanism of eqFP611 is "one to one" coordination and is different from the electrostatic interaction, where all the His_6-tagged monomers are possibly attached to the DHLA-QD surface as long as there is enough space.

The NTA PLs-QDs were prepared by adding 10% of Ni-NTA functionalized lipids to the mixture of POPC and POPG. This should lead to about 70-100 lipids per QD and 7-10 Ni-NTA lipids per QD according to a previous report.[147] If one assumes that these 10% Ni-NTA groups distribute evenly on the spherical surface, which is likely, the average distance between two Ni-NTA groups is ~6 nm (e.g. a simple model of 8 Ni-NTA groups on a PLs-QD spherical surface is an inscribed cube in a 9.9 nm-diameter sphere, the smallest distance between two vertexes is the length of the cube, ~5.7 nm). This distance does not allow all of the four His_6 tags in one eqFP611 tetramer (equivalent diameter, ~5.2 nm) bind to four Ni-NTA groups. The most possible packing geometry is that one Ni-NTA group binds one

eqFP611 tetramer. Accordingly, 7-10 tetramer eqFP611 bind to one PL-QD, leading to ~28-40 monomers per QD, which is close to the number obtained by titration.

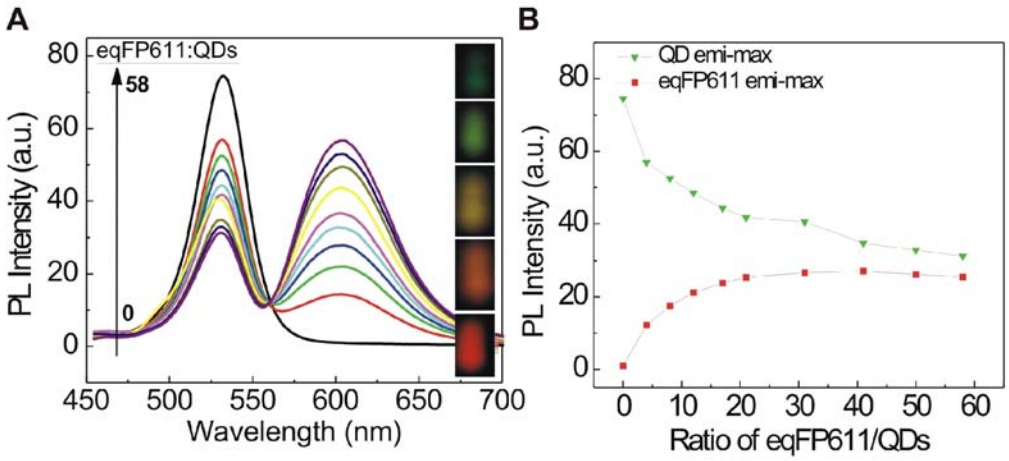

Figure 2.3.4 PL evolution of the NTA-PLs-QD/eqFP611 FRET system. (A) Titration of QDs with increasing molar ratios of eqFP611 measured at an excitation wavelength of 400 nm. The inset shows the titration mixture PL color changes (monitored by a digital camera) during the titration procedure, indicating the energy transfer process; (B) QD PL (green triangle) and eqFP611 PL (red square) as a function of the ratio eqFP611/QD. Note that the data for eqFP611 PL in (B) were corrected for the PL background from direct excitation.

Table 2.3.2 Measured efficiencies E, calculated overlap integrals J, Förster radii R_0, donor-acceptor distances r, structurally estimated donor-acceptor distances and the average eqFP611 monomer number on one QD N for the DHLA-QD536/eqFP611 and PLs-QD531/eqFP611 FRET systems

donor-acceptor pair	overlap integral, $J\times10^{-14}$ cm^{3}M^{-1}	Förster radius, R_0 (nm) [a]	efficiency E [b]	saturation number N	D-A distance, r from E (nm) [c]	D-A distance, r from structural estimate (nm)
DHLA-QD536/eqFP611	32.0	4.3	0.80	20	5.6	5.2
PLs-QD531/eqFP611	32.2	4.7	0.53	35	8.3	8.1

[a] based on eq 1.2; [b] estimated using eq 1.4; [c] estimated using eq 1.1;

A FRET efficiency of ~0.53 was obtained by comparing the PL of QDs before and after conjugation with ~35 eqFP611 monomers (Figure 2.3.4). This efficiency led to an average donor/acceptor distance of ~8.3 nm taking into account a Förster radius estimated to R_0 ~4.7 nm for the PLs-QD531/eqFP611 pair. This value is in good agreement with the one estimated from geometrical assumptions. The distance between eqFP611 monomer chromophore and QD center consists of the radius of the lipid-QD531 which is ~5.0 nm, the half diagonal length of protein monomer which is ~2.4 nm and the length

of His_6 tag of ~0.7 nm, all of which results in an overall estimate of ~8.1 nm. The FRET parameters and calculated results are summarized and listed in Table 2.3.2.

2.3.1.2 Energy transfer between QDs and EYFP

As mentioned earlier, in this work, a ~518 nm emitting DHLA-QD was used as an energy donor for His_6-tagged EYFP and EYFP-DNA conjugate and the FRET efficiency, donor/acceptor distances were investigated in detail. In this chapter, the evidence of an energy transfer between QD and EYFP will be discussed and compared with that from QD to EYFP-DNA conjugates. The detailed quantitative analysis of QD/EYFP-DNA system is presented in the next section.

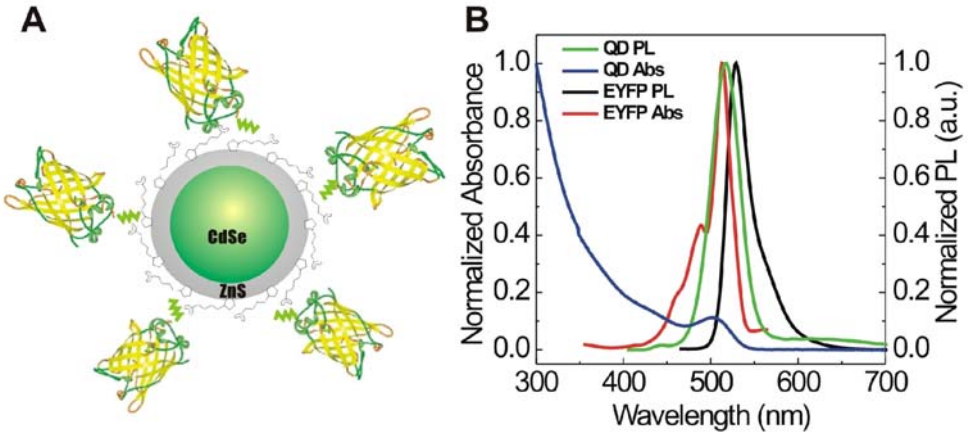

Figure 2.3.5 Schematic representation and spectral properties of a DHLA-QD518/EYFP donor/acceptor system. (A) multiple EYFP were adsorbed to DHLA-coated QD to form a QD/FPs conjugate; (B) spectroscopic characterization of the ~518 nm-emitting DHLA-QDs absorption (blue) and emission (green) and EYFP absorption (red) and emission (black).

As illustrated in Figure 2.3.5B, the large spectral overlap between the QD donor emission and the EYFP acceptor absorption is an advantage for the efficient energy transfer. Figure 2.3.6A shows the PL evolution of the QD/EYFP conjugates with increasing EYFP/QD ratio. To clarify changes in the spectral properties of the QD/EYFP system, disturbing emission from directly excited EYFP was subtracted by using PL spectra measured from samples containing similar concentrations of EYFP. In addition, the fluorescence intensity results are all normalized with respect to the fluorescence intensity of unconjugated QDs. It was evident from the titration that the adsorption of EYFP to the QD led to an increase in PL emission. Moreover, a significant red-shift of the emission peak from ~518 nm to ~528 nm was observed (inset of Figure 2.3.6A), suggesting an energy transfer from the QD donor to the

EYFP acceptors. The FRET was also further confirmed by the agarose gel electrophoresis, as shown in Figure 2.3.6C. The decreasing electrophoretic mobility corresponds to the continuous immobilization of His_6-tagged EYFP on DHLA-QDs. The enhanced PL of the gel bands of the EYFP/QD conjugate (EYFP:QD=2, 4, 6, 8) in comparison with that of EYFP alone confirms the energy transfer from QD to EYFP.

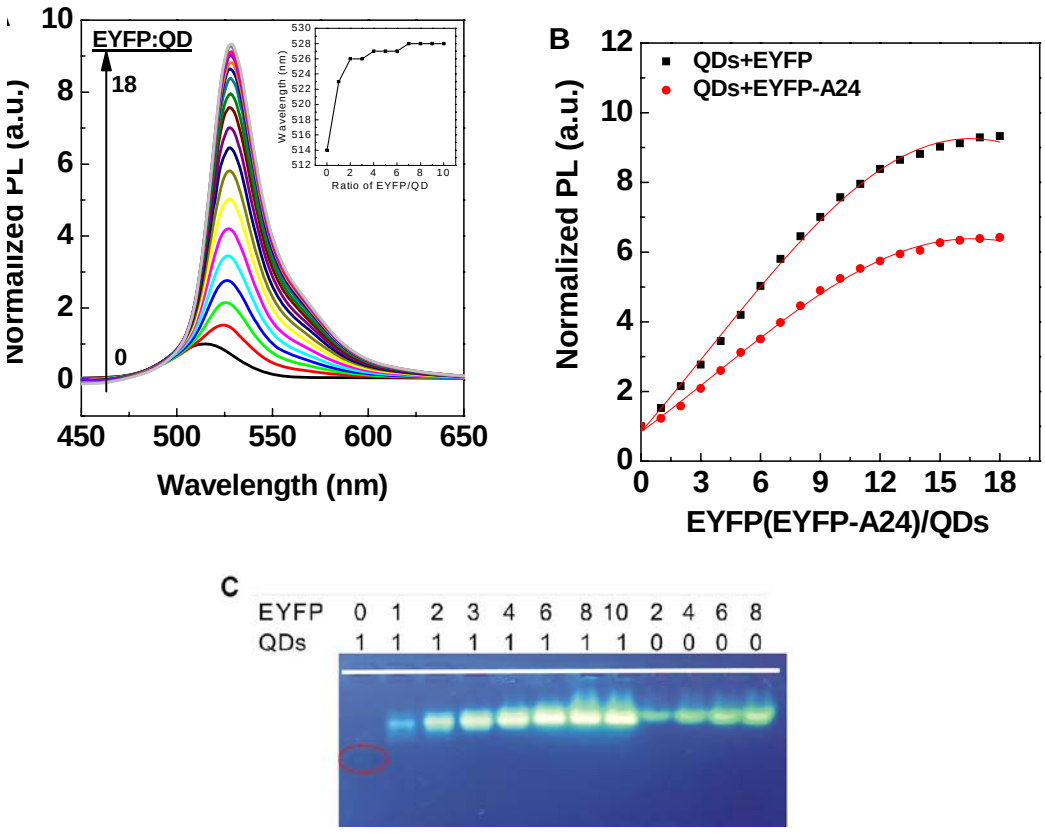

Figure 2.3.6 PL evolution of the DHLA-QD/EYFP FRET system. (A) Titration of QDs with increasing ratios of EYFP measured at an excitation wavelength of 372 nm. The inset shows the shift of the PL maximum with increasing ratio of protein. (B) PL enhancement as a function of the ratio EYFP/QD (black squares); EYFP-A24/QD (red dots). Note that all data were corrected for the EYFP PL background and normalized against unconjugated QDs. (C) 0.4% agarose gel electrophoresis of DHLA-QD/EYFP conjugates with the increasing ratios of EYFP/QD. The gel was illuminated with UV light.

The DHLA-QD allows multiple immobilization of EYFP on one particle (Figure 2.3.5A), which is confirmed by a titration experiment (Figure 2.3.6). The saturation was reached when ~13-16 EYFP were bound to one QD. This value is close to the coverage number estimated from the geometric considerations based on equation 2.1. This geometrical estimate leads to ~19 EYFP per QD using the

radius of QD518, R_1=~2.0 nm, the equivalent radius of EYFP, R_p=~1.8 nm. In order to fabricate a 3-chromophore multiple FRET system, EYFP was covalently coupled to a 24mer oligonucleotide A24, which introduced another fluorophore by hybridizing with dye-modified complementary oligonucleotides (detailed description see chapter 2.3.2). As a comparison, the EYFP-A24 conjugates were also used for the similar titration experiment and the PL maxima for each EYFP-A24/QD ratio were plotted in Figure 2.3.6B. There are two pieces of information obtained from Figure 2.3.6B. First, the surface protein coverage numbers for EYFP-A24/QD and EYFP/QD systems deduced from the PL saturation are almost the same, ~13-16, which means that the attachment of the 24-mer oligonucleotides has little effect on the packing space. Secondly, the PL enhancement effect of QD/EYFP-A24 was apparently smaller than that of QD/EYFP system. The reasons for this observation are currently unclear. However, one may speculate that the increased polarity of the EYFP-A24 might lead to a less efficient hydrophobic shielding of the QDs surfaces, as compared to the pure EYFP.

2.3.2 Three-chromophore FRET system of DHLA-QDs, EYFP and Atto647-dye modified oligonucleotides

It has previously been suggested that the combination of different types of fluorophores, such as inorganic luminescent nanocrystals, organic dyes, and genetically encoded fluorescent proteins offers a promising route for the fabrication of multi-chromophore systems.[61] In this work, the assembly and spectroscopic characterization of a DNA-based 3Ch-FRET system was investigated. In contrast to previous work concerning binary fluorescent protein-based FRET systems,[93, 148] three different types of fluorophores, QDs, EYFP and Atto647-modified oligonucleotides were employed here. The chemical synthesis and self-assembly of our 3Ch-FRET system is illustrated in Figure 2.3.7. ssDNA-EYFP conjugates (**1** in Figure 2.3.7A) were used, which contained the 24mer oligonucleotide A24, covalently linked to an engineered cysteine residue at the EYFP's C-terminus, in addition to a His_6 tail at the N-terminus.[149] Multiple conjugates **1** were adsorbed on the surface of DHLA-coated QDs, thus leading to the formation of a two-chromophore FRET system (**2** in Figure 2.3.7A). The DNA-EYFP conjugates in **2** were then used for specific hybridization with complementary ssDNA labeled with the organic dye Atto647 (**3**) to yield the final supramolecular system (**4** in Figure 2.3.7A). Due to the modular design, four different FRET systems (**4a**-**4d** in Figure 2.3.7B) could be readily assembled by hybridization of **2** with various complementary oligonucleotides, each of which contained the Atto647 dye coupled to a

different nucleotide (**3a** through **3d** in Figure 2.3.7B), thus, enabling to gradually vary the donor-acceptor distances of the FRET systems.

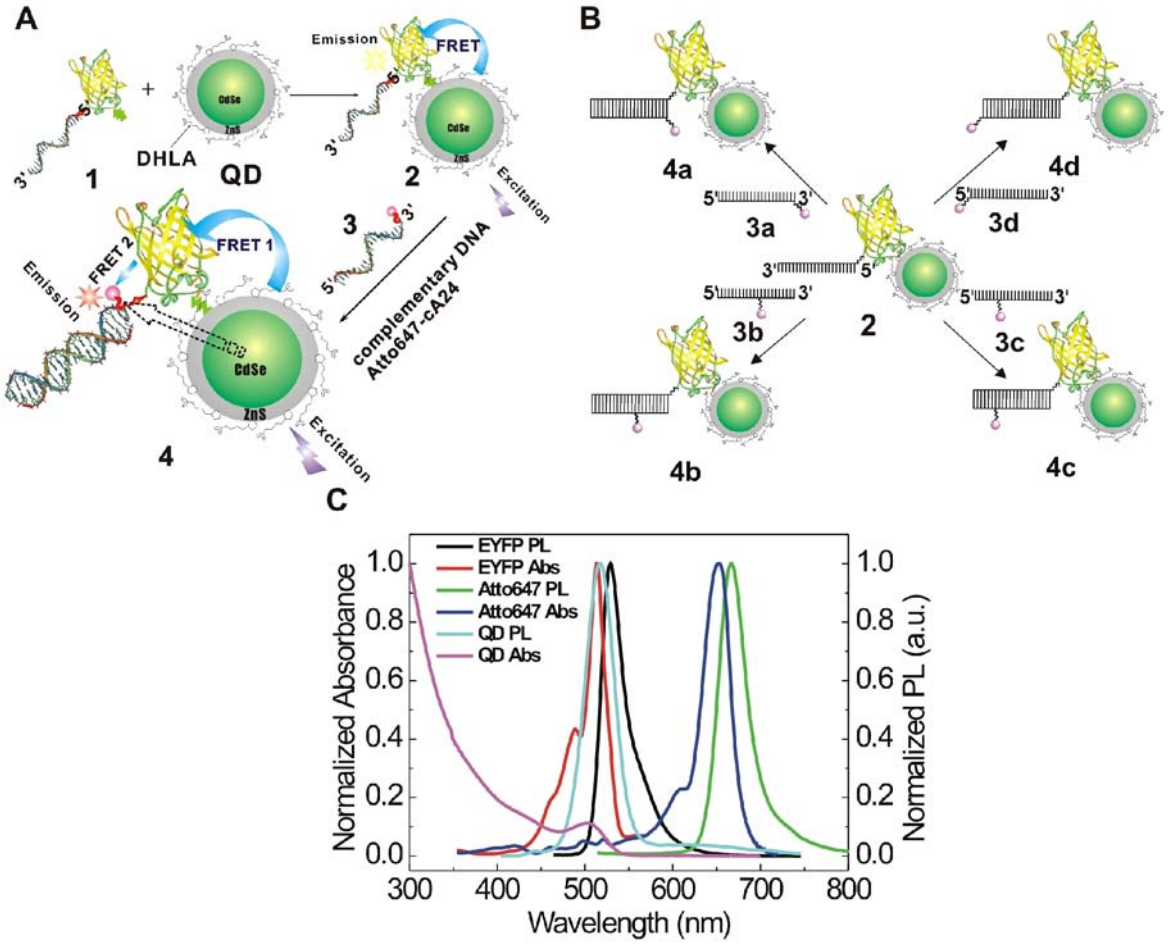

Figure 2.3.7 Schematic representation and spectral properties of the DNA-based 3Ch-FRET system QD-EYFP-Atto647. (A) Initially ssDNA-EYFP conjugates (termed as **1**) were adsorbed to DHLA-coated QDs to form QD-EYFP-A24 conjugate (**2**). Compound **2** is hybridized with complementary Atto647-modified ssDNA (**3**) to form the final 3Ch-FRET conjugate (4); (B) four different DNA-based QD-EYFP-Atto647 conjugates (**4a-d**) were assembled using four different Atto647-cA24 oligonucleotides (**3a-d**) comprising the Atto647 dye at the base pairs 0, 10, 17, or 24, respectively, counted from the 3'-end of **3**; (C) Spectroscopic characterization of the DHLA-QD's absorption (magenta) and emission (cyan), EYFP's absorption (red) and emission (black), and Atto647's absorption (blue) and emission (green).

2.3.2.1 Energy transfer processes in the two-chromophore FRET subsystems

In the course of this work the three two-chromophore (2Ch-FRET) subsystems, i.e., QD/EYFP, QD/Atto647, and EYFP/Atto647 initially were characterized, by using steady-state and time-resolved photoluminescence (PL) spectroscopy. Because the 2Ch-FRET system QD/EYFP exhibited spectrally strongly overlapping EYFP absorption and QD emission bands along with very close emission maxima of EYFP and QD (Figure 2.3.7C), FRET-efficiencies were difficult to derive from standard titration experiments. Therefore, several independent experimental approaches, i.e., Gaussian fitting of photoluminescence, photoluminescence excitation spectroscopy (PLE) and rate equation simulations of time-resolved luminescence were combined to measure and verify the energy transfer rates and efficiencies of the QD/EYFP subsystems. Subsequently, the FRET efficiencies of the full systems (**4a-4d** in Figure 2.3.7B) were then derived and compared with those efficiency data deduced from the independent 2Ch-FRET subsystems. The transfer efficiencies of all FRET pairs were translated into donor/acceptor distances by taking into account the respective Förster radii. The knowledge of these distances additionally allowed an estimation of the spatial arrangement of the multi-FRET constituents, which was compared to a geometric model taking into account the helicity of the DNA. Because this system, to the best of our knowledge, represents the first demonstration of a 3Ch-FRET system comprising QDs, fluorescent proteins and dye-labeled DNA oligonucleotides, it is anticipated that the results will open the door to further studies on the interaction of QDs and fluorescent proteins[75, 141] as well as to the development of general tools for the investigation of multi-protein and protein-DNA assemblies.

Prior to elucidation of the 3Ch-FRET system QD/EYFP/Atto647, the less complex 2Ch-FRET subsystems, namely QD/EYFP, QD/Atto647 and EYFP/Atto647 were initially characterized. The quantitative study of these FRET pairs required the knowledge of distinct parameters, such as the Förster radius or energy transfer rates. For the 2Ch-FRET systems QD/EYFP and QD/Atto647, where a single exciton donor can interact with several acceptors, the energy transfer efficiency depends on the molar ratio of acceptor and donor. E can be expressed as

$$E(N,r) = \frac{N}{N + \left(\frac{r}{R_0}\right)^6} \qquad 1.1$$

where N is the average number of acceptor molecules EYFP-A24 or Atto647 per one QD donor.[88, 90] In the QD/EYFP and QD/Atto647 systems, N=14 was chosen to ensure high FRET-efficiency but keeping

the number of acceptors below the observed saturation value of N_{sat}=~13-16 (Figure 2.3.8 A, B). Since conjugate **1** contains only one DNA oligomer per EYFP,[93] N=1 was chosen in the EYFP/Atto647 subsystem. The Förster radius R_0 defined as the distance between donor and acceptor that yields 50% energy transfer efficiency, can be calculated as[88]

$$R_0^6 = 8.8 \times 10^{23} \kappa_p{}^2 n_D{}^{-4} Q_D J \qquad 1.2$$

where Q_D is the quantum yield (QY) of the donor in the absence of an acceptor, and n_D is the refractive index of the medium; $\kappa_p{}^2$ is an orientation factor, depending on the relative orientation of the donor and acceptor dipoles. $\kappa_p{}^2$=2/3 is the value for randomly oriented dipoles, which is suited for the systems studied here.[91] The overlap integral J is a quantitative measure of donor-acceptor spectral overlap integrated over all wavelengths λ, and is defined as[88]

$$J = \int f_D(\lambda)\varepsilon_A(\lambda)\lambda^4 d\lambda \qquad 1.3$$

where f_D and ε_A represent the donor emission spectrum (normalized and dimensionless) and acceptor absorption spectrum, respectively. Using equation 1.3, the overlap integrals of the three 2Ch-FRET subsystems QD/EYFP, QD/Atto647 and EYFP/Atto647 were calculated with the help of the software *PhotoChemCAD*[146] and they are listed in Table 2.3.3. Experimentally, the efficiency E of a FRET process can, for example, be derived from the quenching of the donor fluorescence intensity, according to[88]

$$E = 1 - \frac{F_{DA}}{F_D} = 1 - \frac{\tau_{D-A}}{\tau_D} = \frac{k_{transfer}}{k_{rad} + k_{nonrad} + k_{transfer}} \qquad 1.4$$

where F_D and F_{DA} are the fluorescence intensities of the donor in the absence and presence of an acceptor; $\tau_{D\text{-}A}$ and τ_D are the fluorescent lifetimes of the donor in the absence and presence of an acceptor. k_{rad}, k_{nonrad} and $k_{transfer}$ are the radiative and nonradiative recombination rates and the transfer rate of the donor, respectively. Alternatively, the efficiency E can be determined by the acceptor fluorescence enhancement (if the acceptor is a fluorescent molecule), expressed as[92]

$$E = \frac{A_A(\lambda_D)}{A_D(\lambda_D)}\left[\frac{F_{AD}(\lambda_A)}{F_A(\lambda_A)} - 1\right] \qquad 1.5$$

where λ_D is the donor excitation wavelength; A_D and A_A are the donor and acceptor absorbance at the wavelength λ_D; F_{AD} and F_A are acceptor fluorescent intensities at the acceptor emission wavelength λ_A in the presence and absence of a donor. Despite the simplicity of donor quenching strategy, there might be other non-FRET sources that cause donor quenching. However, gain in acceptor fluorescence comes

directly from the donor nonradiative energy transfer. Under ideal conditions, every exciton is nonradiatively transferred from donor to acceptor and this brings the donor photoemission loss which could be fully recovered as energy gain by the acceptor. That explains why the efficiency from donor quenching is a little higher than the one from acceptor PL increase. The efficiencies *E* of the four different 2Ch-FRET subsystems QD/Atto647 were calculated from acceptor PL gain. The absorbance at the wavelength of 372 nm of QD and Atto647 were required in this case. Because the relatively weak absorption at 372 nm of EYFP brought large errors the calculation of efficiency from acceptor PL gain for QD/EYFP and EYFP/Atto647 pairs, the efficiency *E* of the QD/EYFP and four EYFP/Atto647 subsystems were obtained from donor PL quenching. All the efficiency data were verified by combining several experimental methods, in particular, 2D-PLE, time-resolved luminescence and titration results. Note that equations 1.1-1.5 were also presented earlier in the introduction chapter 1.3.

Table 2.3.3 Measured efficiencies *E*, calculated overlap integrals *J*, Förster radii R_0, donor-acceptor distances *r* and structurally estimated donor-acceptor distance for the three 2Ch-FRET subsystems **2**, **5a-d** and **4a*-d***.

donor-acceptor pair	overlap integral, $J\times10^{-14}$ cm^3M^{-1}	Förster radius, R_0 (nm)	efficiency	D-A distance, r from E (nm)[a]	D-A distance, r from structural estimate (nm)
QD/EYFP in **2**	29.4	3.86	0.72±0.02	5.11±0.06	5.1
EYFP/Atto647 in **5a**	8.00	4.83	0.78±0.02	3.91±0.08	4.2
EYFP/Atto647 in **5b**			0.43±0.02	5.06±0.07	5.4
EYFP/Atto647 in **5c**			0.23±0.03	5.91±0.16	6.3
EYFP/Atto647 in **5d**			0.072±0.02	7.40±0.44	8.3
QD/Atto647 in **4a***	8.80	3.16	0.31±0.02[b]	5.61±0.09	4.5
QD/Atto647 in **4b***			0.12±0.02	6.84±0.20	7.4
QD/Atto647 in **4c***			0.028±0.001	8.86±0.05	9.3
QD/Atto647 in **4d***			0.003±0.002	12.9±1.1	12.1

[a] Estimated using $r=R_0*(N(1-E)/E)^{1/6}$, N=14 for the QD-Atto647 and QD/EYFP pair and N=1 for the EYFP/Atto647 pair; [b] The efficiencies of four different QD/Atto647 pairs were obtained from acceptor PL gain
* bleached EYFP-A24 (**1***) was used for assembly

- **QD/EYFP 2Ch-FRET subsystem.**

A peculiarity of the QD/EYFP FRET pair is its large spectral overlap between the QD donor emission and the EYFP acceptor absorption which is reflected by a large overlap integral *J*. (see Table 2.3.3) While such strong overlap is necessary to yield highly efficient energy transfer, the PL quenching of the QDs is difficult to extract due to the spectral overlap of the QD and EYFP emission (see Figure 2.3.7C). To analyze the FRET process, three independent experiments were therefore carried out: (i)

titration of QDs with an increasing number of EYFP-A24 conjugates per QD, (ii) comparison titration of QD with photobleached EYFP-A24* conjugates (i.e., QD/**1***) (Figure 2.3.8) and (iii) measurement of the PL-dynamics and modeling of the energy transfer rates using rate equation systems (see Figure 2.3.10). As outlined below, all three methods led to similar and thus consistent results.

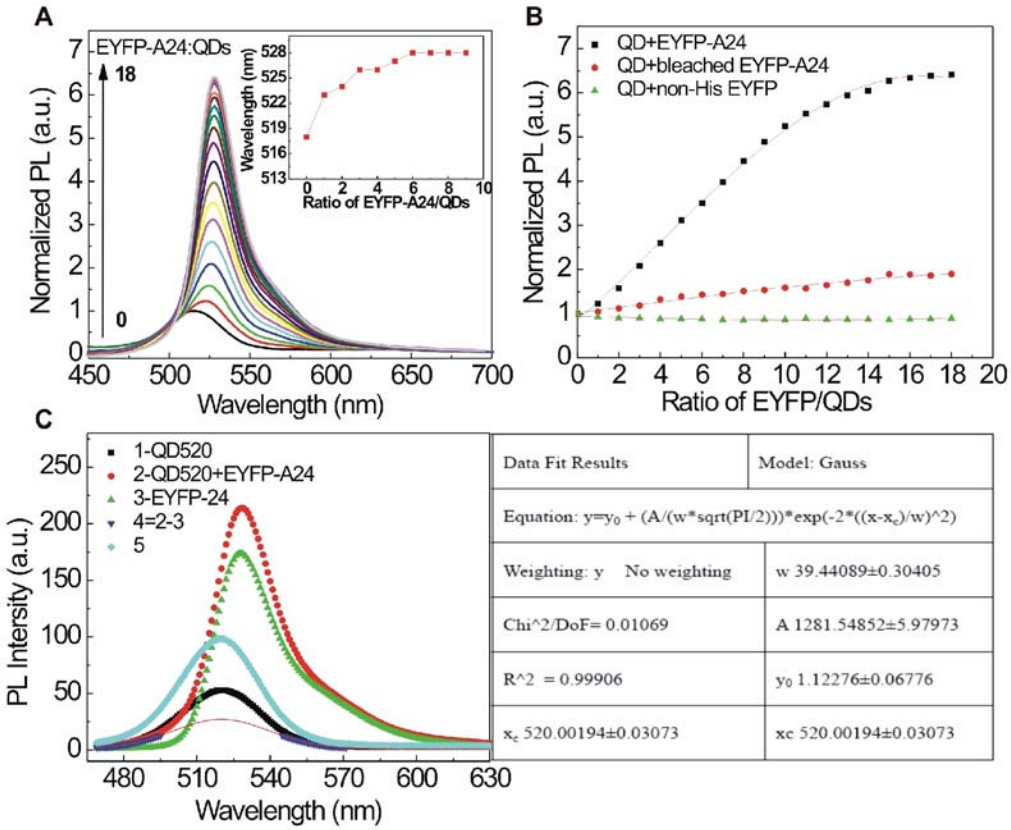

Figure 2.3.8 PL evolution of the 2Ch-FRET subsystem QD/EYFP (conjugate **2** in Figure 2.3.7A). (A) Titration of QDs with increasing ratios of EYFP-A24 (**1**) measured at an excitation wavelength of 372 nm. The inset shows the shift of the PL maximum with increasing ratio of **1**. (B) PL enhancement as a function of the ratio **1**/QD (black squares); **1*/QD** (red dots) and the control experiment comprising QDs and non-histidine tagged EYFP (green triangles). Note that all data were corrected for the EYFP PL background and normalized against unconjugated QDs. (C) Procedure of extraction and recovery of the QD emission from the PL overlapping spectra and Gaussian fit output (right panel table). Red dotted curve B represents a normal emission spectra of the QD/EYFP-A24 conjugate (i.e. **2**) including the overlap of QD520 and EYFP-A24 (528 nm) emission; green triangle curve C represents the EYFP-A24 emission which has been adjusted to the same intensity as curve B in the range of ~560-600 nm, where the QD PL intensity is close to zero. The blue triangle curve D was obtained by subtracting the curve C from the curve B. The data from D in the range of ~469-495 nm (where the EYFP emission intensity is close to zero, see green curve C) was used for the later Gaussian fit. This signal in the range of ~469-495 nm can be mirrored to the range of ~545-571 nm, due to the spectrum symmetry of the QD

emission (centered ~520 nm). A Gaussian fit (red solid curve) is obtained with the analysis function of *Origin 7*. The cyan diamond curve E is the emission spectrum of conjugate **2*** (QD/bleached EYFP-A24), which resembles the QD emission signal at the absence of acceptors F_D. The FRET efficiency can finally be obtained by comparing this curve E and the fitting red solid curve based on equation $E=1-F_{AD}/F_D$.

The results of the titration experiments are shown in Figure 2.3.8. The coverage of the QD surface with EYFP molecules can theoretically be estimated by the equation 2.1. Not like eqFP611, EYFP are mostly monomers at normal conditions.[149] The packing of EYFP on QD surface was only limited by space. In this model, the protein molecules are assumed as close-packed spheres around the central QD. Being a mutant of *aequorea* GFP, EYFP as well has a β-barrel structure with a diameter of ~2.3-3.0 nm and a length of ~4.0-4.2 nm, similar to that of GFP.[145] Comparative titration experiments, carried out with QD and EYFP, showed that saturation occurred at approximately 13-16 molar equivalents of protein per QD and this was very similar for QD and EYFP-A24 (**1**) (Figure 2.3.6B). This result is in good agreement with a theoretical estimation of surface loading, using values of R_p=~1.8 nm (equivalent radius for a EYFP protein), R_1 ~1.9 nm for the CdSe/ZnS QD with an emission of ~518 nm (estimated from TEM images) and the filling factor of 0.65 for equation 2.1, leading to $N_{EYFP\text{-}A24}$ ~18 per QD. Figure 2.3.8A shows the PL evolution of the 2Ch-FRET subsystem QD/EYFP with increasing EYFP/QD ratio. To clarify changes in the spectral properties of the QD/EYFP system, disturbing emission from directly excited EYFP was subtracted by using PL spectra measured from samples containing similar concentrations of EYFP-A24 (**1**). In addition, the fluorescence intensity results were all normalized with respect to the fluorescence intensity of unconjugated QDs. It was evident from Figure 2.3.8A, that the adsorption of **1** to the QD led to an increase in PL emission. Moreover, a significant red-shift of the emission peak from ~517 nm to ~528 nm was observed (see inset of Figure 2.3.8A), suggesting an energy transfer from the QD donor to the EYFP acceptors. To verify that these spectral changes, indeed, were due to FRET processes, control experiments were carried out using a non-His_6-tagged EYFP. It is shown in Figure 2.3.8B (green triangles) that this titration led to only negligible enhancement in fluorescence and no shift of the emission peak, as compared to the results obtained with the His_6-tagged EYFP (black squares). Thus, the experiments supported the hypothesis that the binding of EYFP to the surface of QDs led to Förster energy transfer from QD to **1**. The FRET efficiency E of this QD/EYFP 2Ch-FRET subsystem was calculated using equation 1.4, using the intensity of the QD emission extracted from the total PL-spectrum by Gaussian fits (Figure 2.3.8C). The latter were used because the spectral overlap of EYFP and QD emission brings with it difficulties

for data analysis. Therefore Gaussian fitting were used based on the narrow and symmetric QD emission properties, which helped to extract the QD emission spectra from the overlap. This approach enabled the reproduction of the PL shape with high accuracy. The QD PL emission in the absence of acceptors should be equal to the emission obtained from the QD/bleached EYFP-A24 conjugates (**2***), because **2*** comprises the modification of the QD-quantum yield (here a PL enhancement) due to shielding of negatively charged DHLA-QDs by the adsorbed positively charged protein domains (i.e. polyhistidine). As illustrated in Figure 2.3.9, the photobleaching strategy of EYFP-A24 conjugates provides a non-fluorescent species for control experiments such as the study of QD PL enhancement effect due to QD-protein interaction and the FRET study of QD/Atto647 subsystems described below. Taking into account this PL enhancement effect, a high FRET efficiency of E~0.72±0.02 was obtained, suggesting that, as a result of very efficient FRET, the QD/EYFP 2Ch-FRET subsystem should act as a new, combined donor complex within the anticipated 3Ch-FRET system.

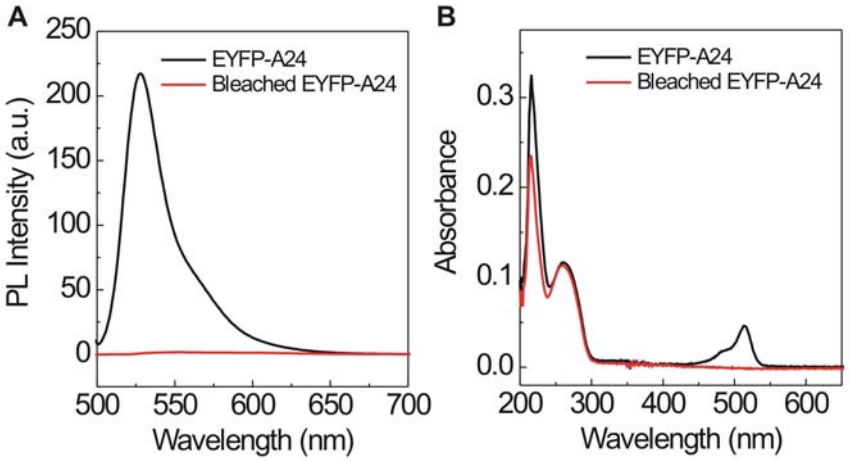

Figure 2.3.9 Spectroscopic characterization of EYFP, EYFP-A24 and photobleached EYFP-A24 conjugates. The samples were diluted to 0.5 µM in TETBS buffer and excited at 488 nm. (A) Fluorescence spectra comparison: the PL of EYFP has ~38% enhancement after conjugation with A24 and completely disappeared after irradiating with laser. (B) Absorbance comparison of EYFP, EYFP-A24 and bleached EYFP-A24 conjugates: The UV absorption peaks below 300 nm remained almost unchanged, while the absorption peak of EYFP centered at 514 nm disappeared completely after photobleaching.

To confirm the calculated number of E~0.72, the temporal evolution of the 2Ch-FRET subsystem QD/EYFP was investigated by time-resolved fluorescence spectroscopy (Figure 2.3.10). To this end, samples containing the QD/EYFP conjugates were excited with pulsed laser light of the same wavelength used in the aforementioned time integrated PL experiments. As indicated from Figure

2.3.10, the QD/EYFP system's emission qualitatively showed an increase in intensity, which reached its maximum at approximately 1 ns after the arrival of the exciting laser pulse. This can be explained by the energy transferred from the QD to the EYFP, due to which the decrease of the QD PL is accelerated, while the EYFP emission gains intensity until the feeding reservoir of the QD is depleted. For comparison, the PL decay of a sample comprising QDs and photobleached EYFP-A24 (**2***) was measured and found to display a fast initial decay in the first 100 ps, before a monoexponential decay with a time constant of ~3.5 ns becomes visible. This decay time and the measured quantum yield of 6.6 % translate into a radiative decay rate of 0.019 ns^{-1}. For a more quantitative analysis, the emission was spectrally binned over a wavelength range around the maximum of combined QD/EYFP emission, centered at 528 nm to produce an intensity vs. time plot representation. The fraction of the total QD emission present in this region, as well as the corresponding value for the EYFP, were extracted from time integrated measurements. For the numerical simulation of the energy transfer rates, the following channels of population and depopulation have been taken into account: The QD is excited by the laser and releases the energy via radiative recombination, non radiative recombination and transfer to the EYFP. The protein is excited by the laser as well, though to a much smaller extent due to the absorption cross section at the chosen excitation wavelength of 372 nm. Additionally, the transferred energy from the QD donor populates this excited state of the acceptor which is depopulated by radiative and nonradiative channels. Rates represent the strength of the respective energy migration channels and enabled the calculation of excitation processes occurring in the QD and the EYFP in an iterative way. The programming algorithm for the simulation was developed by Oliver Schöps[150] and is shown in the appendix of this thesis (Section 7.2). The simulated results were obtained with the following parameters for QD and (EYFP), respectively: molar ratio: 1 (14), QY: 0.066 (0.62), radiative decay rate: 0.019 ns^{-1} (0.20 ns^{-1}), and transfer rate of QD to EYFP of 0.053 ns^{-1}. These FRET transfer rates are consistent with the FRET efficiency value *E* obtained from the titration experiments. The excellent match with the observed dynamics confirmed the high FRET efficiency in the 2Ch-FRET subsystem QD/EYFP.

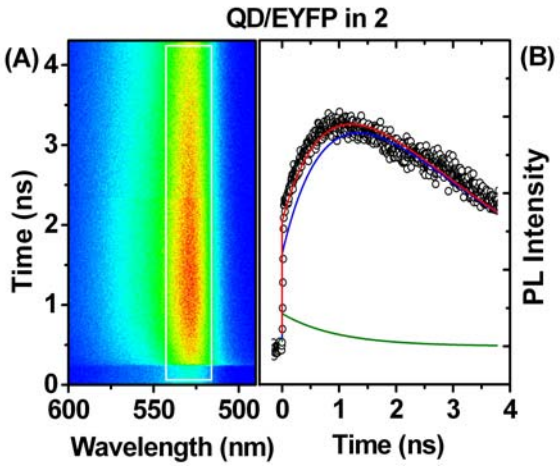

Figure 2.3.10 Temporal evolution of the PL signal of the 2Ch-FRET subsystem QD/EYFP (**2**). (A) Spectrally and temporally resolved dynamics of the conjugate emission. The region over which the intensity was spectrally integrated to generate the cut, shown in the right panel, is indicated by the white box. (B) Emission dynamics of the spectrally integrated QD/EYFP conjugate (black dots). The red curve shows the simulated overall intensity of the two-chromophore system with the parts contributed by the QDs (green) and the EYFP (blue). The simulated results were obtained using the parameters for QD (EYFP): molar concentration 1 (14), QY 0.066 (0.62), radiative decay rate 0.019 ns^{-1} (0.20 ns^{-1}), transfer rate QD to EYFP 0.053 ns^{-1}.

According to equation 1.1, a FRET efficiency E~0.72 results in a distance of r = ~5.11±0.06 nm between the QD center and the EYFP center, taking into account a Förster radius of R_0=3.86 nm for the QD/EYFP 2Ch-FRET subsystem (Table 2.3.3). This value for r is in good agreement with the estimate from geometrical considerations that take into account the size of the QD, the dimension and shape of EYFP and the interaction between these two fluorophores. The QD is attached to the barrel shaped EYFP molecule through its N-terminal His_6 residue, which should position the QD into the region underneath the 'barrel bottom'. Considering the three-dimensional structure of EYFP, the distance between the centers of the QD and EYFP can be estimated by adding half of the diagonal length of the EYFP barrel (~2.4 nm), the QD radius (~2.0 nm) and the length of the His_6 tail (about 0.7 nm when all polyhistidine residues are coordinated to the QD surface[106]). This yields a value of r = ~5.1 nm which nicely correlates with the value obtained from experimental data.

- **EYFP/Atto647 - 2Ch-FRET subsystem**

In this work the previous study performed by Florian Kukolka was continued by investigation the two Atto647-containing 2Ch-FRET subsystems, schematically depicted in Figure 2.3.11A following the strategy proposed in previous work.[93, 148, 151] The resulting data of the isolated EYFP/Atto647 system,

i.e., conjugates **5a-d**, comprising different separation distances between the two fluorophores, are listed in Table 2.3.3. Briefly, the conjugate **1** hybridized with 4 Atto647-DNA conjugate **3a-d** (Atto647 attached to 0, 10, 17 and 24 bp), respectively. The energy transfer efficiencies for **5a-d** were measured to be 0.78±0.02, 0.43±0.02, 0.23±0.03, 0.072±0.02, respectively. The efficiency led to the D/A separation distances of ~3.91, 5.06, 5.91 and 7.40 nm, respectively and this agreed well with the distances estimated from the geometric model.[93] The data clearly indicate the expected decrease in transfer efficiency upon increased donor-acceptor distances.

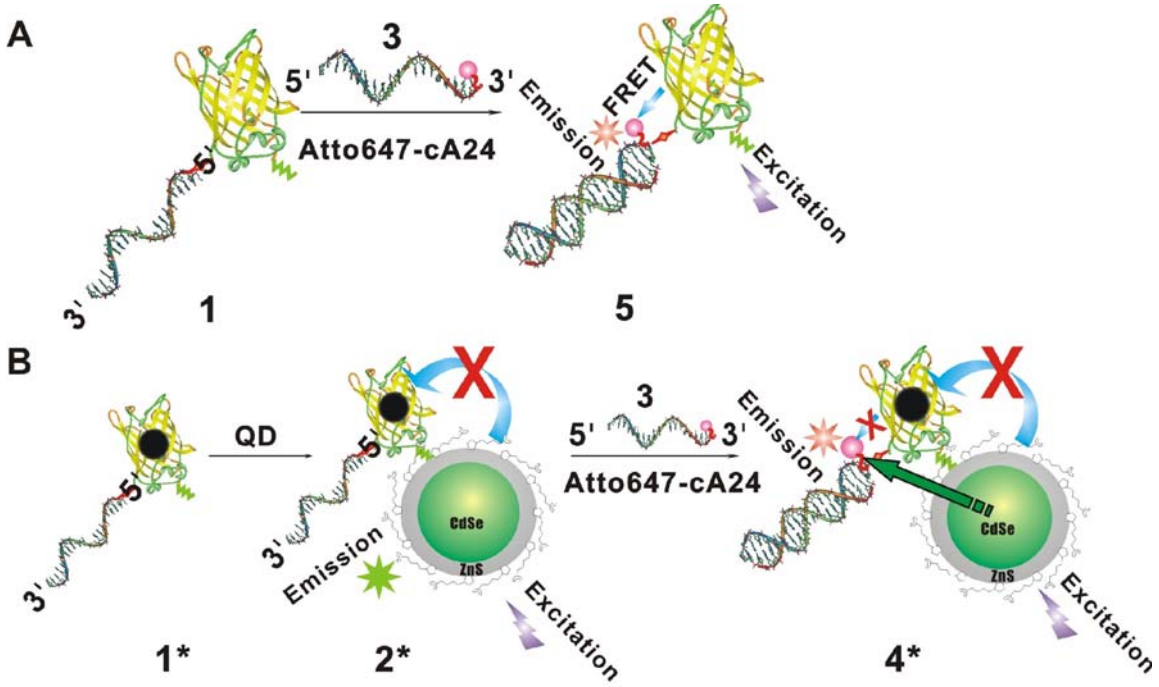

Figure 2.3.11 Schematic representation of the 2Ch-FRET subsystems EYFP/Atto647 and QD/Atto647. (A) Assembly of the EYFP/Atto647 subsystem (**5**) by hybridization of EYFP-A24 (**1**) with cA24-Atto647 (**3**). (B) Assembly of the QD/Atto647 subsystem (**4***) comprising photobleached EYFP-A24 (**1***) as the bridge in between the QD and Atto647-labeled oligonucleotides.

- **QD/Atto647 - 2Ch-FRET subsystem**

In contrast to the aforementioned studies on the 2Ch-FRET subsystems QD/EYFP and EYFP/Atto647, which were performed on the actual binary FRET-systems, it was necessary to analyze the direct energy transfer between QD and the Atto647-labeled oligonucleotides by using the ternary complex comprised of QD, EYFP, and Atto647. To facilitate direct QD-to-Atto647 energy transfer, photobleached, and thus dark, EYFP-A24 (**1***) which was prepared by prolonged irradiation with an

argon laser was used. Due to the non-fluorescent state of **1***, the FRET channel from QD to EYFP and from EYFP to Atto647 is blocked, thereby directing the energy transfer from the QD directly to Atto647 in this 2Ch-FRET subsystem (**4***). This allowed one to explore the influences of chromophore separation distance on FRET processes occurring in the respective conjugates **4a***-**4d*** (Figure 2.3.12).

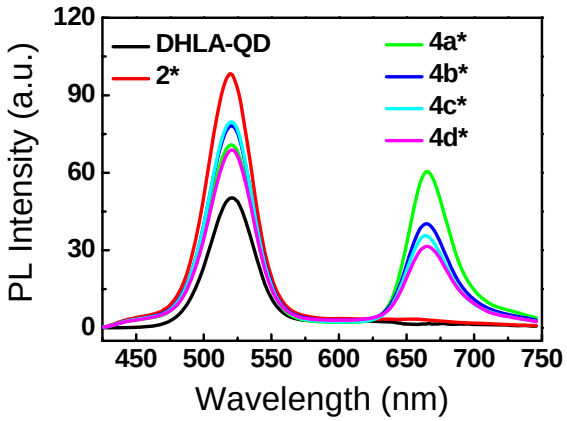

Figure 2.3.12 PL spectra of the four different QD/Atto647 2Ch-FRET subsystems **4a***, **4b***, **4c*** and **4d***. The QD emission is centered at ~520 nm, the Atto647 PL signal at 667nm. The additional curves indicate the spectra obtained for DHLA-QDs only (black) and QDs to which photobleached EYFP-A24 (**1***) was adsorbed (red). The excitation wavelength was 372 nm.

The energy transfer efficiencies of the four 2Ch-FRET subsystems **4a***-**4d*** was derived from the changes in the emission spectra measured for **4a***-**4d*** with respect to a reference spectrum obtained from QDs which were saturated with photobleached EYFP (**2***). Conjugate **2*** was chosen because the protein coating of QDs led to an approximately twofold enhancement in QD PL (Figure 2.3.8C). The transfer efficiency was calculated both from the quenching of the QD PL (equation 1.4) and the PL gain of the Atto647 (equation 1.5) obtained from Figure 2.3.12. The observed quenching of QD PL in conjugates **4*** confirmed the direct FRET form QD to the Atto647-labeled oligomer. Based on QD quenching, an efficiency of ~0.32±0.02 was calculated for conjugate **4a***. For comparison, an efficiency of ~0.31±0.02 was obtained when the gain of the Atto647 emission was used for calculation. The latter method was also used to calculate FRET efficiencies occurring in conjugates **4b***-**4d***. All values obtained are listed in Table 2.3.3. They clearly indicate the expected dependence of FRET efficiency from the donor-acceptor distance, as realized in **4a***-**4d***. The efficiency data were then used to calculate the separation distances between the QD center and the Atto647 dye, leading to distances of ~5.61±0.09, 6.84±0.20, 8.86±0.05 and 12.9±1.1 nm for **4a***-**4d***, respectively.

- **FRET parameters of the 2Ch-FRET subsystems**

Due to their lower complexity, the three 2Ch-FRET subsystems investigated were well analyzable and the results suggested that they form a suitable basis of the intended three-chromophore FRET system. The various efficiencies *E*, calculated overlap integrals *J*, Förster radii R_0, donor-acceptor distances *r* and structurally estimated donor-acceptor distance of the three 2Ch-FRET subsystems, **2** (QD/EYFP-A24), **5a-d** (EYFP-A24/cA24-Atto647), and **4a*-d*** (QD/EYFP-A24/cA24-Atto647 containing photobleached EYFP) are summarized in Table 2.3.3. The results obtained for **2** confirmed the expected high FRET efficiency of E=0.72, which is most likely due to the existence of 14 parallel QD-to-EYFP transfer channels, all of which exhibit the high value of the overlap integral *J* which compensates for the small quantum yield QY of the DHLA-capped QDs (in contrast to the high QY of the EYFP). The other two 2Ch-FRET systems exhibited similar spectral overlap integrals, however slightly different Förster radii of 4.83 nm (EYFP/Atto647) and 3.16 nm (QD/Atto647). Because of the relatively low QY of the DHLA-capped QD used here and the larger separation between chromophores, the QD/Atto647 subsystem revealed significantly smaller, but not negligible FRET efficiencies. It was therefore interesting to see whether this latter transfer acts as a competitive side channel in the three-chromophore FRET system as well, or whether its relative contribution is decreased due to the presence of the stronger parallel transfer occurring from QD/EYFP to the Atto647.

2.3.2.2 Energy transfer processes in the three-chromophore FRET

The 3Ch-FRET system, as depicted in Figure 2.3.7, comprises the combination of two competitive FRET channels, namely, that from QD to Atto647 and that from QD to EYFP to Atto647, which will be modified, and finally controlled, in their individual weightings in the total FRET process. Figure 2.3.13 illustrated vividly the PL emission and solution fluorescence evolution as the continuous addition of acceptors EYFP-A24 and later Atto647-cA24, which demonstrates the panoptic energy transfer process. For the quantitative characterization of the strength of an energy transfer channel, two representations are common. The use of the transfer rate which can be interpreted as the probability of an excitation being transferred within a given time interval is a measure of the absolute magnitude of energy transfer. The transfer efficiency, which is easily connected to measured quantities, weights the energy transfer channel with respect to all other present channels of energy loss. The two complementary representations are connected via equation 2.2.

$$E = 1 - \frac{F_{DA}}{F_D} = 1 - \frac{\tau_{D-A}}{\tau_D} = \frac{k_{transfer1}}{k_{rad} + k_{nonrad} + k_{transfer1} + k_{transfer2}} \qquad 2.2$$

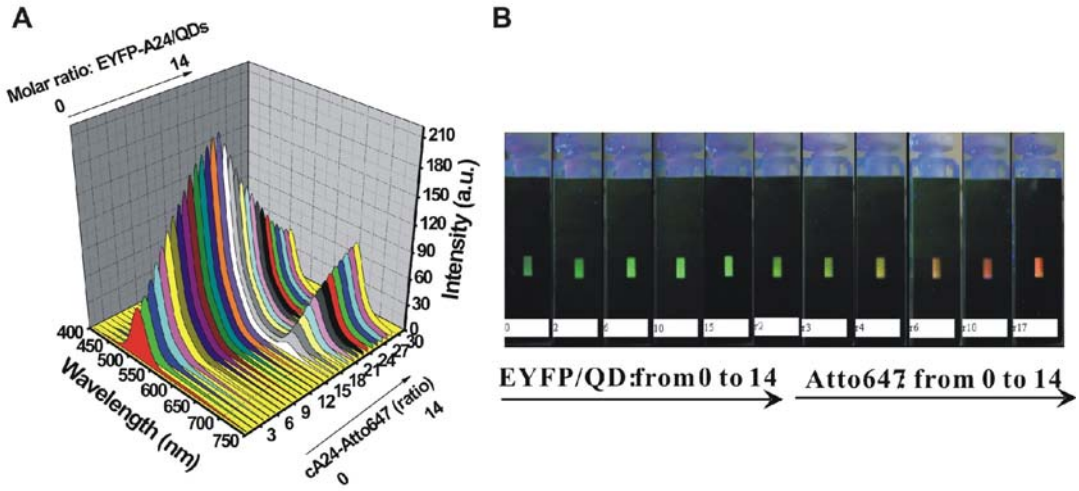

Figure 2.3.13 (A) PL evolution sample of a two-step titration procedure: 0-14 molar equiv of EYFP-A24 conjugates (**1**) were added to the one fold DHLA-QDs TETBS solution, subsequent adding of 0-14 equiv of cA24-3'-Atto647 conjugates (**3**) to the resulting conjugate **2**, which illustrates a two-step FRET from QD to EYFP then to Atto647 dye. (B) Titration mixture PL color (monitored by a digital camera) changes during the titration procedure, indicating the energy transfer process.

In the efficiency representation the presence or absence of a competitive energy transfer channel can change the efficiency value, even if the original strength of transfer, given by the transfer rate is not altered. In this way efficiencies can be tailored by offering alternative pathways of energy migration. From the assembly point-of-view, preformed QD-EYFP-A24 conjugates **2** were allowed to hybridize with 14 molar equiv of the Atto647-labeled complementary oligonucleotide **3** to yield the ternary target conjugates **4a-d**. The alternative strategy, that is to add to a solution containing QDs 14 equiv of pre-formed EYFP-DNA-Atto647 (**5**) led to identical effects in PL, thus suggesting that the self-assembly of the three components, indeed, occurred as expected. The constitution of target conjugates **4a-d** is similar to that of the 2Ch-FRET subsystem **4a*-d*** because the bleaching of EYFP (in **4***) only damages the chromophore center but not the protein's conformation,[152, 153] it was therefore assumed that the QD/EYFP, EYFP/Atto647 and QD/Atto647 donor-acceptor separation distances within **4** were similar to those estimated from the respective two-chromophore subsystems listed in Table 2.3.3.

The pathways of energy migration were unraveled in **4** by comparing the energy transfer efficiencies derived from the measurements of **4** with those obtained from the systems possessing only a single

transfer channel (**2, 4*, 5**). It was expected that the efficiency of the EYFP to Atto647 transfer remains unchanged, because neither the distances nor spectral overlap or other parameters influencing the energy transfer were changed. The opening of an additional depopulation channel for the QD, by allowing it to transfer energy not only to the EYFP, but also directly to the Atto647 dye, however, should influence the values for the transfer efficiency. This can be seen most clearly from the definition of transfer efficiencies as a function of the transfer rates *k*, as indicated in equation 2.2. The radiative and non-radiative rates are those defining the QDs' intrinsic quantum yield and, therefore, they should be constant in all of the assemblies investigated. While the transfer rate is simply the QD to EYFP transition rate in system **2**, and the QD to Atto647 transition rate in system **4***, it needs to be understood as the sum of the QD to EYFP and the direct QD to Atto647 rate in the 3Ch-FRET system.

2.3.2.3 FRET parameters of the 3Ch-FRET system derived from PL and 2-PLE Data

Figure 2.3.14 shows an overview of the donor-acceptor emission spectra measured for the four 3Ch-FRET systems **4a-d**. Figure 2.3.14A shows a map of the emission measured by so-called two dimensional photoluminescence exemplary 3Ch-FRET system **4a-d**. In Figure 2.3.14B, the PL spectra are plotted for the four 3Ch-FRET systems **4a-d** as well as for the reference systems QD only and QD/EYFP-A24 (conjugate **2**), all excited at 372 nm**.** To explore possible spectral dependencies of the FRET efficiencies caused by quantum-confinement induced spectral modifications in the QD-absorption cross section, the emission characteristics were initially mapped as a function of excitation wavelength (2D-PLE) over a broader spectral window, as illustrated in Figure 2.3.14A. The excitation wavelength was tuned from short excitation wavelengths/high energies (350 nm/3.54eV) towards longer wavelengths/lower energies (700 nm/1.77eV) in steps of 1 nm while recording for each excitation the corresponding emission spectrum within a detection range between 500 and 700 nm. Excitation wavelengths longer than 550 nm show the directly excited Atto647 emission. The 450 to 550 nm part (enhanced twofold) shows the transfer from the QD/EYFP subsystem to Atto647. The bottom part (enhanced 15x) shows direct Atto647 excitation, QD-Atto647 transfer and the sequential QD-EYFP-Atto647 transfer. FRET processes were evidenced in the two-dimensional-PLE (2D-PLE) of Figure 2.3.14A by the off-diagonal transfer peak. This appeared as PL intensity at the spectral position of the acceptor's recombination wavelength, while the system was excited at wavelengths of strong donor absorption.[93] In contrast to an organic dye or a fluorescent protein, where the

luminescence is excited within a narrow band, the semiconducting nature of QDs provides well defined electron hole pair states within the QD. The resonance energy of the states is modified by the confinement potential which is directly related to the size. Consequently, the size distribution within the QD ensemble smears out the sharp absorption peaks and produces the well known absorption spectrum as shown in Figure 2.3.7C. It is the simultaneous mapping of a whole emission wavelength range as a function of excitation wavelength, which enables the determination of spectral windows, suited for the analysis of the FRET subsystems. The spectral region from 450-520 exhibits QD absorption, but the onset of the absorption of the EYFP prohibits the observation of the QD to Atto647 transfer. The analysis of the FRET pathways from QD to Atto647, therefore, has to focus on the excitation in the wavelength range of 350 to 400 nm, which is shown, 15-fold magnified, in the lower spectral window in Figure 2.3.14A. At an excitation wavelength of 372 nm, the transfer signature is strong and not concealed by emission stemming from direct excitation of the Atto647, while the EYFP absorption is negligible. The quantitative analysis of energy transfer efficiencies was therefore limited to the selected excitation wavelength of 372 nm (Figure 2.3.14B).

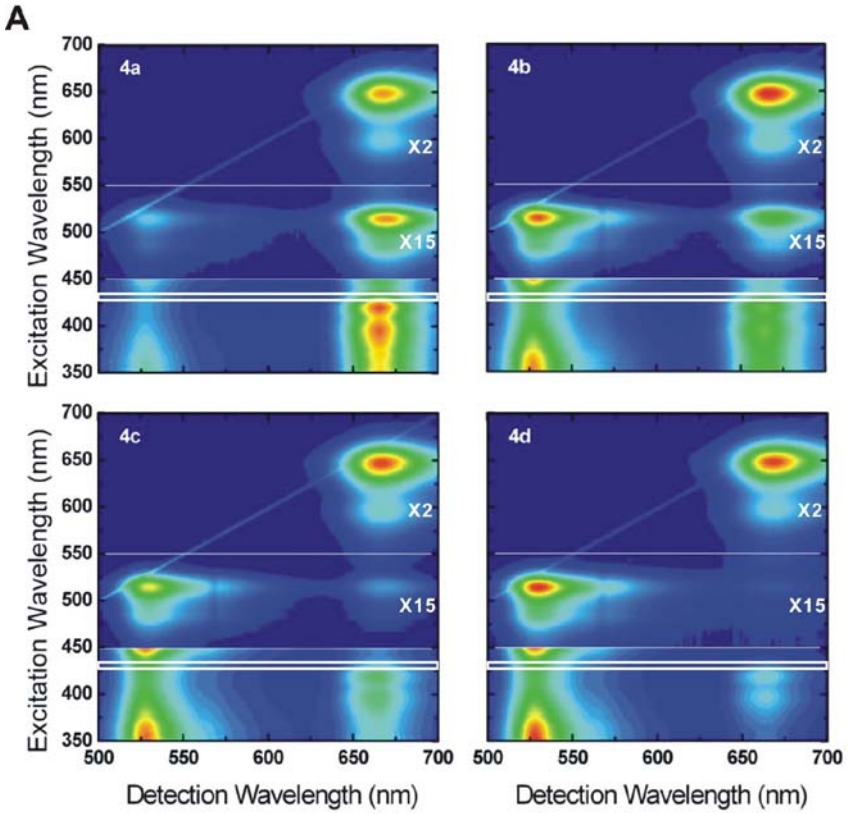

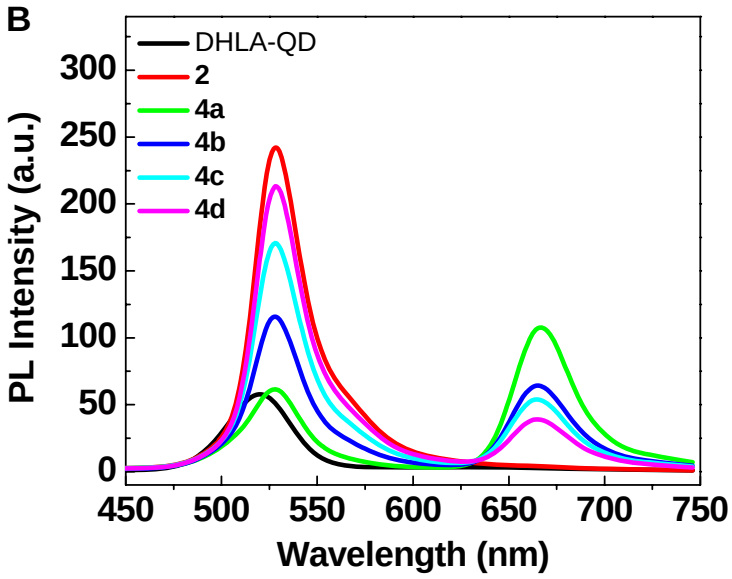

Figure 2.3.14 (A) Full excitation-emission characteristic as measured by 2D-PLE for systems **4a-d**. Excitation wavelengths longer than 550 nm show the directly excited Atto647 emission. The 450 to 550 nm part (enhanced twofold) shows the transfer from the QD/EYFP subsystem to Atto647. The bottom part (enhanced 15x) shows direct Atto647 excitation, QD-Atto647 transfer and the sequential QD-EYFP-Atto647 transfer. (B) Changes of the PL intensity at an excitation wavelength of 372 nm (white box in A) as a function of acceptor presence: DHLA-QD, QD/EYFP-A24 (**2**), and FRET systems **4a-d.**

The FRET efficiency data can be obtained from Figure 2.3.14A or following a study presented by Watrob and colleagues for a similar multicomponent FRET system.[98] According to this study, the efficiencies and Förster radii of different FRET pairs in the 3Ch-FRET system **4** can be derived from the results of the 2Ch-FRET subsystems (QD/EYFP, QD/Atto647 and EYFP/Atto647 pairs of conjugate **2**, **5** and **4***, Table 2.3.3), using the following formulae, which were generated from the kinetic calculations for the energy transfer rates in a three-chromophore system[98, 99]

$$E'_{QA} = \frac{E_{QA} - E_{QA} \times E_{QE}}{1 - E_{QA} \times E_{QE}} \qquad 2.3$$

$$E'_{QE} = \frac{E_{QE} - E_{QE} \times E_{QA}}{1 - E_{QE} \times E_{QA}} \qquad 2.4$$

where E'_{QA} and E'_{QE} are FRET efficiency of QD→Atto647 and QD→EYFP in the 3Ch-FRET system **4** (**4a-d**), and E_{QA}, E_{QE} are the corresponding ones of the 2Ch-FRET subsystems **2** and **4*** (**4a*-d***). The results of the efficiency calculations are listed in Table 2.3.4.

Table 2.3.4 Efficiency *E*, Förster radius R_0 for 3Ch-FRET systems **4a-d,** derived from the 2Ch-FRET subsystems (QD/EYFP, QD/Atto647 and EYFP/Atto647 pairs of conjugate **2**, **5** and **4***) and corresponding donor-acceptor separation distances *r*.

donor-acceptor pair	efficiency derived from independent system data [a]	Förster radius, R_0 (nm)	D-A distance r (nm)[b]
QD/EYFP in **4a**	0.64±0.02	3.63	5.11±0.06
QD/EYFP in **4b**	0.69±0.02	3.78	
QD/EYFP in **4c**	0.71±0.02	3.84	
QD/EYFP in **4d**	0.72±0.02	3.86	
QD/Atto647 in **4a**	0.11±0.02	2.55	5.61±0.09
QD/Atto647 in **4b**	0.037±0.007	2.56	6.84±0.20
QD/Atto647 in **4c**	0.008±0.001	2.56	8.86±0.05
QD/Atto647 in **4d**	0.001±0.001	2.63	12.9±1.1
EYFP/Atto647 in **4a**	0.78±0.02	4.83	3.91±0.08
EYFP/Atto647 in **4b**	0.43±0.02		5.06±0.07
EYFP/Atto647 in **4c**	0.23±0.03		5.91±0.16
EYFP/Atto647 in **4d**	0.072±0.02		7.40±0.44

[a] Based on equation 2.3 and 2.4; [b] *r* of all the FRET pairs, equal to the 2Ch-FRET subsystems due to maintained configurations;

The effect of the additional transfer channel is most readily visible on the example of system **4a**. While the QD→EYFP- and the QD→Atto647-transfer efficiencies were ~0.72 and ~0.31 in the systems displaying only a single transfer channel (**2** and **4a***, respectively), these values were reduced to ~0.64 and ~0.11 when both channels were open simultaneously, as calculated by equation 2.3 and 2.4. This decrease in FRET efficiency between QD and EYFP can be interpreted as the result of the competition between two pathways for FRET from the QD towards two different acceptors in the 3Ch-FRET system. In a complementary way, the decrease of the FRET efficiency from QD to Atto647 in conjugate **4a** compared with **4a*** (from ~0.31 to ~0.11) is due to the same competition between parallel energy transfer mechanisms. Consequently, the reduced efficiency of a transfer in the presence of a competitive acceptor can be specified by recalculating the characteristic Förster radii R_0, which are no longer constant, when exposing a donor species to two acceptors. This representation was chosen for the listing in Table 2.3.4.

Using the one-step FRET efficiency data E'_{QE}, E'_{QA} and E_{EA} of conjugate **4**, two kinds of overall FRET efficiencies for the 3Ch-FRET system can be derived based on the following equations system. [98, 99]

$$E_{QA}^{TOT} = E_{QA}^{SEQ'} + E'_{QA} = E'_{QE} \times E_{EA} + E'_{QA} \qquad 2.5$$

$$E_{Q\rightarrow EA}^{THEOR} = E'_{QE} + E'_{QA} \qquad 2.6$$

where E'_{QE}, E'_{QA} and E_{EA} are the corresponding one-step FRET efficiencies for the conjugates **4** (**4a-d**). Equation 2.5 demonstrates the total efficiency from the QD to Atto647 (the entire energy transferred to the Atto647 dye), which represents the parallel efficiency with one of the parts reflecting the sequential FRET efficiency. Experimentally, this efficiency can be measured by comparing the acceptor Atto647 emission gain at the presence and absence of the donor based on equation 1.5 from the data shown in Figure 2.3.14B. Equation 2.6 represents the theoretical combined efficiency from QD to both EYFP and Atto647 acceptors (the entire energy transferred away from the QD). Likewise, this efficiency can be obtained experimentally from the quenching of QD emission signal based on equation 1.4.

Table 2.3.5 Two types of overall FRET efficiency derived from independent FRET data and experimental estimate of two types of overall FRET efficiency obtained from spectral analysis of conjugates 3Ch-FRET systems **4a-d**.

3Ch-FRET system	calculated combined efficiency from QD ($E_{Q\rightarrow E,A}$) [a]	measured combined efficiency from QD ($E_{Q\rightarrow E,A}$) [b]	calculated total efficiency transferred to Atto647 ($E_{Q,E\rightarrow A}$) [c]	measured total efficiency transferred to Atto647 ($E_{Q,E\rightarrow A}$) [d]
4a	0.75±0.02	0.74±0.01	0.61±0.02	0.58±0.04
4b	0.73±0.02	0.72±0.02	0.33±0.02	0.30±0.06
4c	0.72±0.02	0.73±0.02	0.17±0.02	0.16±0.02
4d	0.72±0.02	0.74±0.03	0.053±0.02	0.048±0.02

[a] Calculated combined FRET efficiency of the energy transfer process from the QD to both EYFP and Atto647 using equation 2.6; [b] Measured combined efficiency from QD to both EYFP and Atto647, derived from equation 1.4; [c] Calculated total FRET efficiency of all energy transfer process to the Atto647, using equation 2.5; [d] Measured total efficiency of all energy transfer process to the Atto647, derived from equation 1.5.

The total efficiency from QD to Atto647 dye of ~0.61±0.02, 0.33±0.02, 0.17±0.02, 0.052±0.02 for conjugates **4a**, **4b**, **4c** and **4d**, respectively, agree well with the experimental data obtained from the Atto647 signal enhancement: ~0.58±0.04, 0.30±0.06, 0.16±0.02 and 0.048±0.02, respectively. The direct QD to Atto647 FRET (E_{QA}'=~0.11, 0.037, 0.008 and 0.001) contributes 18%, 10%, 4% and 0.3% of the total energy transferred from QD to Atto647. The majority of ~82%, 90%, 96% and 99.7% is contributed from the QD→EYFP→Atto647 FRET process. The efficiencies of combined energy transferred away from the QD to both EYFP and Atto647 were also calculated following equation 2.5. Good agreement with the values obtained experimentally from the QD quenching in the four constructs (**4a-d**) was observed (errors of less than ~3%, see Table 2.3.5). These small errors substantiate the assumption raised earlier that in all 3Ch-FRET systems QD/EYFP/Atto647 (**4a-d**) the spatial deviations of the chromophore orientations and distances are very small compared to those within 2Ch-

FRET subsystems **2**, **4*** and **5**. Both the theoretically estimated and experimentally determined overall efficiencies calculated from the results shown in Figure 2.3.14B for the 3Ch-FRET systems **4a-d** are listed in Table 2.3.5.

2.3.2.4 FRET parameter of the 3Ch-FRET system derived from the temporal evolution of the emission

To further support the FRET efficiencies obtained from the time integrated experiments, the luminescence of the four multi-FRET samples **4a-4d** was recorded time-resolved and the decay curves were compared to the results of a numerical simulation as demonstrated in Figure 2.3.15.[142] The evolution of the combined luminescence of the QD and the EYFP was accessible by binning the wavelength range from 521 nm to 547 nm of the temporally and spectrally dispersed luminescence signal to obtain a time vs. intensity plot. Likewise, the decay of the Atto647 dye was accessible by extraction of the PL signal between 653 nm and 679 nm. The model calculation, which is an extension of the routines used to simulate the behavior in the QD/EYFP system explained above, takes into account the radiative and non-radiative recombination channels of the QD, the EYFP and the Atto647 dye. Crosslinking channels are the transfer from the QD to the EYFP, the direct QD→Atto647 transfer and the EYFP→Atto647 channel. Again the population of each subspecies was calculated in an iterative way with a simulated temporal resolution of 1 ps (details of the simulation strategy see appendix 7.2). The radiative recombination rates were extracted from fluorescence lifetime measurements of the QDs, the EYFP and the Atto647 dye, and their respective quantum yields. The transfer transition rates were then adjusted to match the efficiencies derived from time integrated measurements. The result of such a simulation was compared to the measured PL of the system in Figure 2.3.15. The parameters used to obtain a consistent agreement are for the QD were: QY=0.066, k_{rad}=0.019 ns^{-1}; EYFP QY=0.62, k_{rad}=0.2 ns^{-1} and for the dye Atto647 k_{rad}=0.05 ns^{-1} and $k_{QD\rightarrow EYFP}$ = 0.053 ns^{-1}. The varying transfer rates in the four differently spaced multi-FRET systems are $k_{EYFP\rightarrow Atto}$ = 1.15 ns^{-1}, 0.245 ns^{-1}, 0.10 ns^{-1}, 0.031 ns^{-1}; and $k_{QD\rightarrow Atto}$ = 0.0095 ns^{-1}, 0.0028 ns^{-1}, 0.0006 ns^{-1}, 0.00008 ns^{-1} for samples **4a-d**, respectively. It is striking, that at the closest proximity of the Atto647 dye to the EYFP (**4a**), when the energy was transferred to the dye most efficiently, the formation of the rise in the EYFP PL intensity was prevented, while the Atto647 displays a gain in emission (Figure 2.3.15). At larger distances, the characteristic behaviour of the QD/EYFP system was recovered (also Figure 2.3.10), while the Atto647 emission was returning to the mono-exponential behavior, which was also

observed when the dye was not subject to energy transfer. The obtained radiative decay rates k_{rad} and energy transfer rates k derived from the time-resolved emission of the four 3Ch-FRET systems **4a-d** were summarized in Table 2.3.6.

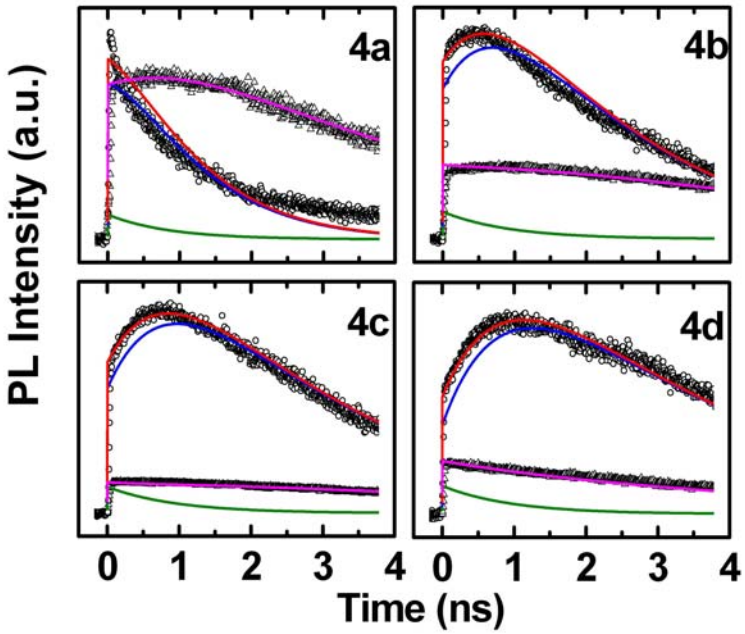

Figure 2.3.15 The temporal evolution of the spectrally resolved luminescence signal of the four FRET systems **4a-d** and their simulated behavior. The data points show the intensity recorded in the wavelength range of QD and EYFP emission (circles) and at the Atto647 emission wavelength (triangles). The simulated curves display the dynamics of QD (green), EYFP (blue), the sum of QD and EYFP (red), and Atto647 (magenta).

According to the data listed in Table 2.3.6, the internal transfer from QD to EYFP in the four conjugates **4a-d** ranged from E~0.64 to E~0.72, indicating that the QD/EYFP-A24 conjugate **2** indeed acts as a combined donor complex. In addition to this high transfer efficiency, this donor complex benefits from the unique advantages of QD and fluorescent proteins and also overcomes the limitations of the individual components. The QD/EYFP-A24 conjugate with a large absorption cross section (from QD) and a high quantum yield (from EYFP) can be excited at a much broader wavelength region and a more efficient transfer can be achieved. The QD also serves as a nano-scaffolding to assemble multiple EYFP-A24 species into a single complex, which to some extent integrates energy transfer emitters. The oligonucleotide attached to the EYFP provides a functional coupling bridge for different acceptors, thus enabling the precise control over donor-acceptor separation distances. The donor emission center of the new complex is shifted from the QD center to the EYFP center and overcomes

the inherent large size limitation of QDs, which also helps to achieve a long-range FRET. As an example, a donor-acceptor separation distance of ~8.86 nm was achieved with a decent total FRET efficiency of ~0.17 in conjugate **4c**, compared to a separation distance of only ~5.91 nm in the respective conjugate **5c**, comprising only EYFP and Atto647 (Tables 2.3.4 and 2.3.5). A maximum separation distance of ~12.9 nm could be reached the case of the 3Ch-FRET systems, which can hardly be achieved by a simple, two-chromophore FRET system.

Table 2.3.6 Radiative decay rates k_{rad} and energy transfer rates k derived from the time-resolved emission for the four FRET systems **4a**, **4b**, **4c** and **4d** as parts of the 3Ch-FRET system QD-EYFP-Atto647.

System	$k_{QD,rad}$	$k_{EYFP,rad}$	$k_{QD\rightarrow EYFP}$	$k_{Atto647,rad}$	$k_{QD\rightarrow Atto647}$	$k_{EYFP\rightarrow Atto647}$
2	0.019 ns^{-1}	0.2 ns^{-1}	0.053 ns^{-1}	-	-	-
4a	—″—	—″—	—″—	0.05 ns^{-1}	0.0095 ns^{-1}	1.15 ns^{-1}
4b	—″—	—″—	—″—	—″—	0.0028 ns^{-1}	0.245 ns^{-1}
4c	—″—	—″—	—″—	—″—	0.0006 ns^{-1}	0.10 ns^{-1}
4d	—″—	—″—	—″—	—″—	0.00008 ns^{-1}	0.031 ns^{-1}

2.3.2.5 Structural arrangement of components in the 3Ch-FRET system

While the distinct relation between transfer efficiency and distance in a single Förster-type energy transfer allows the calculation of the separations between the donor and the acceptor, the simultaneous presence of multiple FRET mechanisms allowed for insights into the spatial arrangement of the system's components. This is due to the fact that three distances between three points in space define their respective coordinates.

Picking up the aforementioned picture of the QD being attached to the "barrel bottom" of the EYFP, and taking into account that the DNA is attached to the same region of the C terminus of the protein, one can assume that the protein is being tilted to provide space for the flexible sulfo-SMCC linkage to the DNA. Knowledge of the transfer efficiency in the case of sample **4d**, which translates into a distance of 12.9 nm, strongly suggests that the flexible EYFP/DNA link is bent in a way that allows the DNA and the attached Atto647 dye to point away from the QD, because this is the only configuration that allows for such a large QD/Atto647 separation, while maintaining the QD/EYFP and the EYFP/Atto647 distances.

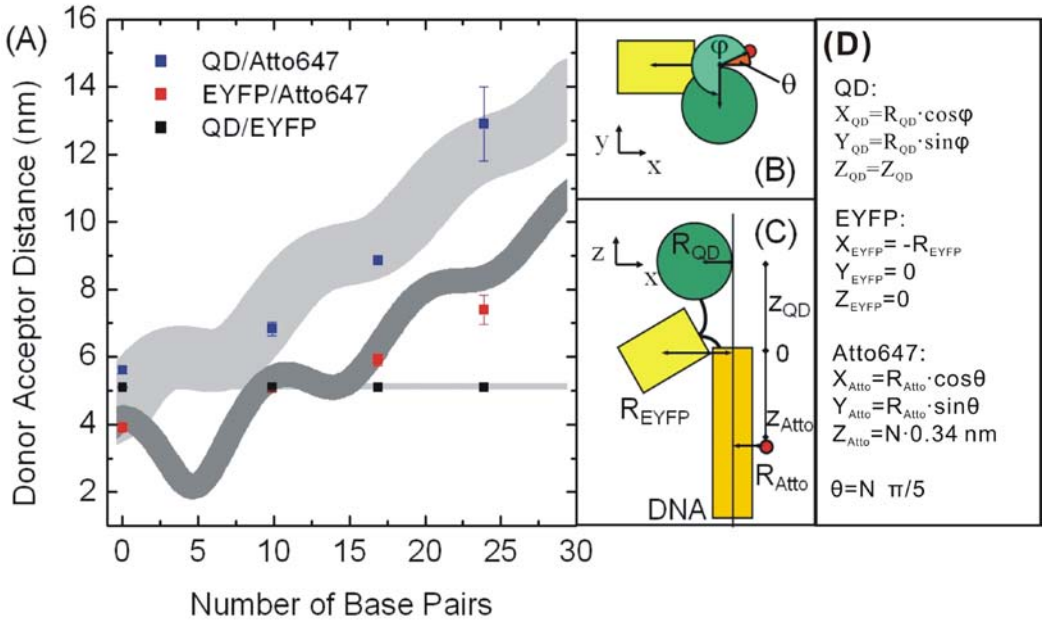

Figure 2.3.16 (A) The donor/acceptor distances between QD, EYFP, and Atto647 derived from the measured transfer efficiencies. The gray regions indicate the results of according distance calculations with the parameters R_{QD}=2.5 nm, R_{EYFP}=2.8 nm, R_{Atto}=1.4 nm, z_{QD}= -3.5 nm, φ=270°, based on a least square fit to the data. The DNA helicity furthermore dictates z_{Atto}= N×0.34 nm and θ=N×36° with N being the number of base pairs. (B) The cylindrical coordinate system, used to describe the positions of the multi-FRET constituents seen from top. The z-axis corresponds to the central DNA axis. The angular coordinate for the QD is φ and for the Atto647 dye θ. (C) Side view of the same coordinate system. The radial coordinates R_{QD}, R_{EYFP}, and R_{Atto} represent the distances from the z-axis. For simplicity only one of the 14 EYFP/Atto647 conjugates is shown. (D) Cartesian coordinate positions of QD, EYFP and Atto647 in the geometric model B and C.

The EYFP/QD subsystem displays an energy transfer efficiency that can be probed with high precision, thus allowing for a realistic estimation of a distance of 5.1 nm. The DNA helix of the EYFP/Atto647 subsystem provides well-defined values for the distance along, and the angle around the DNA axis. However, the aliphatic linker molecules in between EYFP and DNA or Atto647, respectively, introduce uncertainties because they are rather long and flexible. The number of possible configurations and orientations is increased even further, since the EYFP/Atto647 conjugates are likely bound flexibly to the QD's surface. However, one can expect that the high loading of the QD surface (N=~14) reduces the range of possible configurations. To describe the structural properties of this multi-FRET system, a geometric model of the 3Ch-FRET systems was therefore proposed, which is

based on the helicity of the DNA,[93, 154] the rough knowledge of size and shape of the constituents and linkers, and importantly on the measured transfer efficiencies to describe the structural properties of this multi-FRET system. Because the persistence length of DNA is about 50 nm, it was estimated the short dsDNA as a rigid linker, although the aliphatic spacers in between DNA and both EYFP and QD should be considered flexible.

Kukolka et al. had previously established that DNA maintains its double helical B-configuration in the EYFP-A24 conjugates,[93] and thus one can consider the DNA helix as a cylinder with the center of the top lid as the origin of a cylindrical coordinate system. The positions of the FRET constituents are being described by the parameters sketched in Figure 2.3.16B and C. Starting at the origin, the EYFP position can be defined to be at a distance of R_{EYFP} along the negative x-axis. The Atto647 position in the case of 0 BP between the two is fixed at a distance $R_{Atto647}$ in positive x direction. With growing number of base pairs between these two chromophores, the Atto647 orbits the central DNA axis with an angle $\theta = N \times \pi/5$ and simultaneously descends along the z-axis as $z_{Atto} = N \times 0.34$ nm, with N indicating the number of base pairs. This assumes that two base pairs are separated by 0.34 nm, and that the DNA completes one revolution after the 10th base pair. The position of the QD can be represented by a respective set of coordinates z_{QD}, θ, and R_{QD}. Simple geometric considerations were used to calculate the distances between the three multi-FRET constituents in order to compare them to those derived from the measured FRET efficiencies. The distances of each two of the FRET constituents can be acquired by equation 2.7-2.9.

$$Dist_{QD/EYFP} = \sqrt{(R_{QD} \times \cos\varphi + R_{EYFP})^2 + (R_{QD} \times \sin\varphi)^2 + (Z_{QD})^2} \qquad 2.7$$

$$Dist_{QD/Atto} = \sqrt{(R_{QD} \times \cos\varphi - R_{Atto} \times \cos\theta)^2 + (R_{QD} \times \sin\varphi - R_{Atto} \times \sin\theta)^2 + (Z_{QD} - N \times 0.34)^2} \qquad 2.8$$

$$Dist_{EYFP/Atto} = \sqrt{(R_{Atto} \times \cos\theta + R_{EYFP})^2 + (R_{Atto} \times \sin\theta)^2 + (N \times 0.34)^2} \qquad 2.9$$

where N is the number of base pair, 0-24 and is an independent variable. Other parameters can be deduced as illustrated in Figure 2.3.16D. The outcome of this "spectroscopic triangulation" is shown in Figure 2.3.16A. Taking into account the uncertainties mentioned earlier to display the calculated distances as a broad band reflecting estimated errors of 1.3 nm, 0.5 nm, and 0.1 nm in the calculation of the QD/Atto647, the EYFP/Atto647, and the QD/EYFP distances, respectively. The parameters used were: R_{QD}=2.5 nm, R_{EYFP}=2.8 nm, $R_{Atto647}$=1.4 nm, z_{QD}= -3.5 nm, φ=270°, and are based on a least square fit to the data. Indeed, this simulation supported our hypothesis that the proteins are tilted on the QD surface to allow the DNA to place the Atto647 dye at a maximum possible distance from the QD.

This assumption is further corroborated by the fact that the DNA only marginally changes the effective size of the EYFP, derived from of the maximum number of proteins on the QD surface, which was demonstrated in the analysis of the QD/EYFP 2Ch-FRET subsystem (also Figure 2.3.6B).

2.3.2.6 DNA double helix regulated FRET

In order to further verify the cylinder model of the 3Ch-FRET systems, in addition to 0, 10th, 17th, and 24th base pair (bp) position of the cA24 oligonucleotides (Figure 2.3.7B), Atto647 dyes were attached on the 3rd, 5th and 7th bp of cA24 to form three different donor/acceptor distances FRET systems. Since the Atto647-fluorophore is attached through a linker to the thymine base, the 3rd, 5th and 7th base of cA24 were first exchanged to thymine bases instead of the other bases within the cA24 sequence. The modified cA24-Atto647 conjugates are termed as **3e**, **3f** and **3g** for the 3rd, 5th and 7th Atto647 modified oligonucleotides, respectively. In the complementary oligonucleotides A24 bases were also modified at the corresponding positions to adenine and covalently attached to EYFP and termed as **1e**, **1f** and **1g**, respectively (The detailed sequences are listed in experimental section, Table 5.2.). The EYFP/Atto647 2Ch-FRET conjugates were formed by hybridizing **1e**, **1f** and **1g** with **3e**, **3f** and **3g**, respectively, and termed as **5e**, **5f** and **5g**, respectively. The FRET efficiency between EYFP and Atto647 for the three conjugates **5e**, **5f** and **5g** were obtained based on the quenching of EYFP PL by similar titration experiments as **5a-5d** systems and then the donor/acceptor separation distances were calculated based on equation 1.5-1.7 and the Förster radius of EYFP/Atto647 pair (Table 2.3.3). To investigate QD/Atto647 2Ch-FRET systems (termed as **4e***, **4f*** and **4g***), the EYFP-DNA conjugates **5e**, **5f** and **5g** were photobleached via the same procedure described earlier, bound to the QD surface and then hybridized with **3e**, **3f** and **3g**, respectively. The efficiency data for QD/Atto647 conjugates **4e***, **4f*** and **4g*** were obtained based on the enhancement of Atto647 PL (equation 1.4) and the QD/Atto647 separation distances were calculated accordingly. All the efficiency and donor/acceptor separation distances data are listed in Table 2.3.7.

If all the separation distances data are put together to fit the cylinder model presented earlier (Figure 2.3.16) and make a new set of the parameters R_{QD}, R_{EYFP}, $R_{Atto647}$, z_{QD} and φ, the same values of these parameters were achieved based on the least square fit and the boundary conditions, which are limited by the chemical linkage and sizes of the fluorophores. The results are plotted in Figure 2.3.17. As depicted in Figure 2.3.17A, most of the separation distances are within the range of theoretical estimation except the case of 5th bp Atto647-cA24 conjugate **4f** (**5f** or **4f***). In the presented geometric

model, the 5th bp position is where the Atto647 molecule and the EYFP are the first time on the same side and the distance between them is the smallest compared with all the other positions. The theoretical estimation for the EYFP/Atto647 separation distance is ~2.2 nm and the corresponding theoretical FRET efficiency between EYFP and Atto647 is ~0.991. This is an ideal state with the assumption that there is no mechanical or electrostatic interaction between the fluorescent protein and Atto647 dye and with pure geometric consideration. Actually, there will be repulsion between EYFP and Atto647 molecule and the repulsion reaches maximum when the distance between them is minimum, that is, 5th bp position. Additionally, the flexible sulfo-SMCC linkage between EYFP and DNA allowed the free rotation of the DNA cylinder. This repulsion between EYFP and Atto647 will eventually enlarge their distance or rotate the DNA cyliner to keep the mechanical or electrostatic balance. As a result, the separation distance between QD and Atto647 enlarges accordingly. Similarly, this effect influences the separation distances of EYFP/Atto647 when the Atto647 is attached to smaller bp and close the side of EYFP (i.e. 3rd-8th bp). As indicated in Figure 2.3.17A, the EYFP/Atto647 separation distances of the 3rd and 7th cases are also a little larger than the theoretical estimates, which confirmed the repulsion between the protein and dye molecule.

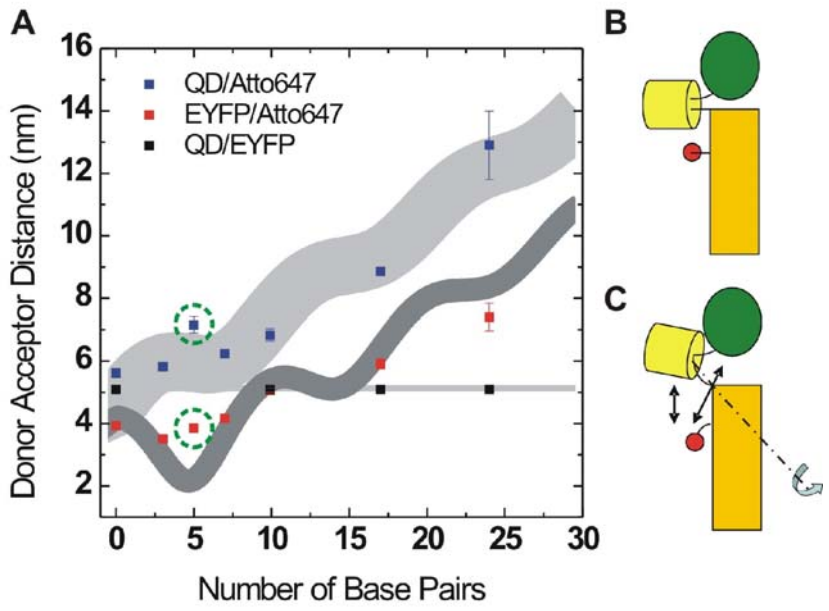

Figure 2.3.17 (A) The donor/acceptor distances between QD, EYFP, and Atto647 derived from the measured transfer efficiencies for all conjugates **5a-g**, **4a*-g***. The gray regions indicate the results of according distance calculations with the parameters R_{QD}=2.5 nm, R_{EYFP}=2.8 nm, R_{Atto}=1.4 nm, z_{QD}= -3.5 nm, φ=270°, based on a least square fit to the data. The DNA helicity furthermore dictates z_{Atto}= N×0.34 nm and θ=N×36° with N being the number of base pairs. (B) Schematic representation of theoretical state of the 5th bp Atto647-DNA conjugate

4f, in which the separation distances between EYFP and Atto647, QD and Atto647 are minima. (C) Schematic representation of the actual state of the 5th bp Atto647-DNA conjugate **4f** based on the experiment data (green dashed circles in A), which the separation distances are larger than estimates due to repulsion. Basically, the linkage between EYFP and DNA cylinder are freely rotatable.

Table 2.3.7 Measured efficiencies *E*, donor-acceptor distances *r* and structurally estimated donor-acceptor distance for the three 2Ch-FRET subsystems **5a-g** and **4a*-g***.

donor-acceptor pair	efficiency	D-A distance, r from E (nm)[a]	D-A distance, r from structural estimate (nm)
EYFP/Atto647 in **5a**[b]	0.78±0.02	3.93±0.08	4.2
EYFP/Atto647 in **5e**	0.87±0.01	3.51±0.05	2.9
EYFP/Atto647 in **5f**	0.80±0.003	3.85±0.01	2.2
EYFP/Atto647 in **5g**	0.71±0.01	4.17±0.03	3.6
EYFP/Atto647 in **5b**	0.43±0.02	5.06±0.07	5.4
EYFP/Atto647 in **5c**	0.23±0.03	5.91±0.16	6.4
EYFP/Atto647 in **5d**	0.072±0.02	7.40±0.44	8.4
QD/Atto647 in **4a***	0.31±0.03[c]	5.62±0.11	4.5
QD/Atto647 in **4e***	0.26±0.03	5.82±0.14	5.9
QD/Atto647 in **4f***	0.094±0.02	7.16±0.25	5.9
QD/Atto647 in **4g***	0.19±0.02	6.24±0.10	6.0
QD/Atto647 in **4b***	0.12±0.02	6.84±0.20	7.4
QD/Atto647 in **4c***	0.028±0.001	8.86±0.05	9.3
QD/Atto647 in **4d***	0.003±0.002	12.9±1.10	12.1

[a] Estimated using $r=R_0*(N(1-E)/E)^{1/6}$, N=14 for the QD-Atto647 and QD/EYFP pair and N=1 for the EYFP/Atto647 pair; [c] The **a**, **e**, **f**, **g**, **b**, **c**, **d** represent the Atto647-dye attaching positions from 0, 3rd, 5th, 7th, 10th, 17th to 24th base pair of the oligonucleotides, respectively; [c] The efficiencies of four different QD/Atto647 pairs were obtained from acceptor PL gain
* bleached EYFP-A24 (**1***) was used for assembly

2.3.3 Summary

In this work the detailed analysis of a novel supramolecular energy transfer system was described, which comprised of inorganic luminescent QD, the fluorescent protein EYFP and DNA oligonucleotides labeled with the organic dye Atto647. The QDs function both as the nano-scaffold to facilitate self-assembly of the system and as the primary donor for energy transfer to the fluorescent proteins. This binary system essentially works as a novel donor for efficient long-range energy transfer to the Atto647, the latter of which is positioned at distinct distances from a donor by means of the double helical DNA spacer. Spatial configurations such as relative orientations, donor-acceptor separation distances, Förster radii and transfer efficiencies of each of the three implemented QD/EYFP,

QD/Atto647 and EYFP/Atto647 2Ch-FRET pairs were elucidated by both theoretical and experimental approaches and found to be consistent. Fluorescent lifetime measurements of QD/EYFP and QD/EYFP/Atto647 systems provided additional proof of the FRET processes occurring between the three chromophores. As a novel approach to investigate interactions between luminescent QD and fluorescent proteins, photobleaching was here employed to unambiguously measure the PL enhancement caused by the adsorption of proteins to the QD and to allow one to take into account this change in QD's spectral properties to elucidate transfer processes.

It was observed that in the 3Ch-FRET system, a dominant QD→EYFP→Atto647 FRET pathway largely overrules the direct QD→Atto647 FRET path. This is caused by the fact that in the 3Ch-FRET system, the 2Ch-FRET subsystem QD/EYFP, comprised of QDs containing up to 14 molecules of EYFP, showed highest FRET efficiencies, ranging from 64% to 72%. Thus, the 2Ch-FRET QD/EYFP subsystem functions as a powerful donor which combines the intrinsic advantages of QDs (large and spectrally broad absorption cross section) with the high quantum yields of EYFP, thereby enabling long-distance FRET processes over 9-13 nm with efficiencies of 17-5%, respectively. The efficiency values are significantly higher than those of the direct QD-to-Atto647 transfer (0.8-0.1%, respectively) thereby impressively demonstrating the power of the self-assembled QD/EYFP donor. These results, in particular, suggest that supramolecular donors assembled from QDs and fluorescent proteins may enable for long-range FRET detection in a variety of applications, such as FRET-based high-throughput screening assay or *in vivo* observation of spatial and temporal regulation of signaling processes.

2.4 PEG2000-phospholipids stabilized QDs for cellular imaging

In the last few years, luminescent QDs have been successfully used in immunofluorescence labeling of living cells and tissues,[13, 14, 52] which represents one of the most attractive and progressive application for QDs. Numerous reports have shown that QD labeling allows extended visualization of cells or living tissues under continuous illumination as well as multiplex color imaging, demonstrating the unique advantages offered by these nanocrystals.[5, 63, 71, 73, 74, 118, 119, 155, 156] Despite these advantages, there are several key requirements to be taken into account to apply luminescent QDs for intracellular imaging: (i) *in vivo* photo- and chemical-stability ready for a long-term imaging under some harsh cellular conditions; (ii) availability of necessary functionalities for the recognition, localization, assembly of conjugated cellular components or proteins in living cells; (iii) effective and safe delivery

strategies. In some cellular studies, hours even days of monitoring are needed, which requires QDs to be resistant against bleaching and posses increased stability in variable environments. Most of the QDs bioconjugates must be delivered into cells since they can not diffuse passively through the lipid bilayer of cell membranes due to the size constrains. Several methods have been used to enable their transport in previous reports: endocytosis;[54, 119, 157] coupling of the QD to cell penetrating peptides;[73, 158-160] microinjection;[74, 158] electroporation[158, 161] or DNA transfection reagents.[158]

In the search for new and effective methods of QD intracellular transport aimed at using them for Rab7 targeting study. Rab-GTPases, members of the Ras superfamily of small GTPases, play an important role in eukaryotic vesicular transport. They regulate vesicle budding, transport and tethering through interactions of their activated GTP-bound form with specific effectors. Post-translational modification of one or two N-terminal cysteines with geranylgeranylgroups allows their strong but reversible binding to lipid membranes. Interestingly, each Rab-GTPase (more than 60 Rab-proteins were identified in mammals) is targeted to specific organelles.[162-166]

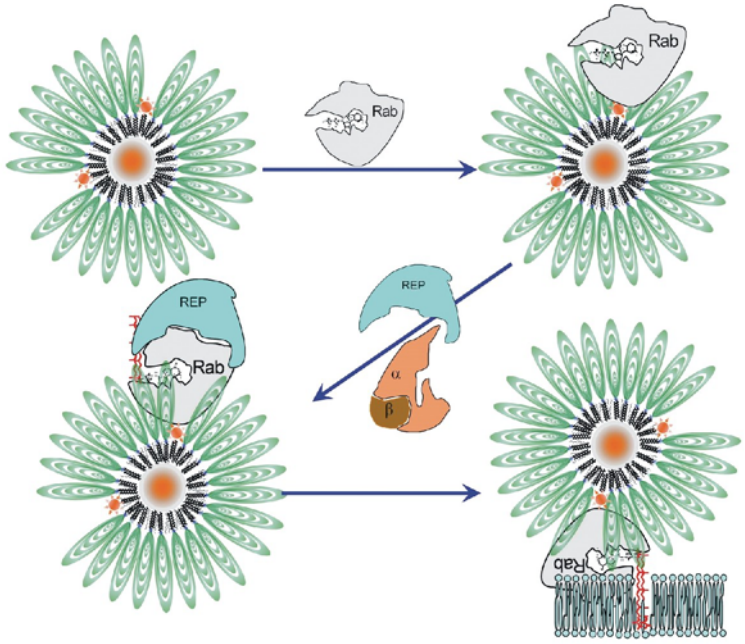

Figure 2.4.1 Scheme of prenylation procedure for a PEG2000-QD/Rab7 conjugate. The Rab7 protein was attached to a functionalized QD and the prenylation reaction was carried out in the presence of Rab escort protein (Rep1), Rab geranylgeranyl transferase (RGGT) and Geranylgeranyl pyrophosphate (GGpp). At the last stage, the prenylated Rab7/QD conjugate was delivered to the membrane of organelles by the help of Rep1.

The aim of the project was to investigate the possibility to deliver quantum dots inside living cells and target them to specific organelles *via* their functionalization with Rab7, one of the aforementioned Rab-GTPases. The *in vitro* and *in vivo* stability of QDs with various surface modifications were first investigated and compared. PEG2000 phospholipid micelle stabilized QDs (termed as PEG2000-QDs) employed in this work possess the best *in vitro* and *in vivo* stability among all the samples. In addition, a preliminary work on preparation of QD-Rab7 conjugates for Rab7 prenylation procedure and intracellular localization study was carried out.

2.4.1 *In vitro* and *in vivo* stability of PEG2000-phospholipid stabilized QDs

QDs show exceptional photostability and the resistance to metabolic degradation. It is reported that QDs do not photobleach even after 14 hrs illumination with a 50-mW light while most of the organic dyes photobleach completely in 20~40 mins.[157] These properties allow QD to be used not only for imaging QD-labeled proteins over long periods[119, 155], but also for imaging of the growth and development of organisms for long periods from hours to days.[74, 157] However, all these applications can be achieved only when the QDs are highly stable in the aqueous environments especially in cellular conditions. QDs are inherently hydrophobic in nature and thus different strategies have been applied to make them water-soluble. During this process, the stability and quantum yield of the QDs is decreased due to the sensitivity of QDs and their PL to environmental factors such as pH, salt concentration and oxidation.[120, 167, 168] Furthermore, the colloidal nature of QDs in aqueous environment makes them susceptible to irreversible aggregation, which is effected by the changes in pH, salt concentration, storage temperature or surroundings. Since the environmental conditions in living cells are varied and some of them are rigorous, a reliable surface modification for QDs is essential. As discussed in the earlier chapters, different solubilization and functionalization strategies have been used in this thesis, such as DHLA-coating, PEG (or non-PEG) phospholipid coating for QD CdSe/ZnS. The *in vitro* and *in vivo* stability will be compared to preliminarily evaluate the QDs for cellular imaging.

Figure 2.4.2 shows the comparison experiments on the PL maintenance for the exemplary 586 nm-emitting QDs with various surface coating (DHLA, non-PEG-PLs, PEG350-PLs, PEG2000-PLs) and in various aqueous conditions (water, PBS, cell lysate). Briefly, QDs samples (termed as DHLA-QDs, PLs-QDs, PEG350-QDs, PEG2000-QDs, respectively) with different coating were dispersed in three classic aqueous solution systems, ddH_2O, PBS (pH 7.3, 150 mM NaCl) and the human epithelia A431 cells lysate. Subsequently the samples were illuminated with 350 nm light for 8 hrs. The PL of each

sample were recorded and compared. The PEG2000-QDs maintain the PL after 8 hrs in all the buffer systems (Figure 2.4.2A), suggesting the comprehensive coating of QDs. The PL of PEG2000-QDs increased ~13% in cell lysate. The reason for this was not further investigated, however, one may speculate that the absorption of some proteins on the QDs surface increases the surface passivation and thus increase the fluorescence.

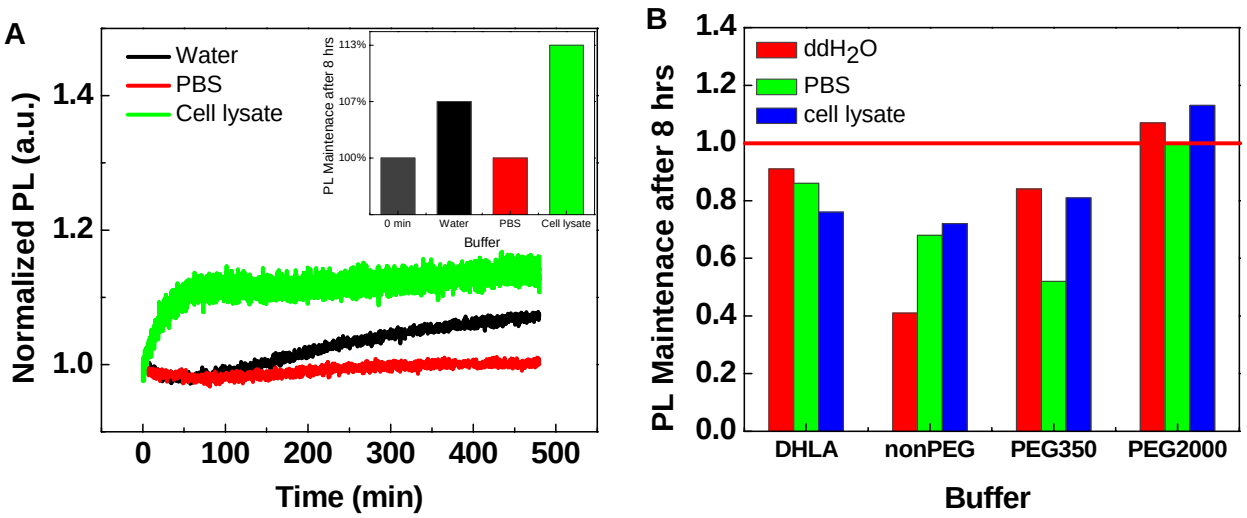

Figure 2.4.2 Photoluminescence stability of 586 nm-emitting DHLA-, PLs-, PEG350- and PEG2000-QDs in ddH_2O, PBS and cells lysate solution. (A) Photoluminescence stability of PEG2000-QDs in ddH_2O, PBS and cells lysate as the function of time of 8 hrs. The inset shows the PL comparison before and after 8 hrs illumination with 350 nm light for PEG2000-QDs in the three aqueous solutions. (B) PL comparison for four different coating QDs in three solutions. The PL was recorded on a fluorescent spectroscope for each sample under illumination of 350 nm light for 8 hrs. Note that the PL intensity of each sample was normalized against initial intensity.

As shown in Figure 2.4.2B, nearly in all samples, the QDs maintain over 50% of their initial photoluminescence after 8 hrs, which indicates that these QDs are relatively stable in the three buffer systems. It was reported that thicker coating leads to improved stability in aqueous media.[13, 14] This was confirmed by the investigations shown in Figure 2.4.2. The PEG2000-QDs exhibited the best *in vitro* stability among all the testing samples and in all aqueous solutions, whereas other QD samples with thinner coating are of less stability either in water or in ionic buffer. The hydrophilic poly (ethylene glycol) chain provides not only the solubilization but also increase the biocompatibility of the nanocrystals.[74] The cell lysate dispersion is the solution with high proteins concentration and is was

used as an model environment to mimic the cellular conditions. The stability of QDs in the lysate can in certain extent reflect the intracellular situation.

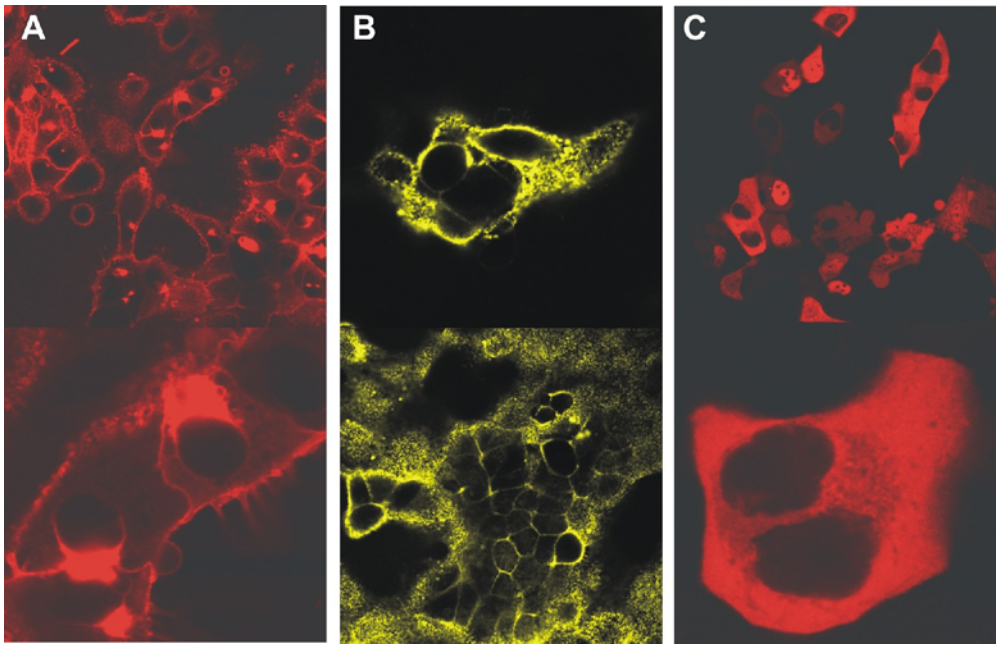

Figure 2.4.3 Intracellular stability test of three different coating QDs observed by a confocal laser scanning microscopy. (A) DHLA-QDs were microinjected into A431 cells. The images were recorded 30 min after microinjection. The DHLA-QDs aggregated at where they were injected. (B) PEG350-QDs aggregated 40 min after microinjection. (C) PEG2000-QDs were well dispersed in A431 cells and no aggregations were observed after microinjection.

The stability of different coating QDs have also been tested in living cells. The PEG2000-QDs are of hydrodynamic diameter (HD) of ~12-20 nm in this work, which are difficult to get into cytoplasm by endocytosis or other active delivery strategies. The QDs were therefore microinjected into A431 cells and monitored by a confocal laser scanning microscope (Figure 2.4.3 and Figure 2.4.4). The goal of this study was to preliminarily evaluate the intracellular stability of different QDs. Therefore, the QDs were not functionalized with any proteins and simply introduced into the cytoplasm. Figure 2.4.3 shows the *in vivo* stability comparison of DHLA-, PEG350-, PEG2000-QDs in A431 cells around 30 min after microinjection.

DHLA-QDs were developed a few years ago and had many applications for *in vitro* studies as FRET-based sensing due to their reduced hydrodynamic diameter (HD).[17, 61] As shown in Figure 2.4.2B, DHLA-QDs maintain 76-91% PL in the above mentioned three solutions, indicating the high *in vitro* stability. However, these QDs have not been widely used for *in vivo* imaging because the thin DHLA

layer makes them highly sensitive to pH and salt. The DHLA-QDs tended to aggregate when the pH decrease below ~6-7 due to the protonation of DHLA.[56, 63, 66] As shown in Figure 2.4.3A, the DHLA-QDs aggregate at where they were loaded and they were difficult to disperse into the cytoplasm upon microinjection, which indicate that these QDs are not suitable for *in vivo* imaging at all.

In the case of PEG350-QDs, they could be introduced into the whole cytoplasm by injection and distributed evenly, but aggregates were observed after ~10-30 min. non-PEG PLs-QDs were also tried to introduce to A431 cells by microinjection in this work. However, the particles aggregated on the needle tips and failed to get into cells. The failure of introduction of PLs- and PEG-QDs into the living cells suggested that non-PEG or short PEG phospholipid stabilized QDs were not suitable for the cellular imaging study in this thesis. Therefore, only PEG2000-QDs were carried out for the further investigation for cellular imaging.

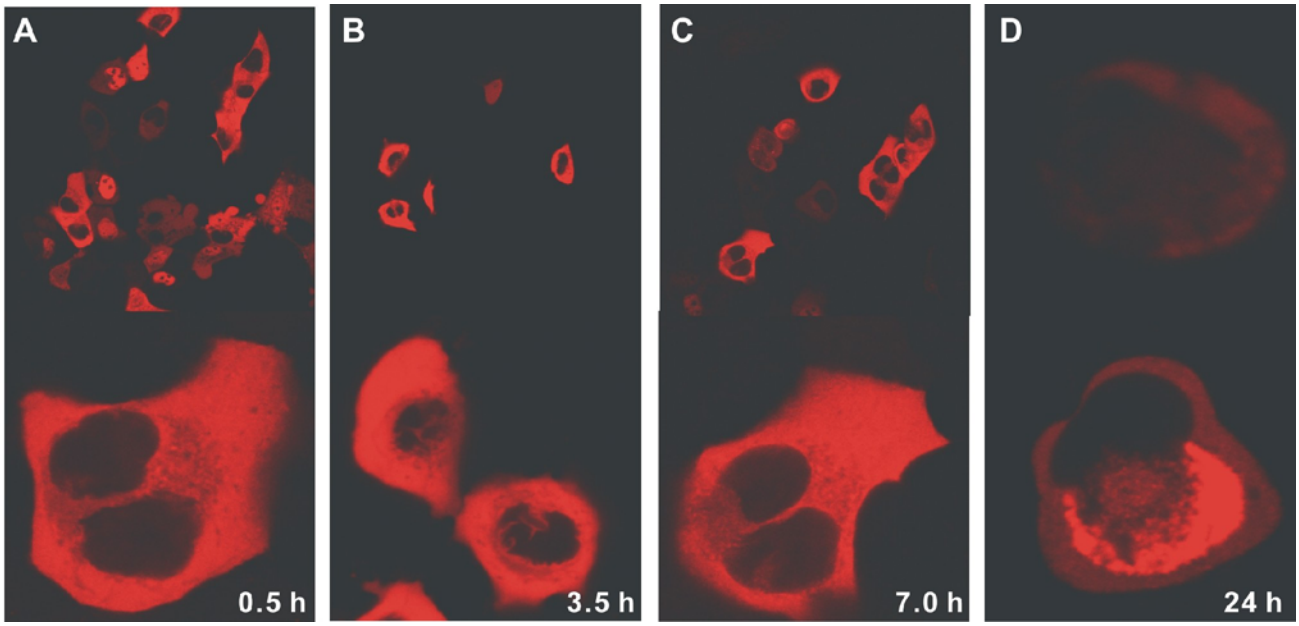

Figure 2.4.4 Intracellular stability over time of microinjected PEG2000-QDs in A431 cells. The PL signal of QD emission was recorded by a confocal laser scanning microscope at (A) 0.5 hrs, (B) 3.5 hrs, (C) 7 hrs and (D) 24 hrs. The QDs were found to be well dispersed in the cytoplasm and stable for at least 7 hrs after injection. The cells seem to be healthy and with normal shapes during the process except after ~24 hrs culture.

The intracellular stability of PEG2000-QDs was further investigated as a function of time (Figure 2.4.4). The QDs were microinjected into living A431 cells and the PL of cells was monitored by the confocal microscope for 24 hrs when the cells seemed sick and died. It is obvious that at least for 7 hrs, the cells were in a health state and the PL of QDs was still high enough for the tracking and no

microscopic aggregations were observed. The stability meets the requirement of targeting the Rab7 in living cells, which normally happens after several mins to 2-3 hrs.[162, 166] This result suggested that the PEG2000-QDs were possibly applicable for tracking the prenylation procedure of Rab7. It was also shown in the figures that PEG2000-QDs were not able to diffuse through the nuclear pores due to the large size. The next step was preparation of QDs/Rab7 conjugates and microinjection into living cells.

2.4.2 Rab7-QDs hybrids

To validate the application of QD in monitoring cellular events, QD conjugated Rab7 GTPase were investigated in the present study. Rab GTPases are the key regulators of membrane trafficking. Posttraslational modification of Rab GTPases with (usually) two geranylgeranyl groups at the C-terminal cysteines enables them to associate membranes of their target organelles. This modification, known as prenylation, is catalyzed by Rab geranylgeranyltransferse (RabGGTase) and requires an additional factor Rab escort protein (REP). Hence it was necessary to determine whether recombinant Rab proteins can be processed by the endogenous Rab prenylation machinery after microinjection into the human epithelial A431 cells. The correctly intracellular localisation of Rab proteins is a suitable assay for Rab function. The fluorescent proteins (EGFP) and immunogold labeling have been used to follow Rab7 intracellular localisation in living cells by fluorescence or electronic microscopy.[162, 166] Nevertheless, The molecular machinery behind lysosomes biogenesis and the maintenance of the perinuclear aggreagate of late endocytic structures is still not well understood.[162] Luminescent QDs are excellent fluorescent labelling alternatives with enhanced quantum yield and anti-photobleaching properties, which have been widely used for such as immunofluorescence labelling, immunostaining of membrane-bound proteins or other organelles in cells.[13] However, the applications of QDs/protein hybrids for tracking posttranslational modification procedure have not been reported. The long-term stability and possible single-particle tracking properties of PEG2000-QDs would allow the further investigation the roles of Rab GTPases in vesicular transport. Before the QDs-Rab7 conjugates were used, recombinantly expressed fusion protein YFP-Rab7 was microinjected into A431 cells as a positive control (Figure 2.4.5).

Rab7 is required for early endosome to late endosome transport and late endosome fusion with lysosomes, thereby it is often observed to be localized in perinuclear regions.[162, 164] As shown in Figure 2.3.5, YFP-Rab7 is mainly in the cytosol immediately after microinjection (Figure 2.3.5A). After ~3.5 hrs incubation of the cells at 37 °C, the proteins were mainly localized in the perinuclear region (Figure

2.3.5B). Rab7 was observed to be localized on the vesicle membrane, which can be clearly seen in Figure 2.3.5C.

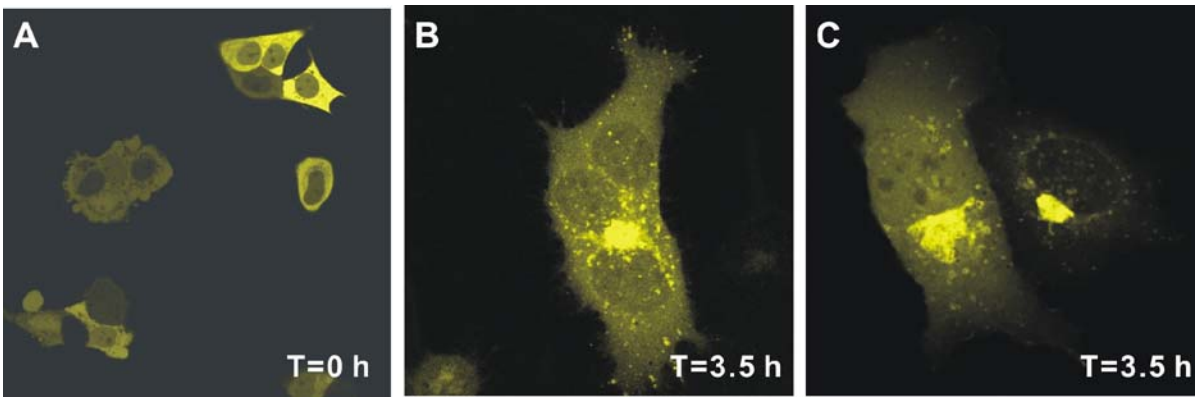

Figure 2.3.5 Targeting of YFP-Rab7 in human A431 cells. 25 μM of YFP-Rab7 were microinjected into the A431 and the living cells were observed with confocal laser scanning microscope. Microinjection and observations were done in room temperature whereas the cells were incubated at 37 °C the rest of the time.

In this work, Rab7 with a His_6 tag at the N-terminus was tried to bind to Ni-NTA-functionalized PEG2000-QDs via the Ni-NTA-affinity coordination (Figure 2.4.1). The C-terminus of Rab7, which is crucial for the prenylation modification, should be available. Ni-NTA functional groups were introduced by doping 10% of 1,2-Dioleoyl-*sn*-Glycero-3-[(N-(5-amino-1-carboxypentyl)iminodiacetic acid)succinyl] (Nickel salt) (DOGS-NTA) with 90% of 1,2-Distearoyl-*sn*-Glycero-3-Phosphoethanolamine-N-[Methoxy(Poly ethylene glycol)-2000] (18:0 PEG2 PE) for the encapsulation of QDs. The Ni-NTA functional groups were confirmed by a FRET-based assay, which a Cy5 modified His_6-peptide (Cy5-CGKGHHHHHH) was used as energy acceptor for QDs (Figure 2.4.6). As illustrated in Figure 2.4.6A, the spectra overlap of the emission of 532 nm- or 586 nm-emitting QDs and the absorbance of Cy5 allows the FRET between QDs and Cy5.

An exemplary 586 nm-emitting QDs sample was used for the FRET test to confirm the successful attachment of Ni-NTA groups. A titration experiment with increasing addition of Cy5-peptide to NTA-PEG2000-QDs586 showed the saturation number of Cy5-peptide on one QD is ~5 (data not shown). Therefore two comparison experiments were carried by adding 5 equiv of Cy5-peptide to Ni-NTA modified QDs and non-NTA QDs, respectively. The PEG2000-QDs with Ni-NTA functionalization caused much larger (~72%) donor quenching and Cy5 emission enhancement than the control sample without Ni-NTA (~9.5% donor quenching), which confirmed the existence of Ni-NTA groups (Figure 2.4.6B). The relatively week Cy5 emission are possibly due to the increased donor/acceptor distance

due to the large hydrodynamic size of PEG2000-QD586, ~18 nm. In this work, no further investigations on this issue were done.

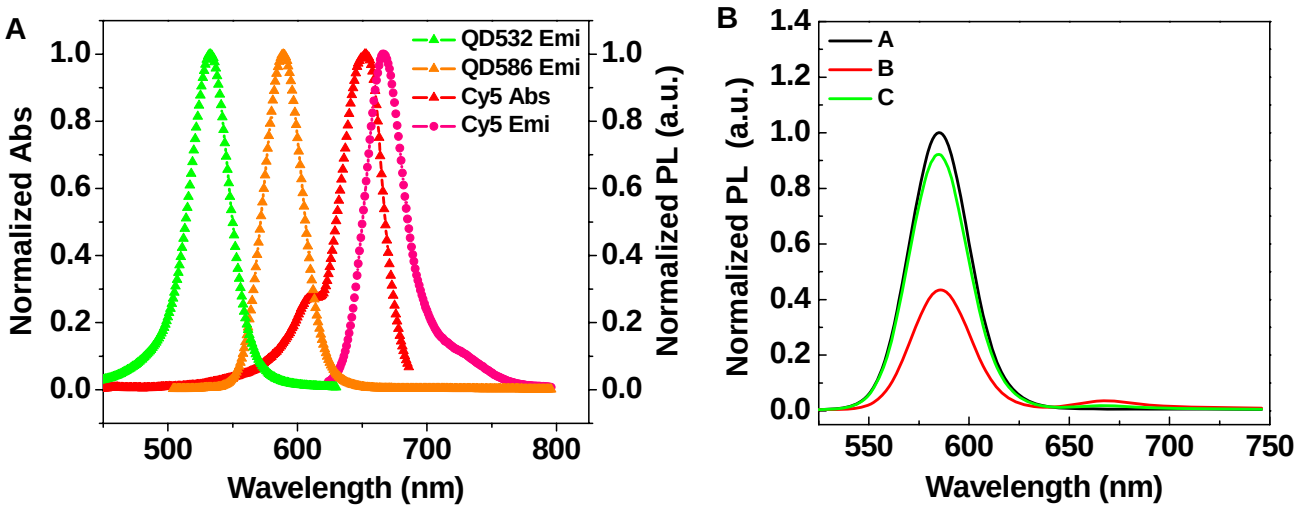

Figure 2.4.6 FRET test of (Ni-NTA)-PEG2000-QD586 and Cy5 modified 6xHis-peptide. (A) spectroscopic characterization of 532 nm- and 586 nm-emitting QDs emission, Cy5 absorption and emission. (B) Black curve A is the normalized emission spectra PEG2000-QD586 (with or without Ni-NTA); red curve B and C are the emission spectra of the systems of 5 equiv of Cy5-peptide plus 1 equiv of NTA-PEG2000-QD586 and non-NTA sample as a control, respectively. Strong PL quench of QDs and an enhancement at ~670 nm of Cy5 emission were seen in the case of curve B (QDs with Ni-NTA groups), whereas, week PL quench of QDs and low Cy5 signal were observed in the non-NTA QDs case. Note that all the emission were normalized against the donor emission intensity at the absence of Cy5-peptide.

The binding of His_6-tagged Cy5-peptide to Ni-NTA modified QDs was further confirmed by an agarose electrophoresis (Figure 2.4.7). In both cases of 532 nm- and 586 nm-emitting QDs, NTA-QD-Cy5-peptide conjugate has smaller electrophoretic mobility than QD itself. The larger the conjugates (with more Cy5-peptide per QD) are, the smaller the mobility will be. All these prove the authentic binding of Cy5-peptide and the existence of Ni-NTA groups on QDs. As comparison, the QDs without Ni-NTA groups did not show any electrophoretic mobility differences with or without the addition of Cy5-peptide.

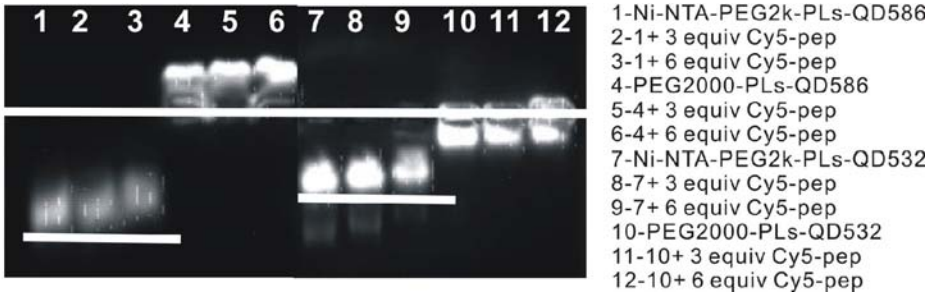

Figure 2.4.7 agarose gel electrophoresis of (NTA)-PEG2000-QD586 (532)/His_6-tagged Cy5-peptide conjugates. 0.6% agarose gel were prepared and run at 180 V in TB buffer for ~45 min.

The NTA-PEG2000-QDs were then used for the conjugation with His_6-tagged Rab7 and confirmed by agarose gel electrophoresis (Figure 2.4.8). As an example, the Rab7-QD532 conjugates showed smaller electrophoretic mobility than QD532 itself due to the larger size of protein-QD conjugates compared with QDs. The lane 5-8 illustrated the mobility for QD586 and Rab7-QD586 conjugates, in which the protein-QD conjugates have larger mobility than QD586 itself. The reason for inconsistency between QD532 and QD586 cases probably due to the varied charge/size ratio. In the case of QD532, which the size and weight of QD itself is smaller, the binding of Rab7 will dramatically increase the size and that makes the mobility differences larger. In the Rab7-QD586 conjugates, the surface charge factor is dominant, therefore the conjugates with more proteins are of larger surface charge and migrate faster.

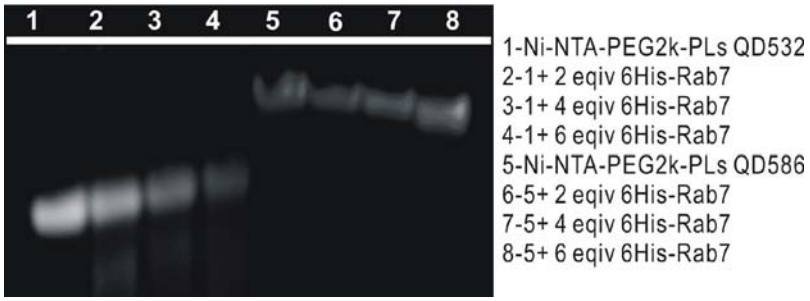

Figure 2.4.8 agarose gel electrophoresis of (NTA)-PEG2000-QD586 (532)/His_6-tagged Rab7 conjugates. 0.6% agarose gel were prepared and run at 200 V in TB buffer for ~1 hr.

The Rab7-QD conjugates were then purified by a cut-off vivaspin® concentrator and microinjected into A431 cells. However, after a certain period of time (~2-6 hrs), no apparent localization of Rab7 was seen. The Rab7 proteins are supposed to complete the prenylation reaction and will target at the perinuclear region within this period of time.[162, 166] No targeting signal of QDs was observed, which may be attributed to two possible reasons. (i) Rab7-QD conjugates failed to get prenylation

modification; (ii) the prenylated Rab7-QD failed to get into the organelle membranes. Rab7 proteins on QD surface are in different state of the free proteins. The space limitation on the QD surface may bring difficulties for the REP1 and RGGT enzymes getting close and reacting with Rab7. The multiple immobilization of Rab7 on one QD, which is a little similar with precipitate of the proteins on the solid phase, could make the proteins lose some activity and deteriorate this circumstance. Furthermore, the large hydrodynamic diameter of Rab7-QD conjugate slows the mobility and also increases the non-specific binding, which is very unfavorable for the *in vivo* imaging. To investigate these problems in-depth, more experiments are needed.

As an outlook, there are several challenges remained for using PEG2000-QDs for intracellular imaging. (i) Conjugating of Rab7 to QDs via Ni-NTA functionality is not always efficient. In this work, some preparation failed to get Rab7-QD conjugates. One possible reason is that the Ni-NTA groups were actually "buried" in the PEG "forest" and hindered the approach of the proteins, because the Ni-NTA functional phospholipids are short of PEG2000 chain and much shorter than the other phospholipids. (ii) Multivalency of the functionalized QD will bring many problems such as increased conjugate size and non-specific binding and adsorption for *in vivo* imaging. A single functional group QDs are difficult to prepare by this doping method. Recently, Bawendi and co-workers made an approach to solve the multivalency problem by gel electrophoresis purification, which aroused wide interest.[87] (iii) The large hydrodynamic diameter of PEG2000-QDs also brings the mobility and non-specific binding problems. In some cases such as mapping of lymph node or the renal clearance study,[69, 121], this type of QD is not capable to get through the tissues. (iv) The PEG chain on QD surface could potentially interact with the lipid bilayer of organelle membranes,[169] which certainly complicates for specific targeting. (v) The posttranslational procedure of Rab proteins is highly intricate and requires the co-functionality of several enzymes at the same time. Any space hindrance blocking the active binding sites could cause the failure of the function of enzymes.

2.4.3 Summary

In this chapter, the *in vitro* and *in vivo* stability of DHLA-, non-PEG-PLs, PEG350-PLs and PEG2000-PLs-coated QDs samples were studied and compared. The PEG2000-QDs are the most stable QDs for *in vivo* imaging studies. The Rab7-QDs conjugates were prepared and characterized. However the comprehensive study to explore the application of Rab7-QDs in cellular imaging is still missing at this stage.

As discussed in chapter 2.2, despite the high stability and biocompatibility, the drawback of PEG2000-PLs coated QDs is their relatively large size (~12-20 nm), which presents a barrier to the widespread implementation of QDs for biological imaging. The large size also increases the possibility of non-specific binding and potentially interferes with the function of tagged proteins. The combination of the DHLA-QDs' reduced HD and the high stability of PEG-coated QDs would be an ideal solution for this issue. Modification of QDs with PEG-terminated DHLA molecules is such a promising combination. PEG-DHLA functionalized ligands have been synthesized by conjugating a short PEG (5, 8, 12 or 15 repeating units) to DHLA and used to cap QDs by Mattoussi et al in 2005.[66] It has been found that PEG-DHLA cap QDs dramatically improve the stability and limit the nonspecific interaction in biological environments. The most precious advantage of this strategy is the HD of the capped QDs is only a few nanometers larger than the inorganic core (i.e. HD ~9.9 nm for a 565 nm-emitting QD). These functionalized QDs have excellent performances both *in vitro* and *in vivo* and have been applied in imaging and sensing investigations in the recent 1-2 years.[67-70]

3 Summary and Outlook

The synthesis, characterization of and the biological applications of water-soluble luminescent QDs CdSe/ZnS were carried out during this work. Various water-solubilization and surface-modification strategies, such as ligand-exchange and phospholipid micelle coating were applied to render the TOPO/TOP-capped QDs suitable in water. The dihydrolipoic acid (DHLA)-coated QDs were used for the fabrication of a QD/fluorescent protein donor system for a long-range FRET detection. The lipid-coated QDs were introduced into the living cells and their stability was investigated *in vitro* and *in vivo*.

Initially, a series of luminescent CdSe NCs with size ranging from ~2.74 to 4.65 nm were synthesized *via* a pyrolysis using CdO and TOPSe (Section 2.1.2). An inorganic shell of ZnS was grown on the CdSe surface to passivate the core and achieve a higher photoluminescence quantum yield. The resulting QDs CdSe/ZnS were dispersed in chloroform with emission wavelength of ~522 to 625 nm and quantum yield of ~20-70% (Section 2.1.3).

Two different types of strategies were used to prepare water-soluble and functionalized QDs in this work. Firstly, dithiolated molecules DHLA were used to substitute the TOPO/TOP ligands and introduce QDs into aqueous media. The negatively charged DHLA-QDs allow the immobilization of His_6-tagged proteins onto the particle surfaces (Section 2.2.1). Second strategy to obtain stable water-soluble QDs was use of PEG-phospholipids (PEG-PLs) to encapsulate QDs giving PLs micelle-coated QDs (Section 2.2.2). Properties of both types of QD were thoroughly investigated particularly concerning their stability.

In a second part of the thesis, a self-assembled donor complex comprising DHLA-QD and fluorescent proteins were fabricated and used for the FRET-based investigations. QDs serve as energy donors as well as nanoscaffolds which immobilize multiple acceptor fluorescent proteins on one QD to achieve higher energy transfer efficiency (Section 2.3.1).

A detailed analysis of a 3Ch-FRET supramolecular system was presented in this work, which comprised of DHLA-QD518, EYFP and DNA-Atto647 (Section 2.3.2). The FRET parameters such as Donor/Acceptor separation distances, Förster radii and transfer efficiencies of each of the three implemented QD/EYFP, QD/Atto647 and EYFP/Atto647 2Ch-FRET pairs were elucidated by both

theoretical and experimental approaches. Time-resolved measurements of the 2Ch- and 3Ch-FRET systems confirmed the FRET processes occurring between the three chromophores. The QD/EYFP conjugate functioned as a new donor system which combines the intrinsic advantages of QDs with high quantum yields of EYFP, thereby enabling long-distance FRET processes up to 13 nm.

Finally, cellular stability of phospholipid stabilized QDs was investigated by microinjecting them into A431 cells. PEG2000-QDs were found to be stable in cellular conditions for at least 7 hrs. Microscopic aggregates were observed in the case of PLs-QDs and PEG350-QDs inside the living cells, which implied that the short PEG or non-PEG phospholipid coated QDs were not suitable for cellular imaging. Additionally, Rab7-QD conjugates, suitable for the investigation of Rab7 prenylation mechanism, were prepared and characterized (Section 2.4).

The DHLA-QDs and phospholipid-coated QDs developed in this work have a potential for a wide range of biological applications in sensing, imaging and diagnostics. The small size of DHLA-QDs allows them serve as an efficient energy donor for other chromophores such as dyes, fluorescent proteins or other nanoparticles. The self-assembled QD/fluorescent protein powerful donor system would find possible applications in an *in vivo* or *in vitro* long-range FRET-based detection. However, much work remains to be done before the full potential of these functionalized QDs can be realized. In particular, the functional protein/QD conjugates possessing high solution stability across wide pH range and under harsh conditions; reduced hydrodynamic size and non-specific binding and controllable surface functional valency are favorable biofunctional conjugates for cell-labeling applications such as cellular post-translational modification investigations.

4 Zusammenfassung und Ausblick

In Rahmen dieser Arbeit wurde die Synthese, Charakterisierung und biologische Anwendung von wasserlöslichen kolloidalen Halbleiternanopartikeln, häufig auch als *Quantum Dots* (QDs) bezeichnet, behandelt. Verschiedene Strategien zur Oberflächen-Modifizierung, wie z. B. Liganden-Austausch oder Beschichtung mit Phospholipid-Mizellen wurden eingesetzt, um die TOPO/TOP-beschichteten QDs in wässrige Lösung zu überführen. DHLA-beschichtete QDs wurden verwendet zur Herstellung eines Systems aus QD und einem fluoreszenten Protein, die gemeinsam als supramolekularer Donor für weit reichende FRET Detektion dienten. Die Stabilität von lipid-beschichteten QDs wurde sowohl *in vitro* als auch *in vivo* durch Einbringen in lebende Zellen untersucht.

Zunächst wurde eine Reihe lumineszenter CdSe Nanopartikel (NPs) mit Größen von ~2.74 bis 4.65 nm mit Hilfe einer Pyrolyse von CdO und TOPSe synthetisiert (Kapitel 2.1.2). Zum Erreichen einer höheren Quantenausbeute und zur Passivierung des CdSe Kerns wurde eine anorganische Hülle aus ZnS hinzugefügt. Die erhaltenen CdSe/ZnS QDs wurden in Chloroform gelöst und zeigten Emissions-Maxima bei Wellenlängen von ~522 bis 625 nm und Quantenausbeuten von ~20-70% (Kapitel 2.1.3).

Zur Herstellung funktionalisierter, wasserlöslicher QDs wurden in dieser Arbeit zwei verschiedene Strategien eingesetzt. Zunächst wurden die TOPO/TOP Liganden auf der Oberfläche der QDs durch das dithiolierte Molekül Dihydroliponsäure (DHLA) ersetzt, so dass wasserlösliche QDs erhalten wurden. Die negativ geladenen DHLA-QDs ermöglichten im Weiteren die Immobilisierung von His_6-markierten Proteinen auf der Oberfläche der Partikel (Kapitel 2.2.1). Die zweite Methode zur Herstellung wasserlöslicher QDs basierte auf dem Einkapseln der QDs mit PEG-Phospholipiden (PEG-PLs), so dass mizell-beschichtete QDs erhalten wurden (Kapitel 2.2.2). Die Eigenschaften beider Typen von QDs wurden speziell bezüglich ihrer Stabilität eingehend untersucht.

In einem zweiten Teil der Dissertation wurde ein selbst-organisierter Donor-Komplex aus DHLA-QDs und fluoreszenten Proteinen hergestellt und für FRET-basierte Experimente eingesetzt. Die QDs dienen sowohl als Energie-Donor als auch als Nano-Gerüst, auf dem multiple fluoreszente Akzeptorproteine immobilisiert werden können, um eine höhere Energietransfereffizienz zu erhalten (Kapitel 2.3.1).

Eine detaillierte Analyse eines supramolekularen 3Ch-FRET Systems bestehend aus DHLA-QD522, EYFP und DNA-Atto647 wurde in dieser Arbeit präsentiert (Kapitel 2.3.2). Die FRET Parameter wie z.B. Donor/Akzeptor-Abstände, Förster-Radii und Transfer-Effizienzen von jedem der drei enthaltenen 2Ch-FRET Paare (QD/EYFP, QD/Atto647 und EYFP/Atto647) wurden mit Hilfe theoretischer und experimenteller Ansätze ermittelt. Zeitaufgelöste Messungen der 2Ch- und 3Ch-FRET Systeme bestätigten die zwischen den drei Chromophoren auftretenden FRET Prozesse. Die QD/EYFP Konjugate fungierten als neues Donor-System, das die intrinsischen Vorteile von QDs mit den hohen Quantenausbeuten von EYFP kombiniert und somit weitreichende FRET Prozesse über Distanzen von bis zu 13 nm ermöglicht.

Darüber hinaus wurde die zelluläre Stabilität von phospholipid-modifizierten QDs mittels Mikroinjektion in A431 Zellen untersucht. Es konnte gezeigt werden, dass PEG2000-QDs für mindestens 7 Stunden unter zellulären Bedingungen stabil sind. Im Falle der PL-QDs und der PEG350-QDs wurden Aggregate in den lebenden Zellen gefunden, woraus geschlossen wurde, dass QDs beschichtet mit Phospholipiden ohne PEG oder mit kurzen PEG-Molekülen nicht geeignet sind für Untersuchungen in Zellen. Zusätzlich wurden Rab7-QD Konjugate hergestellt und charakterisiert, die sich eignen zur Untersuchung des Rab7 Prenylierungs-Mechanismus (Kapitel 2.4).

Die DHLA- bzw. phospholipid-beschichteten QDs, die im Rahmen dieser Arbeit entwickelt wurden haben Potential für einen großen Bereich von biologischen Anwendungen wie Sensortechnik, Markierung und Mikroskopie von lebenden Zellen und Diagnostik. Die kleine Größe der DHLA-QDs ermöglicht eine Verwendung als effizienter Energiedonor für andere Chromophore wie Farbstoffe, fluoreszente Proteine oder andere Nanopartikel. Das selbst-organisierte leistungsstarke Donorsystem aus QD und einem fluoreszenten Protein könnte z.B. bei weitreichenden FRET-basierten Detektionsmethoden *in vivo* oder *in vitro* zum Einsatz kommen. Dennoch sind weitere Arbeiten erforderlich, bevor das ganze Potential dieser funktionalisierten QDs umgesetzt werden kann. Die funktionellen Protein/QD Konjugate zeigen in Lösung eine hohe Stabilität über weite pH-Bereiche und unter extremen Bedingungen. Darüber hinaus zeichnen sich diese biofunktionalisierten Konjugate durch einen reduzierten hydrodynamischen Durchmesser, verringerte unspezifische Bindungen und kontrollierbare Oberflächen-Ladung aus, so dass sie gut geeignet sind für Anwendungen in der Markierung von Zellen wie z. B. Untersuchungen von post-translationalen Modifikationen.

5 Experimental Section

5.2 Materials and methods

5.2.1 Equipments

Atomic force microscope	NanoWizard (JPK Instruments)
Centrifuges	Centrifuge 5415R and 5804R (Eppendorf)
Confocal microscope	DM IRB, TSC-2 (Leica)
Fluorescence spectrophotometer	Cary Eclipse (Varian)
FPLC system	Äkta purifierTM (Amersham Pharmacia Biotech)
	Peptide and MonoQ HR5/5 (Pharmacia)
Gel documentation device	AlphaImagerTM 2200 (Alpha Innotech)
Gel electrophoresis unit	Mini-Protean 3 (BioRad)
Tyco thermal controls (Heating alloy bath)	LSG 2ER/250 mL (Isopad)
Microinjection devices	Transjector 5246, micromanipulator 5171,
	(Eppendorf)
3-neck flasks	50, 100 mL, 14/20 joints (Schott Duran)
pH meter	InLab®423 (InLab)
Rotary evaporator	Laborotor 4000 (Heidolph)
Scanner	OptikPro St64+ (Plustek)
Transmission electron microscope	Philips-CM200 (Philips)
Thermocouple	TD 2000 (Isopad)
Thermo mixer	Thermomixer comfort (Eppendorf)
UV/Vis spectrophotometer	Cary 100 Bio (Varian)
UV lamp hand set	(Benda)
Ultra-centrifuge	RC M120EX (Sorvall,. Inc.)
Analysis software	Office XP, Origin 70, CorelDRAW 11,
	PhotochemCAD

5.2.2 Materials

Centrifugal filtration vivaspin®	500, 2, 6, 15 (Sartorius Stedim biotech)
Gelfiltration columns	NAP5, NAP10 (Pharmacia)
Gel extraction kit	UltraPrep Gel-Ex (Molzym)
Micropipettes	Eppendorf
Micropipette tips	Eppendorf, Biozym
Reactions tubes	0.25 mL, 1.5 mL and 2 mL (Eppendorf, Biozym)
	5 mL, 14 mL and 50 mL (Greiner)
Ultra filtration units	Centricon 30 (Millipore)

5.2.3 Reagents

Acrylamide/Bis 37.5:1; 30% solution (w/v)	Applichem
Agarose	Biorad
Bovine Serum Albumin	Sigma
DNA ladder (50 bp, 123 bp)	MBI Fermentas
DTT	Sigma
2-Mercaptoethanol	Sigma-Aldrich
Silver staining kit	ICN Biomedicals, Bio-Rad
sSMCC	Pierce
SybrGold®	Molecular Probes
TOP	Fluka
TOPO, 90%	Fluka
HDA	Sigma-Aldrich
DDA	Sigma-Aldrich
TDPA	AlfaAesar
CdO	Fluka
Selenium, powder	Riedel
OG	Fluka
Phospholipids	Avanti Polar Lipids
Potassium *tert*-butoxide	Fluka
$(TMS)_2S$	Sigma-Aldrich

$ZnEt_2$	Sigma-Aldrich

5.2.4 Buffers

All reagents used for buffer preparation were purchased from Sigma-Aldrich, Fluka, Acros, Applichem, ICN Biomedicals, Roche, Roth and Merck, unless otherwise stated. Specifically, only ultra-pure water (Milli-Q Synthesis, Millipore) was used for buffer preparation.

Table 5.1 List of buffer and constituents

Buffer	Ingredients
6X sample loading buffer	10 mM Tris-HCl (pH 7.6), 0.03% bromophenol blue (BPB), 60% Glycerol, 60 mM EDTA.
Borate	10 mM boric acid, pH 9
Glycine	25 mM Tris, 192 mM Glycine, pH 8.5
HEPES	25 mM Hepes pH 7,2, 40 mM NaCl, 2 M $MgCl_2$, 10 µM GDP, 1 mM DTE
Living cells	150 mM NaCl, 5 mM KCl, 1 mM $MgCl_2$, 1 mM $CaCl_2$, 20 mM HEPES pH 7,4, 10 mM Glucose
PBS	16.7 mM KH2PO4, 83.3 mM K_2HPO_4, 150 mM NaCl, pH 7.3
PBSE	36.4 mM KH2PO4, 63.6 mM K2HPO4, 150 mM NaCl, 5 mM EDTA, pH 6.8
TB	89 mM Tris-HCl, 89 mM boric acid
TBE	89 mM Tris-HCl, 89 mM boric acid, 2 mM EDTA, pH 8.4
TBS	20 mM Tris-HCl, 150 mM NaCl, pH 7.35
TBS-Tween	20 mM Tris-HCl, 150 mM NaCl, pH 7.35, 0.05% Tween 20
TE	10 mM Tris-HCl, 1 mM EDTA, pH 7.5
TETBS	20 mM Tris-HCl, 150 mM NaCl, 5 mM EDTA, 0.005% Tween, pH 7.5

5.2.5 Oligonucleotides

Oligonucleotides A24 and modified A24 used for preparing fluorescent protein-DNA conjugates were purchased from Thermo Electron. Atto647 modified oligonucleotides cA24 were purchased from TIB MOLBIOL (Berlin, Germany). The sequences are listed in Table 5.2

Table 5.2 Sequences of Oligonucleotides

Oligonucleotide	Sequence (5´-3´)
aA24	Amino-TCC TGT GTG AAA TTG TTA TCC GCT
aA24m1	Amino-TCC TA*T GTG AAA TTG TTA TCC GCT
aA24m2	Amino-TCA TGT GTG AAA TTG TTA TCC GCT
aA24m3	Amino-TCC TGT ATG AAA TTG TTA TCC GCT
3´-Atto647-cA24	AGC GGA TAA CAA TTT CAC ACA GGA(-Atto647)
5th-Atto647-cA24m1	AGC GGA TAA CAA TTT CAC AT(-Atto647)A GGA
3rd-Atto647-cA24m2	AGC GGA TAA CAA TTT CAC ACA T(-Atto647)GA
7th-Atto647-cA24m3	AGC GGA TAA CAA TTT CAT(-Atto647) ACA GGA
10th-Atto647-cA24	AGC GGA TAA CAA TTT(-Atto647) CAC ACA GGA
17th-Atto647-cA24	AGC GGA T(-Atto647)AA CAA TTT CAC ACA GGA
5´-Atto647-cA24	(Atto647-)AGC GGA TAA CAA TTT CAC ACA GGA

* The underline bases are those substitutes in modified oligonucleotides for those in A24 and cA24 oligonucleotides.

5.3 Synthesis and characterization of CdSe/ZnS QDs

Trioctylphosphine/trioctylphospine oxide (TOP/TOPO)-capped CdSe/ZnS core/shell nanocrystals were prepared using method of high temperature growth and annealing of organometallic compounds, similar to the methods previously described.[16, 35, 39, 49, 129] Here the modified Peng preparation protocol was followed, where cadmium oxide (CdO) was used as cadmium resource. Tetradecylphosphonic acid (TDPA), dodecylamine (DDA) and TOPO served as coordinating molecules. Diethylzinc ($ZnEt_2$) and hexamethyldisilathiane ($(TMS)_2S$) were used as the Zn and S precursors for the CdSe overcoating.

5.3.1 CdSe core synthesis

The TOPSe stock solution was prepared by mixing 7.896 grams selenium powder with 100 mL TOP and stirring overnight. The obtained solution is air stable and can be kept out on the bench for months. The only side effect of air exposure is the eventual formation of TOPO. To start the core synthesis, a mixture of 2 g of 90% TOPO, 2.88 g of DDA, 0.3 g of TDPA and 0.05 g of CdO was heated to 100 °C, while vacuum was applied to remove the oxygen and humidity. Then the temperature setting was raised to ~300 °C. At this point the red color of the CdO started to disappear. Oxygen was being evolved and TDPA was coordinating to the Cd ion. The highest temperature that can actually be reached was

around 260-290 °C. This temperature was maintained for approximately 5-10 mins until the mixture solution became completely clear. At this point, the mixture reagents of 0.25 mL of 1M TOPSe and 4mL 90% TOP were injected into the cadmium solution. Upon addition, the temperature of the mixture dropped immediately to ~240 °C with some evolution of gas. Afterwards the temperature was slowly raised back to 300 °C. The color of the solution turned slightly yellow, then darker yellow, then orange, then to dark orange, then wine red and dark red and so forth. The period of time of the color change varied from a few seconds at the beginning to several hours at the end. At each point aliquots could be taken and characterized by UV/Vis spectroscopy to see the growth of the particles. The growth of the CdSe dots could be halted by rapid cooling to a temperature below around 200 °C, because the growth of the dots only occurs above 200°C. The heating should be removed at some point to cease the particle growth to obtain desired size of CdSe. Once the preparation was completed, 10 mL of butanol were added to keep the TOP/TOPO from freezing and becoming a solid. The CdSe NCs were collected by size-selective precipitation with methanol and then redispersed in chloroform or hexane. UV/Vis absorption spectra and photoluminescence spectra were acquired on Cary 100 Bio (Varian) spectroscopy and Cary Eclipse (Varian) fluorescent spectrophotometer. The size of the single CdSe particle was determined by the first UV/Vis absorption peak based on the previously published work.[30-32, 34] With the size of the NCs, the extinction coefficient was determined. Hence the particle concentration was obtained from the UV/Vis absorbance.[30-32, 34]

5.3.2 ZnS overcoating

Once the CdSe particle size as well as the concentration of CdSe NCs was determined, the ZnS overcoating calculations were done base on the total volume of the ZnS shell. The calculations were performed with the assumption that the particles are perfectly spherical and the thickness of a ZnS monolayer is ~0.31 nm.[35] The volume of total ZnS needed were finally converted to the volume of each precursor solution ($ZnEt_2$ and $(TMS)_2S$). According to the calculation, CdSe was crushed out of a certain volume of stock solution by methanol and dried. The mixture of CdSe, 5 g of TOPO and 2.5 g of hexadecylamine (HDA) was heated to 150 °C and degassed. The overcoating solution was prepared afore in a glove box where the calculated amounts of $ZnEt_2$ and $((TMS)_2S$ were added to 5 mL of TOP. This precursor solution was then added slowly to the heated mixture. The addition should proceed very slowly over at least 30 mins. The resulting core/shell CdSe/ZnS nanocrystals can be collected by the

similar precipitation procedure with methanol and purified by re-precipitation for several times. The CdSe/ZnS QDs can be resolved in hexane or chloroform at room temperature.

5.3.3 Characterization of CdSe/ZnS QDs

The resulting CdSe/ZnS NCs were characterized by UV/Vis spectroscopy, fluorescent spectroscopy and transmission electron microscopy (TEM). The nanocrystals were purified by precipitation with methanol, accompanied by centrifuging and subsequent washing with anhydrous methanol to rinse the residual TOPO. The CdSe/ZnS QDs were then dispersed in anhydrous chloroform. Dilutions of this concentrated QDs solution were later used for room-temperature optical characterization. The absorption spectra were acquired on Cary 100 Bio (Varian) UV/Vis spectroscopy. The luminescence spectra were acquired on Cary Eclipse (Varian) fluorescent spectrophotometer. These spectra were later compared with those of CdSe. The TEM images of CdSe/ZnS were acquired on a Philips CM200 electron microscope operating at 200 kV. The samples were prepared by dropping the diluted solution of QDs in chloroform onto carbon coated 400 mesh copper grids. The quantum yield of CdSe/ZnS QDs was estimated by comparing the integrated fluorescent intensity to that of rhodamine 6G in ethanol.[170] The integrated fluorescent intensity of QDs solutions in hexane and rhodamine 6G in methanol were compared based on equation 5.1. Both QDs sample and standard solution were excited at 480 nm.

$$\phi_{QD} = \phi_{Std}\left(\frac{A_{Std}}{A_{QD}}\right)\left(\frac{I_{QD}}{I_{Std}}\right)\left(\frac{n_{QD}}{n_{Std}}\right)^2 \qquad 5.1$$

where Φ_{QD} and Φ_{Std} are the quantum yields of the QDs sample and the standard rhodamine 6G, respectively; A_{QD} and A_{Std} are the absorbance of QDs and rhodamine 6G at the excitation wavelength of 480 nm; I_{QD} and I_{Std} are the integrated fluorescent intensity of the QD and rhodamine 6G obtained from fluorescent spectra, respectively; n_{QD} is the refractive index of the solvent hexane for QD, which is 1.3749 at 20 °C and n_{Std} is the refractive index for methanol, which is 1.325 at room temperature.

5.4 Water-solubilization and functionalization of CdSe/ZnS QDs

5.4.1 CdSe/ZnS QDs capping with dihydrolipoic acid (DHLA)

Water-soluble CdSe/ZnS QDs, compatible with aqueous conjugation conditions, were prepared using a stepwise procedure consisting of core-shell nanocrystal synthesis, TOP/TOPO-capping, size selective precipitation, dihydrolipoic acid (DHLA) cap exchange and final washing and cleaning.[56, 63] DHLA

was freshly prepared from distilled lipoic acid by sodium cyanoborohydride ($Na(CN)BH_3$) reduction under carefully controlled conditions.[171] CdSe/ZnS QDs were precipitated by the addition of acetone to the stock solution followed by centrifugation. The resulting precipitate was redissolved in a few drops of chloroform and precipitated again with acetone. Approximately 100 mg of the resulting CdSe/ZnS were resuspended in 100 µL of DHLA and heated to ~60-70 °C and kept at this temperature for 4-8 hrs. After dilution with 1.5 mL of dimethylformamide (DMF), deprotonation of the terminal lipoic acid carboxyl groups was carried out by the slow addition of excess potassium *tert*-butoxide ($K^+(CH_3)_3CO^-$), about 5 times the mass of the initial QDs used. Note that the addition of potassium *tert*-butoxide must be carried out in a very slow way to avoid rapid quenching of the fluorescence. The resulting precipitate consisting of the QDs together with TOP/TOPO reagents was sedimented by centrifugation. The sedimented precipitate was then dispersed in water or PBS buffer, but in some cases solution was slightly turbid because of released TOP/TOPO molecules. Centrifugation or filtration of the dispersion permitted removal of the TOP/TOPO and provided a clear dispersion of the carboxyl capped QDs. The QD dispersion was further separated from excess hydrolyzed potassium *tert*-butoxide and residual DMF by 3-4 cycles of concentration/dilution, using an Ultra-free centrifugal filtration device (vivaspin® concentrator, 10 kDa MW cutoff), and redispersed in water. The final clean and stable aqueous QD dispersions had the emission characteristics of the initial QDs and a quantum yield of ~3-10% obtained by the strategy described in 5.2.3 using the rhodamine 6G as the standard. The resulting DHLA-QDs solution was diluted till 5-20 µM and stored at 4 °C for future use. QD particle concentrations were estimated from the same absorbance and extinction coefficient that was used for CdSe/ZnS samples measured shortly after preparation.[30-32] The polar-capped, negatively charged QDs are stable and have useful luminescence emission only in buffered basic solutions at pH >~6. More acidic solutions induce precipitation of the QDs along with a substantial loss in the PL emission, due to loss of surface charge upon DHLA cap protonation and loss of cap affinity for the ZnS overcoat. The monodispersity of DHLA-QDs was further confirmed by atomic force microscopy (AFM). Briefly, negatively charged DHLA-QDs solution was dropped on the Mg^{2+} modified mica surface and let dry. The mica was then scanned by the tapping mode with a frequency of 200-400 Hz on the NanoWizard AFM.

5.4.2 PEG2000-Phospholipid micelle-stabilized QDs CdSe/ZnS

CdSe/ZnS QDs can be encapsulated in hydrophobic cores of a micelle composed of a mixture of *n*-poly (ethylene glycol) phosphatidylethanolamine (PEG-PE) and functional PEG-PLs.[74] In this thesis, 100 µL of a 10 µM QDs solution were precipitated with methanol and washed thoroughly with methanol and dried to get rid of the solvent. The resulting particles were resuspended with ~2000 molar equivalents (~2.0 µmol) of 1,2-dipalmitoyl-*sn*-glycero-3-phosphoethanolamine-N-[methoxy(poly ethylene glycol)-2000] (mPEG-2000 PE) in ~1 mL of chloroform. 1-2 ml ddH_2O was added to the mixture and the chloroform was evaporated by gentle rotary-evaporation in boiling water. This process only takes ~10 min for obtaining a clear QD water solution. The vacuum can be applied carefully to remove all organic solvent. For purification of encapsulated QDs from excess phospholipids and tiny aggregates, an ultracentrifuge at 80,000g was applied for 5 hrs at 4 °C. The micelles containing QDs formed a pellet while the empty micelles stayed suspended. The supernatant was discarded and the QD-micelles were resuspended in water. An alternative purification strategy is size exclusion chromatography (SEC), which affords QDs samples of higher purity. The Sephacryl S500 HR chromatography column was equilibrated with 20 mM borate buffer (pH 8) for ~2 hrs at a flow rate of 1.0 mL/min. 100 µL of concentrated PEG2000-QDs in borate buffer were loaded on the column and eluted with borate buffer. The PEG2000-QD fraction monitored by UV/Vis signal and was collected and this volume was reduced by a 30kDa MW cutoff vivaspin® concentrator. Functionalized PEG2000-QDs can be prepared by doping 5-10% of functional PEG2000-PLs, such as 1,2-Distearoyl-*sn*-glycero-3-phosphoethanolamine-N-[amino(poly ethylene glycol)2000] (DSPE-PEG(2000)-NH_2) or 1,2-Distearoyl-*sn*-Glycero-3-Phosphoethanolamine-N-[Carboxy(Poly ethylene Glycol)2000] (DSPE-PEG(2000)-Carboxylic Acid). The final PEG2000-QDs solution was characterized by fluorescence spectroscopy, UV/Vis spectroscopy and compared with that of CdSe/ZnS in chloroform. The quantum yields of the samples were also obtained by comparing with rhodamine 6G, ~17-57% for different samples (Table 2.2.1). TEM images of the PEG2000-QDs samples were taken on a Philips CM200 electron microscope to demonstrate the shape, size and monodispersity of the QDs cores.

5.4.3 Non-PEG and PEG350 Phospholipid stabilized QDs CdSe/ZnS

TOPO-stablilized CdSe/ZnS QDs were suspended in chloroform (200 µL of 40 µM solution) containing ~1000 molar equivalent of PLs (~8.0 µmol) composed of : (i) 1-palmitoyl-2-oleyl-sn-glycerophosphatidylcholine (POPC; 90 mol%) and 1-palmitoyl-2-oleyl-sn-glycerophosphatidylglycerol

(POPG; 10 mol%) for producing PLs-QDs; (ii) POPC (80 mol%), POPG (10 mol%), and 1,2-dioleoyl-sn-glycero-3-[N-(5-amino-1-carboxypentyl)iminodiacetic acid succinyl] nickel salt (DOGS-NTA-Ni, 10 mol%), to produce NTA-PLs-QDs; (iii) 1,2-Dioleoyl-*sn*-Glycero-3-Phosphoethanolamine-N-[Methoxy(Poly ethylene glycol)-350] Ammonium Salt (18:1 PEG350 PE) (90 mol%) and DOGS-NTA-Ni (10%) to produce NTA-PEG350-QDs. After adding *β*-octylglucopyranoside (OG, 25 mg in 3.2 mL ddH_2O), the mixture was heated in a 40 °C water bath and the chloroform was evaporated under vacuum. The aqueous PLs-QDs or PEG350-QDs solution was dialyzed twice against 2000 volumes of water or PBS buffer to remove the detergent. The PLs-QDs or PEG350-QDs can be further purified and washed with water or buffer and concentrated by a 10 kDa MW cutoff vivaspin® concentrator. The resulting PLs-QDs and PEG350-QDs solution was characterized by fluorescence spectroscopy, UV/Vis spectroscopy and compared with CdSe/ZnS in chloroform. The quantum yields of the samples were also obtained by comparing with rhodamine 6G, ~4.4-18 % for different samples (Table 2.2.1). TEM images of the PLs-QDs samples were took on a Philips CM200 electron microscope to demonstrate the shape, size and monodispersity of the QDs cores.

5.5 Synthesis and characterization of QD/fluorescent protein conjugate

5.5.1 Synthesis of EYFP-DNA conjugates

The fluorescent protein EYFP (emission at 528 nm, extinction coefficient ε=84 000 $M^{-1}cm^{-1}$) was covalently coupled to the 5'-end of the 24-mer amino-modified single-stranded DNA (ssDNA) aA24 (sequence: 5'amino-TCC TGT GTG AAA TTG TTA TCC GCT-3') or one bp modified aA24m1 (sequence: 5'amino-TCC TAT GTG AAA TTG TTA TCC GCT-3'), aA24m2 (sequence: 5'amino-TCA TGT GTG AAA TTG TTA TCC GCT-3'), aA24m3 (sequence: 5'amino-TCC TGT ATG AAA TTG TTA TCC GCT-3') yielding EYFP-A24 (or EYFP-A24m1, EYFP-A24m2, EYFP-A24m3) conjugate using a coupling strategy developed previously.[149, 151] Briefly, an EYFP mutant was created by site-directed mutagenesis containing an extra cysteine residue at the C-terminus, which is exposed on the protein's surface. The protein was expressed in *E.coli* and purified by Ni^{2+}-nitrilotriacetic acid (Ni-NTA) chromatography. The 24-mer oligonucleotide containing a aliphatic primary amino group at the 5'-end, was first activated with the heterobifunctional crosslinker Sulfosuccinimidyl-4-[N-maleimidomethyl]-cyclohexane-1-carboxylate (sSMCC), which comprises a maleimide and a N-hydroxy-succinimide (NHS) ester group, that are reactive towards thiols and primary amines, respectively. The maleimide-containing DNA oligomers were purified by gel-filtration and

subsequently coupled to the extra cysteine residue on EYFP. The resulting DNA-EYFP conjugates were purified by anion-exchange chromatography and stored in 20 mM Tris-buffered saline containing 150 mM NaCl, 5 mM EDTA and 0.005% TWEEN-20, pH 7.5 (TETBS buffer). The concentration of EYFP-A24 for instance can be determined by an EYFP/A24 working curve, which considers the absorbances measured at 260 and 280 nm for EYFP/A24 1:1 ratio mixture (Figure 5.1). To measure the concentration of an EYFP-A24 sample, 2 μL of sample solution was added into 198 μL of TETBS buffer, the concentration of the sample was estimated using equation 5.1 or 5.2 and the absorbance at 260 and 280 nm of the resulting solution. The ratio of absorbances measured at 260 and 280 nm, respectively, was found for EYFP-A24 sample to be ~1.46-1.48, and this value was in good agreement with the control solution comprising equiv molar amounts of DNA A24 and the EYFP (1.47, the ratio of two slopes of two curves in Figure 5.1). In contrast, control samples containing either of the two components in a 2-fold excess, i.e., DNA/EYFP 2:1 or DNA/EYFP 1:2, revealed values of 1.61 and 1.41, respectively, thus confirming the 1:1 stoichiometric ratio of DNA/EYFP in the EYFP-A24 conjugate.[149] The similar analysis strategy can also apply to other EYFP-DNA conjugates prepared in this thesis. The absorbance of the EYFP-A24 conjugate at 260 or 280 nm can be translated into the concentration of the sample solution based on one of the fitting curves' experiential equation in Figure 5.1,

$C=-2.3+665\times A_{280}$ 5.1

$C=-2.3+453\times A_{260}$ 5.2

where C is the concentration of EYFP-A24, A_{280} and A_{260} are the absorbances at 260 and 280 nm, respectively.

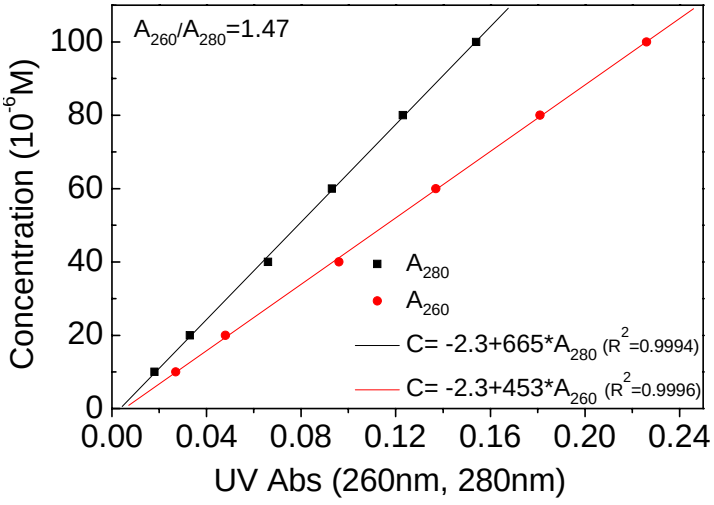

Figure 5.1 EYFP-A24 conjugate concentration working curve. 2μL of EYFP-A24 sample solution can be added to 198 μL of TETBS buffer and the absorbances at 260 and 280 nm are measured. The concentration of the sample can be estimated using either of the aborbances of 260 and 280 nm and fitting equation 5.1 or 5.2.
Native and denaturing PAGE were performed in 10% acrylamide gels. Gel electrophoresis were carried out with 10% acrylamide gels at 4 °C at a constant voltage of 150 V to prevent DNA denaturation due to excessive heating. Gels were stained with SybrGold and a silver developing kit, according to the manufacturer's instructions, and imaged with a UV-Vis gel documentation system using appropriate filters.

Fluorescence emission spectra were carried out with CARY-Eclipse fluorescent spectrophotometer (Varian, Austria) at an excitation wavelength of 490 nm. The absorption spectra were carried out with a 100 Bio UV-Visible spectrophotometer (Varian, Austria). Samples were previously diluted to 0.5 μM in TETBS buffer.

5.5.2 Immobilization of eqFP611 or EYFP-A24 on QDs

The assembly of CdSe/ZnS QDs containing a hydrophilic monolayer of dihydrolipoic acid (DHLA) with DNA-EYFP conjugate **1** and eqFP611 was performed similar to the approach reported by Mattoussi and colleagues, in which polyhistidine–labeled proteins or short peptides were attached to DHLA-capped QDs. It is known that this immobilization occurs due to Zn-hexahistidine coordination.[104] To assemble QD/**1** donor/acceptor FRET conjugates (**2**, in Figure 2.3.7A), DHLA-QD518 (0.1 μM solution in TETBS buffer) were mixed with solutions containing **1** (1.4 μM in TETBS buffer). Control experiments were carried out by using the same concentration of non-His_6-tagged EYFP instead. Titration experiments revealed that the binding of **1** to the surface of DHLA-QDs due to the metal-histidine coordination mechanism, which occurred fast and was completed within a few mins. DHLA-QD/eqFP611 FRET titration experiment was carried out by adding 0-40 equiv molar of His_6-tagged eqFP611 solution to one equiv molar of DHLA-QD536 (0.1 μM solution in TETBS buffer). PLs-QD/eqFP611 titration experiment was carried out by adding 0-58 equiv molar of His_6-tagged eqFP611 solution to one equiv of NTA-PLs-QD532 (0.1μM solution in TETBS buffer).

5.5.3 Fabrication and characterization of three-chromophore FRET system of DHLA-QDs, EYFP and Atto647 modified oligonucleotides

Atto647-labeled oligonucleotides, Atto647-cA24 (emission at 667 nm, extinction coefficient ε=120 000 $M^{-1}cm^{-1}$) were purchased lyophilized from TIB MOLBIOL (Berlin, Germany), dissolved in ddH_2O at a

concentration of 100 μM and stored at -20 ˚C until use. In these conjugates, the Atto647 fluorophore was attached either through a C_6-linker to the 3'-end (**3a**), through a C_7-linker to the 5'-end (**3d**), or through a C_2-linker at two different thymine bases dT at the 10th (**3b**), 17th (**3c**) base pair position from the 3'-end of the 24mer oligonucleotide cA24 (5'-AGC GGA TAA CAA TT(-Atto647)T CAC ACA GGA-3') and at the 3rd (**3e**), 5th (**3f**) and 7th (**3g**) base pair position from the 3'-end of the modified cA24 (5'- AGC GGA TAA CAA TTT CAC ACA T(-Atto647)GA -3' for **3e**; 5'- AGC GGA TAA CAA TTT CAC AT(-Atto647)A GGA -3' for **3f** and 5'- AGC GGA TAA CAA TTT CAT(-Atto647) ACA GGA-3' for **3g**). The QD/EYFP-A24 conjugates **2** and the Atto647-labeled cA24 oligomers were assembled in a two-step process. In the first step, a titration was carried out by continuously adding 0.1-1.4μM of conjugate **1** to 0.1 μM DHLA-QDs in TETBS solution until the saturation of the QD's surface was reached. This titration was followed by fluorescence spectroscopy which indicated the formation of a supramolecular FRET complex comprising a spherical DHLA-QD and ~14 EYFP-A24 conjugates. The resulting two-chromophore FRET system was further referred to as the QD/EYFP 2Ch-FRET subsystem. In the second step, the three-chromophore FRET system was assembled by hybridizing Atto647-labeled cA24 oligomers (**3a**-**d**) to the EYFP-A24 conjugates attached at the QD's surface. This led to the formation of the four 3Ch-FRET systems (**4a**-**d**, respectively) with varying donor-acceptor distances between Atto647 and the EYFP luminescent centre. In TETBS buffer solutions of the final 3Ch-FRET systems, the concentrations of QDs, EYFP-A24 and Atto647-cA24 were approximately 0.1, 1.4, 1.4 μM, respectively. Additional 2Ch-FRET subsystems, EYFP-A24/Atto647, were assembled by hybridization of EYFP-A24 conjugate **1** with the four Atto647-labeled oligonucleotides **3a**-**d**.

To enable determination of direct FRET from the QDs to the Atto647, additional 2Ch-FRET subsystems (denoted as QD/Atto647, were assembled using photobleached EYFP-A24 conjugates to connect the two components. The bleached EYFP-A24 conjugates were also used for the investigation of the unaffected interaction of QD/EYFP. To this end, EYFP-A24 conjugate **1** in TETBS buffer was irradiated using an argon laser with an intensity of 50 mW at the wavelength of 514 nm (EYFP absorbance maximum) at room temperature for ~6-8 hrs. As determined by fluorescence and UV/Vis absorbance spectroscopy, this treatment led an about 99% decrease in the EYFP's PL. The resulting EYFP-A24 species, denoted as **1***, was used for the conjugation with DHLA-QDs to form the QD-protein conjugate **2***. The latter (**2***) was used in fluorescence titration experiments to analyze the increase in QD's PL upon binding to His_6-tagged proteins The 2Ch-FRET QD/Atto647 subsystems,

denoted as **4a*** to **4d***, were assembled using bleached EYFP-A24 **1*** by mixing 14 molar equivalents of **1*** with DHLA-QDs to generate conjugate **2***. The latter was allowed to hybridize with 14 molar equivalents of the Atto647-labeled oligomers **3a-d**. In order to further investigate the FRET systems of the small DNA bp cases, the modified Atto647-cA24 **3e-g** were used to construct EYFP/Atto647 2Ch-FRET systems **5e-g**, and QD/Atto647 2Ch-FRET systems **4e*-4g***, respectively with the similar strategies described earlier.

PL spectra were recorded with a CARY-Eclipse fluorescent spectrophotometer (Varian, Austria), UV/vis spectroscopic measurements were carried out using a 100 Bio UV-Visible spectrophotometer (Varian, Austria). All spectroscopic data were taken at room temperature. The excitation wavelength of the 3Ch-FRET systems was chosen at 372 nm, where the QDs absorb strongly, while both EYFP and Atto647 display minimal absorption. For the monitoring of the PL intensity as a function of detection and excitation wavelength in photoluminescence excitation spectroscopy (PLE), a 150 W Xenon lamp attached to a 1 m monochromator was used as a tuneable excitation source. The excitation wavelength was scanned with a step size of 1 nm while the excitation intensity at that wavelength was measured with a photodiode. The sample's luminescence was recorded with a TE cooled CCD camera attached to a 0.85 m imaging spectrometer resulting in a spectral resolution of 0.4 nm. The acquired spectra were normalized to the exciting photon flux recorded simultaneously and the intensities were displayed as a color coded two-dimensional (2D-PLE) plot with detection wavelength and excitation wavelength as the x and y- axis, respectively. The acquired spectra were background corrected and normalized to the exciting photon flux recorded simultaneously. The resulting intensities were displayed as a color coded two-dimensional (2D-PLE) plot with detection wavelength and excitation wavelength as the x and y-axis, respectively.

Solution of the samples (typically 1.0-1.4 μM in TETBS buffer) in a UV transparent cuvette were illuminated by the frequency doubled output of a Ti:Sapphire laser, resulting in 1mW at 374 nm with a repetition rate of 75.4 MHz and a pulse width of about 150 fs. The luminescence was collected with an achromatic lens, after which scattered excitation light was filtered out by a long pass filter. The PL signal was fed to the entrance slit of a 0.46 m imaging spectrometer with a spectral resolution of 2 nm. The output spectrum was temporally dispersed and recorded using a Hamamatsu streak camera, with a time-resolution of 20 ps. This yielded a two dimensional representation of the PL as a function of emission wavelength and time.

5.6 Phospholipid micelle-stabilized QDs for in vivo cellular imaging

5.6.1 *In vitro* and *in vivo* photoluminescence stability test of micelle-coated QDs

The *in vitro* photoluminescence (PL) stability of QDs with different surface coating was compared by a PL kinetics study. As examples for the PL stability study, DHLA-QD586, PLs-QD586, PEG350-QD586 and PEG2000-QD586 were diluted at a concentration of 0.5 μM in distilled water, PBS buffer and A431 cell lysate, respectively. The PL stability of the four samples was tested by the kinetics program on a CARY-Eclipse fluorescent spectrophotometer and continued for 8 hrs, respectively. The remaining PL was compared with the initial PL for every sample.

The *in vivo* stability of the DHLA-QDs and PEG2000-QDs were carried out by microinjecting of ~1-3 nL of 5 μM samples to living A431 cells. A431 adherent cells were seeded on 30 mm coverslips in 6-wells dishes at a confluence of 300 000 cells/dish and let grown overnight. For microinjection and microscopic observations, cells were incubated in living cells buffer (150 mM NaCl, 5 mM KCl, 1 mM $MgCl_2$, 1 mM $CaCl_2$, 20 mM HEPES pH 7,4, 10 mM Glucose). After observation, cells were incubated in A431 DMEM cell medium at 37 °C with 5 % CO2. Microinjection was done with Eppendorf devices Transjector 5246 and micromanipulator 5171 with an injection time of about 0,5 s and a pressure of about 70-80 hPa. All particles microinjected were dispersed in PBS without any additive and centrifuged 15 min at maximal speed to remove the aggregates.

5.6.2 Rab7-QDs conjugates preparation and characterization

The Ni-NTA functional groups on PEG2000-QDs586 were first verified by FRET-based testing experiments using His_6-tagged Cy5-peptide (Cy5-CGKGHHHHHH) as energy acceptors. The QD/Cy5-peptide conjugates were prepared by mixing one equiv of NTA-PEG2000-QDs586 solution (borate buffer, 0.1 μM) with 1-5 equiv of His_6-peptide-Cy5 solution (borate buffer, 0.1-0.5 μM) and the photoluminescence change of the system were recorded by a fluorescent spectrophotometer. The control experiment was carried out by using PEG2000-QDs586 instead and with the same titration procedure. The binding of His_6-peptide-Cy5 to NTA-PEG2000-QDs586 (or QD532) was confirmed by the agarose gel electrophoresis. One equiv of NTA-PEG2000-QDs586 (or QD532) samples was mixed with 0, 3, 6 equiv of His_6-peptide-Cy5 samples, respectively and run on the 0.6% agarose gel at 180 V for ~40-60 min. As controls, the non-NTA QDs samples were used on the same gel. The fluorescent signals of QDs were detected by the AlphaImager system under the excitation of UV lamp.

The Rab7-QDs bioconjugates were prepared by mixing one equiv of NTA-PEG2000-QDs with ~6 equiv molar of His_6-Rab7 and purified by a 100 kDa Mw cutoff vivaspin® concentrator. The binding was also confirmed by an agarose gel electrophoresis. The NTA-PEG2000-QDs586 (or QDs532) and non-NTA PEG2000-QDs586 (or QDs532) were mixed with 0, 2, 4 and 6 equiv molar of His_6-Rab7, respectively and run on 0.6% agarose gel in TB buffer, at the voltage of 200 V for ~1 hr. The fluorescent signals were detected by the AlphaImager system under the excitation of UV lamp.

6 References

1. Niemeyer, C., M. *Nanoparticles, proteins, and nucleic acids: biotechnology meets materials science*. Angew. Chem. Int. Ed. **40**, 4128-4158 (2001).

2. Drummond, T.G., Hill, M.G. & Barton, J.K. *Electrochemical DNA sensors*. Nat. Biotechnol. **21**, 1192-1199 (2003).

3. Alivisatos, P. *The use of nanocrystals in biological detection*. Nat. Biotechnol. **22**, 47-52 (2004).

4. Daniel, M.C. & Astruc, D. *Gold nanoparticles: Assembly, supramolecular chemistry, quantum size related. properties, and applications toward biology, catalysis, and nanotechnology*. Chem. Rev. **104**, 293-346 (2004).

5. Gao, X., Yang, L., Petros, J.A., Marshall, F.F., Simons, J.W. & Nie, S. *In vivo molecular and cellular imaging with quantum dots*. Curr. Opin. Biotechnol. **16**, 63-72 (2005).

6. Rosi, N.L. & Mirkin, C.A. *Nanostructures in biodiagnostics*. Chem. Rev. **105**, 1547-1562 (2005).

7. Burns, A., Ow, H. & Wiesner, U. *Fluorescent core-shell silica nanoparticles: towards "Lab on a Particle" architectures for nanobiotechnology*. Chem. Soc. Rev. **35**, 1028-1042 (2006).

8. Cai, W. & Chen, X. *Nanoplatforms for targeted molecular imaging in living subjects*. Small **3**, 1840-1854 (2007).

9. Stewart, M.E., Anderton, C.R., Thompson, L.B., Maria, J., Gray, S.K., Rogers, J.A. & Nuzzo, R.G. *Nanostructured plasmonic sensors*. Chem. Rev. **108**, 494-521 (2008).

10. Niemeyer, C.M. & Mirkin, C.A. *Nanobiotechnology: Concepts, Applications and Perspectives*. Wiley-VCH, Weinheim (2004).

11. Mirkin, C.A. & Niemeyer, C.M. *Nanobiotechnology II-More Concepts and Applications*. Wiley-VCH, Weinheim (2007).

12. Alivisatos, A.P. *Semiconductor clusters, nanocrystals, and quantum dots*. Science **271**, 933-937 (1996).

13. Medintz, I.L., Uyeda, H.T., Goldman, E.R. & Mattoussi, H. *Quantum dot bioconjugates for imaging, labelling and sensing*. Nat. Mater. **4**, 435-446 (2005).

14. Michalet, X., Pinaud, F.F., Bentolila, L.A., Tsay, J.M., Doose, S., Li, J.J., Sundaresan, G., Wu, A.M., Gambhir, S.S. & Weiss, S. *Quantum dots for live cells, in vivo imaging, and diagnostics*. Science **307**, 538-544 (2005).

15. Klostranec, J.M. & Chan, W.C.W. *Quantum dots in biological and biomedical research: Recent progress and present challenges*. Adv. Mater. **18**, 1953-1964 (2006).

16. Murray, C.B., Norris, D.J. & Bawendi, M.G. *Synthesis and characterization of nearly monodisperse CdE (E=S, Se, Te) semiconductor nanocrystallites*. J. Am. Chem. Soc. **115**, 8706-8715 (1993).

17. Clapp, A.R., Medintz, I.L. & Mattoussi, H. *Förster resonance energy transferinvestigations using quantum-dot fluorophores*. ChemPhysChem **7**, 47-57 (2006).

18. Somers, R.C., Bawendi, M.G. & Nocera, D.G. *CdSe nanocrystal based chem-/bio-sensors*. Chem. Soc. Rev. **36**, 579-591 (2007).

19. Alivisatos, A.P. *Perspectives on the physical chemistry of semiconductor nanocrystals*. J. Phys. Chem. **100**, 13226-13239 (1996).

20. Woggon, U. *Optical Properties of Semiconductor Quantum Dots*. In Springer Tracts in Modern Physics **Vol. 136** (1996).

21. Rossetti, R., Nakahara, S. & Brus, L.E. *Quantum size effects in the redox potentials, resonance Raman spectra, and electronic spectra of CdS crystallites in aqueous solution*. J. Chem. Phys. **79**, 1086-1088 (1983).

22. Goldstein, A.N., Echer, C.M. & Alivisatos, A.P. *Melting in semiconductor nanocrystals*. Science **256**, 1425-1427 (1992).

23. Ercolessi, F., Andreoni, W. & Tosatti, E. *Melting of small gold particles: Mechanism and size effects*. Phys. Rev. Lett. **66**, 911 (1991).

24. Papavassiliou, G.C. *Luminescence spectra and Raman excitation profiles in small CdS particles*. J. Solid State Chem. **40**, 330-335 (1981).

25. Brus, L.E. *A simple model for the ionization potential, electron affinity, and aqueous redox potentials of small semiconductor crystallites*. J. Chem. Phys. **79**, 5566-5571 (1983).

26. Ekimov, A.I. & Onushchenko, A.A. *Quantum size effect in the optical spectra of semiconductor microcrystals*. Soviet Physics Semiconductors-Ussr **16**, 775-778 (1982).

27. Efros, A.L. *Interband absorption of light in a semiconductor sphere*. Soviet Physics Semiconductors-Ussr **16**, 772-775 (1982).

28. Brus, L.E. *Electron--electron and electron-hole interactions in small semiconductor crystallites: The size dependence of the lowest excited electronic state*. J. Chem. Phys. **80**, 4403-4409 (1984).

29. Brus, L. *Quantum crystallites and nonlinear optics*. Appl. Phys. A: Mater. Sci. Process. **53**, 465-474 (1991).

30. Richter, K. & Kuno, M.K. *ND QD essential*. Internal protocol (2003).

31. Schmelz, O., Mews, A., Basche, T., Herrmann, A. & Mullen, K. *Supramolecular complexes from CdSe nanocrystals and organic fluorophors*. Langmuir **17**, 2861-2865 (2001).

32. Yu, W.W., Qu, L., Guo, W. & Peng, X. *Experimental determination of the extinction coefficient of CdTe, CdSe, and CdS nanocrystals*. Chem. Mater. **15**, 2854-2860 (2003).

33. Li, L.s., Hu, J., Yang, W. & Alivisatos, A.P. *Band gap variation of size- and shape-controlled colloidal CdSe quantum rods*. Nano Lett. **1**, 349-351 (2001).

34. Leatherdale, C.A., Woo, W.-K., Mikulec, F.V. & Bawendi, M.G. *On the absorption cross section of CdSe nanocrystal quantum dots*. J. Phys. Chem. B **106**, 7619-7622 (2002).

35. Dabbousi, B.O., Rodriguez-Viejo, J., Mikulec, F.V., Heine, J.R., Mattoussi, H., Ober, R., Jensen, K.F. & Bawendi, M.G. *(CdSe)ZnS core-shell quantum dots: synthesis and characterization of a size series of highly luminescent nanocrystallites*. J. Phys. Chem. B **101**, 9463-9475 (1997).

36. Spanhel, L., Haase, M., Weller, H. & Henglein, A. *Photochemistry of colloidal semiconductors. 20. Surface modification and stability of strong luminescing CdS particles*. J. Am. Chem. Soc. **109**, 5649-5655 (1987).

37. Steigerwald, M.L., Alivisatos, A.P., Gibson, J.M., Harris, T.D., Kortan, R., Muller, A.J., Thayer, A.M., Duncan, T.M., Douglass, D.C. & Brus, L.E. *Surface derivatization and isolation of semiconductor cluster molecules*. J. Am. Chem. Soc. **110**, 3046-3050 (1988).

38. Brennan, J.G., Siegrist, T., Carroll, P.J., Stuczynski, S.M., Brus, L.E. & Steigerwald, M.L. *The preparation of large semiconductor clusters via the pyrolysis of a molecular precursor*. J. Am. Chem. Soc. **111**, 4141-4143 (1989).

39. Peng, Z.A. & Peng, X.G. *Formation of high-quality CdTe, CdSe, and CdS nanocrystals using CdO as precursor*. J. Am. Chem. Soc. **123**, 183-184 (2001).

40. Peng, X., Wickham, J. & Alivisatos, A.P. *Kinetics of II-VI and III-V colloidal semiconductor. nanocrystal growth: focusing, of size distributions*. J. Am. Chem. Soc. **120**, 5343-5344 (1998).

41. Dushkin, C.D., Saita, S., Yoshie, K. & Yamaguchi, Y. *The kinetics of growth of semiconductor nanocrystals in a hot amphiphile matrix*. Adv. Colloid Interface Sci. **88**, 37-78 (2000).

42. Shiang, J.J., Kadavanich, A.V., Grubbs, R.K. & Alivisatos, A.P. *Symmetry of annealed wurtzite CdSe nanocrystals - assignment to the C-3v point group*. J. Phys. Chem. **99**, 17417-17422 (1995).

43. Peng, X., Schlamp, M.C., Kadavanich, A.V. & Alivisatos, A.P. *Epitaxial growth of highly luminescent CdSe/CdS core/shell. nanocrystals with photostability and electronic accessibility*. J. Am. Chem. Soc. **119**, 7019-7029 (1997).

44. Lamer, V.K. & Dinegar, R.H. *The limiting degrees of super-saturation of the sparingly soluble sulfates*. J. Am. Chem. Soc. **73**, 380-385 (1951).

45. Murray, C.B., Kagan, C.R. & Bawendi, M.G. *Synthesis and characterization of monodisperse nanocrystals and close-packed nanocrystal assemblies*. Annu. Rev. Mat. Sci. **30**, 545-610 (2000).

46. De Smet, Y., Deriemaeker, L. & Finsy, R. *A simple computer simulation of ostwald ripening*. Langmuir **13**, 6884-6888 (1997).

47. Gratz, H. Ostwald ripening: *New relations between particle growth and particle size distribution.* Scripta Materialia, **37**, 9-16 (1997).

48. Sugimoto, T. *Preparation of monodispersed colloidal particles*. Adv. Colloid Interface Sci. **28**, 65-108 (1987).

49. Hines, M.A. & Guyot-Sionnest, P. *Synthesis and characterization of strongly luminescing ZnS-Capped CdSe nanocrystals*. J. Phys. Chem. **100**, 468-471 (1996).

50. Sukhanova, A., Devy, M., Venteo, L., Kaplan, H., Artemyev, M., Oleinikov, V., Klinov, D., Pluot, M., Cohen, J.H.M. & Nabiev, I. *Biocompatible fluorescent nanocrystals for immunolabeling of membrane proteins and cells*. Anal. Biochem. **324**, 60-67 (2004).

51. Reiss, P., Bleuse, J. & Pron, A. *Highly luminescent CdSe/ZnSe core/shell nanocrystals of low size dispersion*. Nano Lett. **2**, 781-784 (2002).

52. Alivisatos, A.P., Gu, W. & Larabell, C. *Quantum dots as cellular probes*. Annu. Rev. Biomed. Eng. **7**, 55-76 (2005).

53. Jamieson, T., Bakhshi, R., Petrova, D., Pocock, R., Imani, M. & Seifalian, A.M. *Biological applications of quantum dots*. Biomaterials **28**, 4717-4732 (2007).

54. Chan, W.C.W. & Nie, S.M. *Quantum dot bioconjugates for ultrasensitive nonisotopic detection*. Science **281**, 2016-2018 (1998).

55. Willard, D.M., Carillo, L.L., Jung, J. & Van Orden, A. *CdSe-ZnS quantum dots as resonance energy transfer donors in a model protein-protein binding assay*. Nano Lett. **1**, 469-474 (2001).

56. Mattoussi, H., Mauro, J.M., Goldman, E.R., Anderson, G.P., Sundar, V.C., Mikulec, F.V. & Bawendi, M.G. *Self-assembly of CdSe-ZnS quantum dot bioconjugates using an engineered recombinant protein*. J. Am. Chem. Soc. **122**, 12142-12150 (2000).

57. Pathak, S., Choi, S.K., Arnheim, N. & Thompson, M.E. *Hydroxylated quantum dots as luminescent probes for in situ hybridization*. J. Am. Chem. Soc. **123**, 4103-4104 (2001).

58. Goldman, E.R., Balighian, E.D., Mattoussi, H., Kuno, M.K., Mauro, J.M., Tran, P.T. & Anderson, G.P. *Avidin: a natural bridge for quantum dot-antibody conjugates*. J. Am. Chem. Soc. **124**, 6378-6382 (2002).

59. Mitchell, G.P., Mirkin, C.A. & Letsinger, R.L. *Programmed assembly of DNA functionalized quantum dots*. J. Am. Chem. Soc. **121**, 8122-8123 (1999).

60. Hong, R., Fischer, N.O., Verma, A., Goodman, C.M., Emrick, T. & Rotello, V.M. *Control of protein structure and function through surface recognition by tailored nanoparticle scaffolds*. J. Am. Chem. Soc. **126**, 739-743 (2004).

61. Sapsford, K.E., Berti, L. & Medintz, I.L. *Materials for fluorescence resonance energy transfer analysis: Beyond traditional donor-acceptor combinations*. Angew. Chem. Int. Ed. **45**, 4562-4588 (2006).

62. Clapp, A.R., Goldman, E.R. & Mattoussi, H. *Capping of CdSe-ZnS quantum dots with DHLA and subsequent conjugation with proteins*. Nat. Protoc. **1**, 1258-1266 (2006).

63. Jaiswal, J.K., Goldman, E.R., Mattoussi, H. & Simon, S.M. *Use of quantum dots for live cell imaging*. Nat Meth **1**, 73-78 (2004).

64. Voura, E.B., Jaiswal, J.K., Mattoussi, H. & Simon, S.M. *Tracking metastatic tumor cell extravasation with quantum dot nanocrystals and fluorescence emission-scanning microscopy*. Nat. Med. **10**, 993-998 (2004).

65. Liu, W., Choi, H.S., Zimmer, J.P., Tanaka, E., Frangioni, J.V. & Bawendi, M. *Compact cysteine-coated CdSe(ZnCdS) quantum dots for in vivo applications*. J. Am. Chem. Soc. **129**, 14530-14531 (2007).

66. Uyeda, H.T., Medintz, I.L., Jaiswal, J.K., Simon, S.M. & Mattoussi, H. *Synthesis of compact multidentate ligands to prepare stable hydrophilic quantum dot fluorophores*. J. Am. Chem. Soc. **127**, 3870-3878 (2005).

67. Susumu, K., Uyeda, H.T., Medintz, I.L., Pons, T., Delehanty, J.B. & Mattoussi, H. *Enhancing the stability and biological functionalities of quantum dots via compact multifunctional ligands*. J. Am. Chem. Soc. **129**, 13987-13996 (2007).

68. Pons, T., Uyeda, H.T., Medintz, I.L. & Mattoussi, H. *Hydrodynamic dimensions, electrophoretic mobility, and stability of hydrophilic quantum dots*. J. Phys. Chem. B **110**, 20308-20316 (2006).

69. Zimmer, J.P., Kim, S.W., Ohnishi, S., Tanaka, E., Frangioni, J.V. & Bawendi, M.G. *Size series of small indium arsenide-zinc selenide core-shell nanocrystals and their application to in vivo imaging*. J. Am. Chem. Soc. **128**, 2526-2527 (2006).

70. Liu, W., Howarth, M., Greytak, A.B., Zheng, Y., Nocera, D.G., Ting, A.Y. & Bawendi, M.G. *Compact biocompatible quantum dots functionalized for cellular imaging*. J. Am. Chem. Soc. **130**, 1274-1284 (2008).

71. Wu, X., Liu, H., Liu, J., Haley, K.N., Treadway, J.A., Larson, J.P., Ge, N., Peale, F. & Bruchez, M.P. *Immunofluorescent labeling of cancer marker Her2 and other cellular targets with semiconductor quantum dots*. Nat. Biotechnol. **21**, 41-46 (2003).

72. Chen, Y., Thakar, R. & Snee, P.T. *Imparting nanoparticle function with size-controlled amphiphilic polymers*. J. Am. Chem. Soc. **130**, 3744-3745 (2008).

73. Gao, X.H., Cui, Y.Y., Levenson, R.M., Chung, L.W.K. & Nie, S.M. *In vivo cancer targeting and imaging with semiconductor quantum dots*. Nat. Biotechnol. **22**, 969-976 (2004).

74. Dubertret, B., Skourides, P., Norris, D.J., Noireaux, V., Brivanlou, A.H. & Libchaber, A. *In vivo imaging of quantum dots encapsulated in phospholipid micelles*. Science **298**, 1759-1762 (2002).

75. Geissbuehler, I., Hovius, R., Martinez, K.L., Adrian, M., Thampi, K.R. & Vogel, H. *Lipid-coated nanocrystals as multifunctionalized luminescent scaffolds for supramolecular biological assemblies*. Angew. Chem. Int. Ed. **44**, 1388-1392 (2005).

76. Carion, O., Mahler, B., Pons, T. & Dubertret, B. *Synthesis, encapsulation, purification and coupling of single quantum dots in phospholipid micelles for their use in cellular and in vivo imaging*. Nat. Protoc. **2**, 2383-2390 (2007).

77. Bruchez, M., Moronne, M., Gin, P., Weiss, S. & Alivisatos, A.P. *Semiconductor nanocrystals as fluorescent biological labels*. Science **281**, 2013-2016 (1998).

78. Gerion, D., Pinaud, F., Williams, S.C., Parak, W.J., Zanchet, D., Weiss, S. & Alivisatos, A.P. *Synthesis and properties of biocompatible water-soluble silica-coated CdSe/ZnS semiconductor quantum dots*. J. Phys. Chem. B **105**, 8861-8871 (2001).

79. Guo, W., Li, J.J., Wang, Y.A. & Peng, X. *Conjugation chemistry and bioapplications of semiconductor box nanocrystals prepared via dendrimer bridging*. Chem. Mater. **15**, 3125-3133 (2003).

80. Osaki, F., Kanamori, T., Sando, S., Sera, T. & Aoyama, Y. *A quantum dot conjugated sugar ball and its cellular uptake on the size effects of endocytosis in the subviral region*. J. Am. Chem. Soc. **126**, 6520-6521 (2004).

81. Pellegrino, T., Manna, L., Kudera, S., Liedl, T., Koktysh, D., Rogach, A.L., Keller, S., Radler, J., Natile, G. & Parak, W.J. *Hydrophobic. nanocrystals coated with an amphiphilic polymer shell: a general. route to water soluble nanocrystals*. Nano Lett. **4**, 703-707 (2004).

82. Kim, S. & Bawendi, M.G. *Oligomeric ligands for luminescent and stable nanocrystal quantum dots*. J. Am. Chem. Soc. **125**, 14652-14653 (2003).

83. Slocik, J.M., Moore, J.T. & Wright, D.W. *Monoclonal antibody recognition of. histidine-rich peptide encapsulated nanoclusters*. Nano Lett. **2**, 169-173 (2002).

84. Pinaud, F., King, D., Moore, H.P. & Weiss, S. *Bioactivation and cell targeting of semiconductor CdSe/ZnS nanocrystals with phytochelatin-related peptides*. J. Am. Chem. Soc. **126**, 6115-6123 (2004).

85. Groc, L., Heine, M., Cognet, L., Brickley, K., Stephenson, F.A., Lounis, B. & Choquet, D. *Differential activity-dependent regulation of the lateral mobilities of AMPA and NMDA receptors*. Nat Neurosci **7**, 695-696 (2004).

86. Gao, X.H., Chan, W.C.W. & Nie, S.M. *Quantum-dot nanocrystals for ultrasensitive biological labeling and multicolor optical encoding*. J. Biomed. Optics **7**, 532-537 (2002).

87. Bawendi, M.G. *Nanocrystal quantum dots for biomedical and biological imaging.* MRS Fall meeting Presentation (2007).

88. Lakowicz, J.R. *Principles of Fluorescence Spectroscopy;*. Kluwer/Plenum: New York (1999).

89. Giepmans, B.N.G., Adams, S.R., Ellisman, M.H. & Tsien, R.Y. *The fluorescent toolbox for assessing protein location and function*. Science **312**, 217-224 (2006).

90. Clapp, A.R., Medintz, I.L., Mauro, J.M., Fisher, B.R., Bawendi, M.G. & Mattoussi, H. *Fluorescence resonance energy transfer between quantum dot donors and dye-labeled protein acceptors*. J. Am. Chem. Soc. **126**, 301-310 (2004).

91. Medintz, I.L., Clapp, A.R., Brunel, F.M., Tiefenbrunn, T., Tetsuo Uyeda, H., Chang, E.L., Deschamps, J.R., Dawson, P.E. & Mattoussi, H. *Proteolytic activity monitored by fluorescence resonance energy transfer through quantum-dot-peptide conjugates*. Nat Mater. **5**, 581-589 (2006).

92. van der Meer, B.W., Coker, G. & Chen, S.-Y.S. *Resonance energy transfer : theory and data*. New York : VCH, (1994).

93. Kukolka, F., Schoeps, O., Woggon, U. & Niemeyer, C.M. *DNA-directed assembly of supramolecular fluorescent protein energy transfer systems*. Bioconjugate Chem. **18**, 621-627 (2007).

94. Ramirez-Carrozzi, V.R. & Kerppola, T.K. *Dynamics of Fos-Jun-NFAT1 complexes*. Proc. Natl. Acad. Sci. U. S. A. **98**, 4893-4898 (2001).

95. Tong, A.K., Li, Z.M., Jones, G.S., Russo, J.J. & Ju, J.Y. *Combinatorial fluorescence energy transfer tags for multiplex biological assays*. Nat. Biotechnol. **19**, 756-759 (2001).

96. Liu, J.W. & Lu, Y. *FRET study of a trifluorophom-labeled DNAzyme*. J. Am. Chem. Soc. **124**, 15208-15216 (2002).

97. Haustein, E., Jahnz, M. & Schwille, P. *Triple FRET: A tool for studying long-range molecular interactions*. Chemphyschem **4**, 745-748 (2003).

98. Watrob, H.M., Pan, C.P. & Barkley, M.D. *Two-step FRET as a structural tool*. J. Am. Chem. Soc. **125**, 7336-7343 (2003).

99. Galperin, E., Verkhusha, V. & Sorkin, A. *Three-chromophore FRET microscopy to analyze multiprotein interactions in living cells*. Nat. Methods **1**, 209-217 (2004).

100. Heilemann, M., Tinnefeld, P., Mosteiro, G.S., Parajo, M.G., Van Hulst, N.F. & Sauer, M. *Multistep energy transfer in single molecular photonic wires*. J. Am. Chem. Soc. **126**, 6514-6515 (2004).

101. Klostermeier, D., Sears, P., Wong, C.H., Millar, D.P. & Williamson, J.R. *A three-fluorophore FRET assay for high-throughput screening of small-molecule inhibitors of ribosome assembly*. Nucleic Acids Res. **32**, 2707-2715 (2004).

102. Lee, N.K., Kapanidis, A.N., Koh, H.R., Korlann, Y., Ho, S.O., Kim, Y., Gassman, N., Kim, S.K. & Weiss, S. *Three-color alternating-laser excitation of single molecules: Monitoring multiple interactions and distances*. Biophys. J. **92**, 303-312 (2007).

103. Kawahara, S.-i., Uchimaru, T. & Murata, S. *Sequential multistep energy transfer: enhancement of efficiency of long-range fluorescence resonance energy transfer*. Chem. Commun., 563-564 (1999).

104. Medintz, I.L., Clapp, A.R., Mattoussi, H., Goldman, E.R., Fisher, B. & Mauro, J.M. *Self-assembled nanoscale biosensors based on quantum dot FRET donors*. Nat. Mater. **2**, 630-638 (2003).

105. Kim, J.H., Morikis, D. & Ozkan, M. *Adaptation of inorganic quantum dots for stable molecular beacons*. Sens. Actuators, B **102**, 315-319 (2004).

106. Medintz, I.L., Konnert, J.H., Clapp, A.R., Stanish, I., Twigg, M.E., Mattoussi, H., Mauro, J.M. & Deschamps, J.R. *A fluorescence resonance energy transfer-derived structure of a quantum dot-protein bioconjugate nanoassembly*. Proc. Natl. Acad. Sci. U. S. A. **101**, 9612-9617 (2004).

107. Medintz, I.L., Clapp, A.R., Melinger, J.S., Deschamps, J.R. & Mattoussi, H. *A reagentless biosensing assembly based on quantum dot-donor Forster resonance energy transfer*. Adv. Mater. **17**, 2450-2455 (2005).

108. Clapp, A.R., Medintz, I.L., Uyeda, H.T., Fisher, B.R., Goldman, E.R., Bawendi, M.G. & Mattoussi, H. *Quantum dot-based multiplexed fluorescence resonance energy transfer*. J. Am. Chem. Soc. **127**, 18212-18221 (2005).

109. Goldman, E.R., Medintz, I.L., Whitley, J.L., Hayhurst, A., Clapp, A.R., Uyeda, H.T., Deschamps, J.R., Lassman, M.E. & Mattoussi, H. *A hybrid quantum dot-antibody fragment fluorescence resonance energy transfer-based TNT sensor*. J. Am. Chem. Soc. **127**, 6744-6751 (2005).

110. Zhang, C.-Y., Yeh, H.-C., Kuroki, M.T. & Wang, T.-H. *Single-quantum-dot-based DNA nanosensor*. Nat Mater **4**, 826-831 (2005).

111. Oh, E., Hong, M.Y., Lee, D., Nam, S.H., Yoon, H.C. & Kim, H.S. *Inhibition assay of biomolecules based on fluorescence resonance energy transfer (FRET) between quantum dots and gold nanoparticles*. J. Am. Chem. Soc. **127**, 3270-3271 (2005).

112. Hohng, S. & Ha, T. *Single-molecule quantum-dot fluorescence resonance energy transfer*. Chemphyschem **6**, 956-960 (2005).

113. Shi, L., DePaoli, V., Rosenzweig, N. & Rosenzweig, Z. *Synthesis and application of quantum dots FRET-based protease sensors*. J. Am. Chem. Soc. **128**, 10378-10379 (2006).

114. Shi, L., Rosenzweig, N. & Rosenzweig, Z. *Luminescent quantum dots fluorescence resonance energy transfer-based probes for enzymatic activity and enzyme inhibitors*. Anal. Chem. **79**, 208-214 (2007).

115. Pons, T., Medintz, I.L., Sapsford, K.E., Higashiya, S., Grimes, A.F., English, D.S. & Mattoussi, H. *On the quenching of semiconductor quantum dot photoluminescence by proximal gold nanoparticles*. Nano Lett. **7**, 3157-3164 (2007).

116. Peng, H., Zhang, L., Kjallman, T.H.M., Soeller, C. & Travas-Sejdik, J. *DNA hybridization detection with blue luminescent quantum dots and dye-labeled single-stranded DNA*. J. Am. Chem. Soc. **129**, 3048-3049 (2007).

117. Medintz, I.L., Berti, L., Pons, T., Grimes, A.F., English, D.S., Alessandrini, A., Facci, P. & Mattoussi, H. *A reactive peptidic linker for self-assembling hybrid quantum dot-DNA bioconjugates*. Nano Lett. **7**, 1741-1748 (2007).

118. Akerman, M.E., Chan, W.C.W., Laakkonen, P., Bhatia, S.N. & Ruoslahti, E. *Nanocrystal targeting in vivo*. Proc. Natl. Acad. Sci. U. S. A. **99**, 12617-12621 (2002).

119. Lidke, D.S., Nagy, P., Heintzmann, R., Arndt-Jovin, D.J., Post, J.N., Grecco, H.E., Jares-Erijman, E.A. & Jovin, T.M. *Quantum dot ligands provide new insights into erbB/HER receptor-mediated signal transduction*. Nat. Biotechnol. **22**, 198-203 (2004).

120. Kim, S., Lim, Y.T., Soltesz, E.G., De Grand, A.M., Lee, J., Nakayama, A., Parker, J.A., Mihaljevic, T., Laurence, R.G., Dor, D.M., Cohn, L.H., Bawendi, M.G. & Frangioni, J.V. *Near-infrared fluorescent type II quantum dots for sentinel lymph node mapping*. Nat. Biotechnol. **22**, 93-97 (2004).

121. Soo Choi, H., Liu, W., Misra, P., Tanaka, E., Zimmer, J.P., Itty Ipe, B., Bawendi, M.G. & Frangioni, J.V. *Renal clearance of quantum dots*. Nat. Biotechnol. **25**, 1165-1170 (2007).

122. Larson, D.R., Zipfel, W.R., Williams, R.M., Clark, S.W., Bruchez, M.P., Wise, F.W. & Webb, W.W. *Water-soluble quantum dots for multiphoton fluorescence imaging in vivo*. Science **300**, 1434-1436 (2003).

123. Hainfeld, J.F., Liu, W., Halsey, C.M.R., Freimuth, P. & Powell, R.D. *Ni-NTA-gold clusters target His-tagged proteins*. J. Struc. Bio. **127**, 185-198 (1999).

124. Medintz, I.L., Trammell, S.A., Mattoussi, H. & Mauro, J.M. *Reversible modulation of quantum dot photoluminescence using a protein-bound photochromic fluorescence resonance energy transfer acceptor*. J. Am. Chem. Soc. **126**, 30-31 (2004).

125. Goldman, E.R., Anderson, G.P., Tran, P.T., Mattoussi, H., Charles, P.T. & Mauro, J.M. *Conjugation of luminescent quantum dots with antibodies. using an engineered adaptor protein to provide new reagents for fluoroimmunoassays*. Anal. Chem. **74**, 841-847 (2002).

126. Tian, Y., Newton, T., Kotov, N.A., Guldi, D.M. & Fendler, J.H. *Coupled composite CdS-CdSe and core-shell types of (CdS)CdSe. and (CdSe)CdS nanoparticles*. J. Phys. Chem. **100**, 8927-8939 (1996).

127. Danek, M., Jensen, K.F., Murray, C.B. & Bawendi, M.G. *Synthesis of luminescent thin-film CdSe/ZnSe quantum dot composites using CdSe quantum dots passivated with an overlayer of ZnSe*. Chem. Mater. **8**, 173-180 (1996).

128. Wilson, W.L., Szajowski, P.F. & Brus, L.E. *Quantum confinement in size-selected, surface-oxidized silicon nanocrystals*. Science **262**, 1242-1244 (1993).

129. Talapin, D.V., Rogach, A.L., Kornowski, A., Haase, M. & Weller, H. *Highly luminescent monodisperse CdSe and CdSe/ZnS nanocrystals synthesized. in a hexadecylamine-trioctylphosphine oxide-trioctylphospine mixture*. Nano Lett. **1**, 207-211 (2001).

130. Bawendi, M.G., Carroll, P.J., Wilson, W.L. & Brus, L.E. *Luminescence properties of CdSe quantum crystallites: resonance between interior and surface localized states*. J. Chem. Phys. **96**, 946-954 (1992).

131. Jonathan S. Steckel, J.P.Z.S.C.-S.N.E.S.V.B., cacute & Bawendi, M.G. *Blue luminescence from (CdS)ZnS core-shell nanocrystals*. Angew. Chem. Int. Ed. **43**, 2154-2158 (2004).

132. Johnsson, M., Hansson, P. & Edwards, K. *Spherical micelles and other self-assembled structures in dilute aqueous mixtures of poly(ethylene glycol) lipids*. J. Phys. Chem. B **105**, 8420-8430 (2001).

133. Lukyanov, A.N. & Torchilin, V.P. *Micelles from lipid derivatives of water-soluble polymers as delivery systems for poorly soluble drugs*. Adv. Drug Delivery Rev. **56**, 1273-1289 (2004).

134. Fan, H., Leve, E.W., Scullin, C., Gabaldon, J., Tallant, D., Bunge, S., Boyle, T., Wilson, M.C. & Brinker, C.J. *Surfactant-assisted synthesis of water-soluble and biocompatible semiconductor quantum dot micelles*. Nano Lett. **5**, 645-648 (2005).

135. Fan, H.Y., Yang, K., Boye, D.M., Sigmon, T., Malloy, K.J., Xu, H.F., Lopez, G.P. & Brinker, C.J. *Self-assembly of ordered, robust, three-dimensional gold nanocrystal/silica arrays*. Science **304**, 567-571 (2004).

136. Huang, X., Bronstein, L.M., Retrum, J., Dufort, C., Tsvetkova, I., Aniagyei, S., Stein, B., Stucky, G., McKenna, B., Remmes, N., Baxter, D., Kao, C.C. & Dragnea, B. *Self-assembled virus-like particles with magnetic cores*. Nano Lett. **7**, 2407-2416 (2007).

137. Dubertret, B. *Personal communication*. (2005).

138. Bentzen, E.L., Tomlinson, I.D., Mason, J., Gresch, P., Warnement, M.R., Wright, D., Sanders-Bush, E., Blakely, R. & Rosenthal, S.J. *Surface modification To reduce nonspecific binding ofquantum dots in live cell assays*. Bioconjugate Chem. **16**, 1488-1494 (2005).

139. Wuister, S.F., Houselt, A.v., Donega, C.d.M., Vanmaekelbergh, D. & Meijerink, A. *Temperature antiquenching of the luminescence from capped CdSe quantum dots*. Angew. Chem. Int. Ed. **43**, 3029-3033 (2004).

140. Moreels, I., Martins, J.C. & Hens, Z. *Ligand adsorption/desorption on sterically stabilized InP colloidal nanocrystals: observation and thermodynamic analysis*. Chemphyschem **7**, 1028-1031 (2006).

141. Hering, V.R., Gibson, G., Schumacher, R.I., Faljoni-Alario, A., Politi, M., xe & rio, J. *Energy transfer between CdSe/ZnS core/shell quantum dots and fluorescent proteins*. Bioconjugate Chem. **18**, 1705-1708 (2007).

142. Lu, H., Schoeps, O., Woggon, U. & Niemeyer, C.M. *Self-assembled donor comprising quantum dots and fluorescent proteins for long-range fluorescence resonance energy transfer*. J. Am. Chem. Soc. **130**, 4815-4827 (2008).

143. Wiedenmann, J., Schenk, A., Rocker, C., Girod, A., Spindler, K.D. & Nienhaus, G.U. *A far-red fluorescent protein with fast maturation and reduced oligomerization tendency from Entacmaea quadricolor (Anthozoa, Actinaria)*. Proc. Natl. Acad. Sci. U S A **99**, 11646-11651 (2002).

144. Wiedenmann, J., Vallone, B., Renzi, F., Nienhaus, K., Ivanchenko, S., Rocker, C. & Nienhaus, G.U. *Red fluorescent protein eqFP611 and its genetically engineered dimeric variants*. J. Biomed. Optics **10** (2005).

145. Yang, F., Moss, L.G. & Phillips, G.N. *The molecular structure of green fluorescent protein*. Nat. Biotechnol. **14**, 1246-1251 (1996).

146. Du, H., Fuh, R.C.A., Li, J.Z., Corkan, L.A. & Lindsey, J.S. *PhotochemCAD: A computer-aided design and research tool in photochemistry*. Photochem. Photobiol. **68**, 141-142 (1998).

147. Geissbuehler, I. *PhD dissertation*. Swiss Federal Institute of Technology Lausanne (EPFL), Switzerland (2005).

148. Kukolka, F., Muller, B.K., Paternoster, S., Arndt, A., Niemeyer, C.M., Brauchle, C. & Lamb, D.C. *A single-molecule Forster resonance energy transfer analysis of fluorescent DNA-protein conjugates for nanobiotechnology*. Small **2**, 1083-1089 (2006).

149. Kukolka, F. & Niemeyer, C.M. *Synthesis of fluorescent oligonucleotide-EYFP conjugate: Towards supramolecular construction of semisynthetic biomolecular antennae*. Org. Biomol. Chem. **2**, 2203-2206 (2004).

150. Schoeps, O. *Planned PhD Dissertation*. Technical University Dortmund, Germany (2008).

151. Kukolka, F. *PhD dissertation*. Technical University Dortmund, Germany (2007).

152. Swaminathan, R., Hoang, C.P. & Verkman, A.S. *Photobleaching recovery and anisotropy decay of green fluorescent protein GFP-S65T in solution and cells: Cytoplasmic viscosity probed by green fluorescent protein translational and rotational diffusion*. Biophys. J. **72**, 1900-1907 (1997).

153. Tsien, R.Y. *The green fluorescent protein*. Annu. Rev. Biochem. **67**, 509-544 (1998).

154. Clegg, R., Murchie, A., Zechel, A. & Lilley, D. *Observing the helical geometry of double-stranded DNA in solution by fluorescence resonance energy transfer*. Proc. Natl. Acad. Sci. U. S. A. **90**, 2994-2998 (1993).

155. Dahan, M., Levi, S., Luccardini, C., Rostaing, P., Riveau, B. & Triller, A. *Diffusion dynamics of glycine receptors revealed by single-quantum dot tracking*. Science **302**, 442-445 (2003).

156. Xiao, Y. & Barker, P.E. *Semiconductor nanocrystal probes for human metaphase chromosomes*. Nucleic Acids Res. **32** (2004).

157. Jaiswal, J.K., Mattoussi, H., Mauro, J.M. & Simon, S.M. *Long-term multiple color imaging of live cells using quantum dot bioconjugates*. Nat. Biotechnol. **21**, 47-51 (2003).

158. Derfus, A.M., Chan, W.C.W. & Bhatia, S.N. *Intracellular delivery of quantum dots for live cell labeling and organelle tracking*. Adv. Mater. **16**, 961-966 (2004).

159. Rozenzhak, S.M., Kadakia, M.P., Caserta, T.M., Westbrook, T.R., Stone, M.O. & Naik, R.R. *Cellular internalization and targeting of semiconductor quantum dots*. Chem. Commun., 2217-2219 (2005).

160. Silver, J. & Ou, W. *Photoactivation of quantum dot fluorescence following endocytosis*. Nano Lett. **5**, 1445-1449 (2005).

161. Chen, F.Q. & Gerion, D. *Fluorescent CdSe/ZnS nanocrystal-peptide conjugates for long-term, nontoxic imaging and nuclear targeting in living cells*. Nano Lett. **4**, 1827-1832 (2004).

162. Bucci, C., Thomsen, P., Nicoziani, P., McCarthy, J. & van Deurs, B. *Rab7: A key to lysosome biogenesis*. Mol. Biol. Cell **11**, 467-480 (2000).

163. Segev, N. *Ypt and Rab GTPases: insight into functions through novel interactions*. Curr. Opin. Biotechnol. **13**, 500-511 (2001).

164. Stein, M.P., Dong, J.B. & Wandinger-Ness, A. *Rab proteins and endocytic trafficking: potential targets for therapeutic intervention*. Adv. Drug Delivery Rev. **55**, 1421-1437 (2003).

165. Seabra, M.C. & Wasmeier, C. *Controlling the location and activation of Rab GTPases*. Curr. Opin. Biotechnol. **16**, 451-457 (2004).

166. Jager, S., Bucci, C., Tanida, I., Ueno, T., Kominami, E., Saftig, P. & Eskelinen, E.L. *Role for Rab7 in maturation of late autophagic vacuoles*. J. Cell Sci. **117**, 4837-4848 (2004).

167. Derfus, A.M., Chan, W.C.W. & Bhatia, S.N. *Probing the cytotoxicity of semiconductor quantum dots*. Nano Lett. **4**, 11-18 (2004).

168. Chen, Y. & Rosenzweig, Z. *Luminescent CdS quantum dots as selective ion probes*. Anal. Chem. **74**, 5132-5138 (2002).

169. Gopalakrishnan, G., Danelon, C., Izewska, P., Prummer, M., Bolinger, P.Y., Geissbuhler, I., Demurtas, D., Dubochet, J. & Vogel, H. *Multifunctional lipid/quantum dot hybrid nanocontainers for controlled targeting of live cells*. Angew. Chem. Int. Ed. **45**, 5478-5483 (2006).

170. Gussin, H.A., Tomlinson, I.D., Little, D.M., Warnement, M.R., Qian, H.H., Rosenthal, S.J. & Pepperberg, D.R. *Binding of muscimol-conjugated quantum dots to GABA(c) receptors*. J. Am. Chem. Soc. **128**, 15701-15713 (2006).

171. Gunsalus, I.C., Barton, L.S. & Gruber, W. *Biosynthesis and structure of lipoic acid derivatives*. J. Am. Chem. Soc. **78**, 1763-1766 (1956).

7 Appendix

7.1 Strategy and working tables for determining the extinction coefficient and size of CdSe from UV/Vis absorbance

The particle size and the extinction coefficient of a CdSe sample can be determined based on the UV/Vis absorption or emission spectra of the sample and Table 7.1-7.3.[30] Thus the particle concentration of the CdSe solution can be determined by using *Lambert-beer's law*: A=εcl

Where, A=absorbance (at the first absorption peak)

ε=extinction coefficient (Table 7.3) [$M^{-1}cm^{-1}$]

c=concentration of the CdSe NCs [M]

l=path length [cm]

For example, for the CdSe NCs sample in chloroform, with the first absorption peak λ=570 nm and absorbance A=0.1, the radius is *r*=22.10 Å (Table 7.1), the extinction coefficient is ε=316093 $M^{-1}cm^{-1}$ (Table 7.3) and the concentration of CdSe NCs can be calculated accordingly, c=A/εl=3.2×10^{-7} M.

Table 7.1 Absorption versus size for CdSe QDs, Size are in effective radii.

Absorption (nm)	Size (Å)	Absorption (nm)	Size (Å)	Absorption (nm)	Size (Å)	Absorption (nm)	Size (Å)
460.00	10.41	522.00	16.33	584.00	23.76	646.00	45.07
462.00	10.79	524.00	16.54	586.00	24.01	648.00	46.92
464.00	11.13	526.00	16.76	588.00	24.26	650.00	48.91
466.00	11.43	528.00	16.98	590.00	24.51		
468.00	11.71	530.00	17.21	592.00	24.78		
470.00	11.96	532.00	17.44	594.00	25.05		
472.00	12.19	534.00	17.68	596.00	25.33		
474.00	12.40	536.00	17.92	598.00	25.63		
476.00	12.60	538.00	18.16	600.00	25.94		
478.00	12.78	540.00	18.40	602.00	26.26		
480.00	12.94	542.00	18.65	604.00	26.61		
482.00	13.10	544.00	18.90	606.00	26.98		
484.00	13.25	546.00	19.15	608.00	27.37		
486.00	13.40	548.00	19.40	610.00	27.79		
488.00	13.54	550.00	19.65	612.00	28.25		
490.00	13.68	552.00	19.90	614.00	28.74		
492.00	13.82	554.00	20.15	616.00	29.26		
494.00	13.95	556.00	20.39	618.00	29.83		
496.00	14.09	558.00	20.64	620.00	30.45		
498.00	14.24	560.00	20.89	622.00	31.12		
500.00	14.38	562.00	21.13	624.00	31.84		
502.00	14.53	564.00	21.38	626.00	32.62		
504.00	14.69	566.00	21.62	628.00	33.47		
506.00	14.84	568.00	21.86	630.00	34.39		
508.00	15.01	570.00	22.10	632.00	35.39		
510.00	15.18	572.00	22.33	634.00	36.47		
512.00	15.36	574.00	22.57	636.00	37.64		
514.00	15.54	576.00	22.81	638.00	38.91		
516.00	15.73	578.00	23.04	640.00	40.27		
518.00	15.92	580.00	23.28	642.00	41.75		
520.00	16.12	582.00	23.52	644.00	43.35		

Table 7.2 Emission versus size for CdSe QDs. Size are in effective radii.

Absorption (nm)	Size (Å)	Absorption (nm)	Size (Å)	Absorption (nm)	Size (Å)	Absorption (nm)	Size (Å)
516	14.52	554	18.66	592	23.69	630	30.58
518	14.59	556	18.88	594	24.03	632	31.14
520	14.70	558	19.11	596	24.36	634	31.77
522	14.86	560	19.33	598	24.70	636	32.50
524	15.04	562	19.55	600	25.03	638	33.33
526	15.26	564	19.78	602	25.37	640	34.29
528	15.49	566	20.01	604	25.71	642	35.40
530	15.73	568	20.25	606	26.05	644	36.69
532	15.99	570	20.49	608	26.39	646	38.19
534	16.24	572	20.75	610	26.72	648	39.93
536	16.50	574	21.00	612	27.06	650	41.95
538	16.76	576	21.27	614	27.39	652	44.29
540	17.01	578	21.55	616	27.74	654	47.00
542	17.26	580	21.83	618	28.08	656	50.12
544	17.51	582	22.12	620	28.44	658	53.72
546	17.75	584	22.42	622	28.81	660	57.84
548	17.98	586	22.73	624	29.20		
550	18.21	588	23.05	626	29.62		
552	18.44	590	23.37	628	30.08		

Table 7.3 Extinction coefficient versus size for CdSe QDs. Sizes are in effective diameter (nm).

Dia (nm)	Ext Coeff ($M^{-1}cm^{-1}$)	Dia (nm)	Ext Coeff ($M^{-1}cm^{-1}$)	Dia (nm)	Ext Coeff ($M^{-1}cm^{-1}$)
1.5	5027.668800	3.0	210336.8635	4.5	321060.8133
1.6	22206.55000	3.1	220358.2435	4.6	325750.0169
1.7	38851.47660	3.2	229967.3572	4.7	330148.6424
1.8	54970.56120	3.3	239172.3172	4.8	334264.8026
1.9	70571.91620	3.4	247981.2359	4.9	338106.6098
2.0	85663.65420	3.5	256402.2260	5.0	341682.1767
2.1	100253.8878	3.6	264443.4000	5.1	344999.6158
2.2	114350.7296	3.7	272112.8705	5.2	348067.0397
2.3	127962.2921	3.8	279418.7500	5.3	350892.5610
2.4	141096.6878	3.9	286369.1510	5.4	353484.2921
2.5	153762.0293	4.0	292972.1862	5.5	355850.3456
2.6	165966.4292	4.1	299235.9681	5.6	357998.8342
2.7	177718.0000	4.2	305168.6091	5.7	359937.8703
2.8	189024.8543	4.3	310778.2220	5.8	361675.5665
2.9	199895.1046	4.4	316072.9192	5.9	363220.0353

7.2 Simulation of the photoluminescence evolution of the QD/EYFP/ Atto647 assembly

In order to model the temporal evolution of the excitations present in the FRET system, typically a set of rate equations like 7.1-3 representing the changes of the QD (EYFP) (Atto647) excitation as a function of the population and depopulation rates is solved.[142, 150]

$$\frac{d(QD)}{dt} = QD \cdot \left(-k_{QD,rad} - k_{QD,nonrad} - k_{QD\to EYFP} \cdot M_{EYFP} - k_{QD\to Atto647} \cdot M_{Atto647}\right) \quad 7.1$$

$$\frac{d(EYFP)}{dt} = EYFP \cdot \left(-k_{EYFP,rad} - k_{EYFP,nonrad} - k_{EYFP\to Atto647} \cdot \frac{M_{Atto647}}{M_{EYFP}} + QD \cdot k_{QD\to EYFP}\right) \quad 7.2$$

$$\frac{d(Atto647)}{dt} = Atto647 \cdot \left(-k_{Atto647,rad} - k_{Atto647,nonrad} + EYFP \cdot k_{EYFP\to Atto647} \cdot \frac{M_{EYFP}}{M_{Atto647}} + QD \cdot k_{QD\to Atto647}\right) \quad 7.3$$

The resulting functions for QD(t), EYFP (t) and Atto647(t) are then used as fit functions in a least square fit to the data. Since the parameter space spanned by such a set of functions, is rather large, an iterative approach was chosen, which simulates the population of QD, EYFP and Atto647 dye as entries in three 30000 cell long arrays, each cell resembling a time interval of 1 ps.

The initial condition on the arrival of the laser pulse is that all species are excited according to their absorbance at the excitation wavelength used. For all further times, the population of the QD is calculated from the previous time increment by taking into account the radiative and non-radiative decay, the transfer to the EYFP and the transfer to the Atto647 dye. It is important to note that here non-radiative means the intrinsic non-radiative depopulation, which is present even without transfer, due to the non unity quantum yield, as it is visible from the definition of the quantum yield as the ratio of the radiative recombination rate to the sum of radiative and non-radiative recombination rates. A back-filling transfer channel from the EYFP to the QD was initially taken into account in the programming, but found to be negligible in the overall process.

The excited state of the EYFP is populated, apart from the initial laser pulse, by the transfer from the QD donor, while depopulation is governed by radiative and non-radiative rates as well as the transfer transition to the Atto647 dye.

The Atto647 dye itself acts as an acceptor of transferred energy from both the QD and the protein, while depopulation is possible only by non-radiative decay of excitation or photon emission.

The intensities of the PL signals are then calculated by multiplying the population with the concentration and the radiative decay rate. Since the signals of the QD and the EYFP overlap, the sum of both contributions is calculated and compared to the measured decay in the corresponding wavelength interval.

Formulae:

Initialization:

QD[0]=pump*AQ, EYFP[0]=pump*AE, Atto[0]=pump*AA.

Calculation for t>0:

QD[i]=QD[i-1]*(1-GQR-GQNR -GQE*ME-GQA*MA)+EYFP[i-1]*GEQ*ME.

EYFP[i]= EYFP[i-1]*(1-GER-GENR-GEQ-GEA*MA/ME)+QD[i-1]*GQE

Atto[i]= Atto[i-1]*(1-GAR-GANR)+GEA*EYFP[i-1]*ME/MA+GQA*QD[i-1].

Calculation of PL intensities:

QD_PL[i]=QD[i]*GQR*MQ

EYFP_PL[i]=EYFP[i]*GER*ME

Atto_PL[i]=Atto[i]*GAR*MA

Variable definitions:

pump - intensity of the pump pulse in arbitrary units

AQ - absorbance of the QD at the laser wavelength

AE - absorbance of the EYFP at the laser wavelength

AA - absorbance of the Atto dye at the laser wavelength

QD[i] - the population of one QD unit at time index i

EYFP[i] - the population of one EYFP unit at time index i

Atto[i] - the population of one Atto dye unit at time index i

GQR - rate of radiative recombination of the QD

GQNR - rate of non-radiative recombination of the QD

GQE - Rate of QD to EYFP transfer

GQA - rate of QD to Atto dye transfer

GER - rate of radiative recombination of the EYFP

GENR - rate of non-radiative recombination of the EYFP

GEQ - rate of EYFP to QD (back)-transfer

GEA – Rate of EYFP to Atto647 transfer

GAR - rate of radiative recombination of the Atto dye

GANR - rate of non-radiative recombination of the Atto dye

MQ – concentration of the QD, (set to 1)

ME - concentration of the EYFP, relative to the QD concentration

MA - concentration of the atto dye relative to the QD concentration

Acknowledgements

Foremost, I would like to express my sincere gratitude to my supervisor Prof. Christof M. Niemeyer for giving me this interstesting project and leading me into the field of nanobiotechnology. I have to thank him for his thoughtful and patient guidance, motivation and encouragement. I also thank him for the pertinent remarks and useful suggestions he gave me during writing of this thesis.

I would like to thank Prof. Christian Becker for being in my examination committee.

I thank Prof. Ulrike Woggon and Oliver Schöps for their help with the 2D-PLE and time-resolved experiments, and also for their constructive suggestions and support on the QD-FRET project.

I wish to thank Prof. Christian Becker and Prof. Kirill Alexandrov for the helpful discussion on the cellular imaging project and also for providing me the experimental materials and facilities from their groups. I gratefully acknowledge IMRPS and Dr. Jutta Rötter for lots of considerate help.

I would like to say “thank-you” to Florian Kukolka, Binil Itty Ipe, Anne Adida and Christine Delon for their efficient help and discussion at the beginning of this work. I wish to thank Ljiljana very much for giving me helpful and sound advice during writing this thesis as well as a lot of help in daily life. I would also like to thank Matina, Petra, Andreas and Viola for their timely assistance and support during my PhD work. I wish to thank Marina, Bo, Joschi, Jessica, Max, Kersten, Mark and Vidmantas for their kind help in lab as well as outside. I hope to thank Kathrin for translating the summary of this thesis into German. I wish to thank all other BCMT members for their help and assistance. It is my great honor to share my research and life with them in the past three and a half years.

I would like to take this opportunity to thank all my friends and co-workers who gave me plenty of nice memories and pleasant experiences in Dortmund. These friendships are my most precious treasures. Specially, I thank Ying for all.

Finally I wish to thank my family for providing a loving environment for me, my parents, my brothers Ri-Chang, Le-Chang and Qiong-Yu for their unconditional love and infinite support.